TECHNISCHE UNIVERSITÄT WIEN

DIPLOMARBEIT

Light-light scattering in the presence of magnetic fields

zur Erlangung des akademischen Grades

Diplom-Ingenieur

im Rahmen des Studiums

Technische Physik

eingereicht von

Matthias Gerold Wödlinger BSc BSc
Matrikelnummer 01125717

ausgeführt am Institut für theoretische Physik
der Fakultät für Physik der Technischen Universität Wien

Betreuung
Beutreuer: Univ.-Prof. Dr. Anton Rebhan

Wien, _____ _____

(Matthias Wödlinger) (Anton Rebhan)

Abstract

Evidence for scattering of light by light has been found recently in heavy ion collisions by the ATLAS collaboration at the LHC. These collisions produce strong magnetic fields that can influence the probability of light-light scattering events. Motivated by these findings we investigate low energy light-light scattering in the presence of spatially homogeneous magnetic background fields in the Euler-Heisenberg theory.

We derive the scattering matrix element for four external photons in Euler-Heisenberg theory. With this we compute the full analytical differential cross section in the limit of weak fields and numerically for arbitrary field strengths. For spinor QED we find that scattering parallel to the magnetic field is suppressed. For scattering processes in which none of the involved photons is parallel to the magnetic field we find that the differential cross section for unpolarized photons averaged over final polarizations grows quadratically with the field strength were maximum growth can be found if the scattering plane is perpendicular to the field strength. For scalar QED we find no quadratic growth and the cross section drops quartic in the magnetic field. We conclude that the quadratic growth in the spinor case has its cause in the interaction of spin and magnetic field and show this claim in the worldline formulation of the one loop QED action. For charged vector particles we find a divergence of the cross section at $B/B_c = 1$ which we identify as a consequence of a phase transition to a superconducting vacuum state.

Contents

Chapter 1

Basics

1.1 Historical overview

Classically scattering of light by light is forbidden because of the linearity of the Maxwell equations. However if one also takes quantum effects into account one finds a non-zero probability for light-light scattering.

This was first discovered by two students of Heisenberg, Euler and Kockel in 1935 [1] where they computed the leading corrections to Maxwells electrodynamics in the low frequency limit (low photon energy compared to the electron mass). They found

$$\mathcal{L} = \frac{1}{2}(\mathbf{E}^2 - \mathbf{B}^2) + \frac{1}{90\pi}\frac{\hbar c}{e^2}\frac{1}{E_0^2}\left[(\mathbf{E}^2 - \mathbf{B}^2)^2 + 7(\mathbf{E}\cdot\mathbf{B})^2\right] \tag{1.1}$$

with $E_0 = m^2c^4/e^3$. They also computed the light-light scattering cross section for which they obtained

$$\sigma \propto \left(\frac{e^2}{\hbar c}\right)^4 \left(\frac{\hbar^4}{mc}\right)^4 \frac{1}{\lambda^6} \tag{1.2}$$

in the center of mass system.

Later in 1936 Euler and Heisenberg [2] extended the results and obtained the full nonlinear correction for spatially homogeneous background field. They obtained an integral representation of the Lagrangian

$$\begin{aligned}\mathcal{L} = \frac{1}{2}(\mathbf{E}^2 - \mathbf{B}^2) + \\ \frac{e^2}{2\pi\hbar c}\int_0^\infty \mathrm{d}\eta \frac{e^{-\eta}}{\eta^3}\left[i\eta^2(\mathbf{E}\cdot\mathbf{B})\frac{\cos\left(\frac{\eta}{|E_k|}\sqrt{\mathbf{E}^2 - \mathbf{B}^2 + 2i(\mathbf{E}\cdot\mathbf{B})}\right) + conj.}{\cos\left(\frac{\eta}{|E_k|}\sqrt{\mathbf{E}^2 - \mathbf{B}^2 + 2i(\mathbf{E}\cdot\mathbf{B})}\right) - conj.}\right. \\ \left. + \mathcal{E}_c^2 + \frac{\eta^2}{3}(\mathbf{E}^2 - \mathbf{B}^2)\right]\end{aligned} \tag{1.3}$$

with the critical field strength $\mathcal{E}_c = m_e^2 c^3/(e\hbar)$. The result of Euler and Kockel (1.1) can be regained from this by expanding the integral term in quartic order around the vacuum. This Lagrangian is nowadays called the *Euler-Heisenberg Lagrangian*. With it one can compute the cross section of light-light scattering for spatially homogeneous background fields (what we will do later) but one can also investigate other non-trivial effects that are not apparent in the classical theory and even non-perturbative effects like electron positron pair creation creation in strong electric background fields.

In a more modern language the work of Heisenberg and Euler can be understood as finding the low energy effective field theory of quantum electrodynamics (QED) in a constant background field by integrating out internal fermion loops. A more extensive discussion about the history of the Euler-Heisenberg Lagrangian can be found in [3].

Soon after the discovery by Euler and Heisenberg, Weisskopf found a simpler derivation that he also used to obtain the Euler-Heisenberg Lagrangian for scalar QED

$$\mathcal{L}^{(1)}_{\text{scalar}} = -\frac{1}{2\pi\hbar c}\int_0^\infty \frac{d\eta}{\eta^3} e^{\eta e \mathcal{E}_c}\left[\frac{2ie^2\eta^2(\mathbf{E}\cdot\mathbf{B})}{\cos\left(e\eta\sqrt{\mathbf{E}^2-\mathbf{B}^2+2i(\mathbf{E}\cdot\mathbf{B})}\right)-conj.} + 1 - \frac{e^2\eta^2}{6}(\mathbf{B}^2-\mathbf{E}^2)\right] \quad (1.4)$$

Further development by Fock [4], Stückelberg [5] and later by Feynman [6] led to the so-called world-line representation

$$\mathcal{L}^{(1)} = -\int_0^\infty \frac{d\eta}{s} e^{-m^2\eta}\int d^4x \int_{x(0)=x(\eta)=x} \mathcal{D}x\, e^{-S[x]} \quad (1.5)$$

where $S[x]$ is the classical action for a charged particle (which works for both, scalar and spinor QED) to propagate on a space-time trajectory $x^\mu(\tau)$ for total proper time s. The world line representation can be used to derive the Euler-Heisenberg Lagrangian in a simpler way [7] and to get a different perspective on the problem. A deeper discussion of the mentioned topics can be found in [8, 9].

The first experimental evidence for light-light scattering was found in 1953 by Robert R. Wilson [10] in the form of Delbrück scattering, the scattering of photons at the electromagnetic field of an atomic nucleus. Only recently in 2017 direct evidence for light-light scattering was found in heavy ion collisions at the ATLAS Collaboration at the LHC [11]. In these non-central heavy ion collisions very strong magnetic fields are created perpendicular to the scattering plane. The magnetic fields decay rapidly but reach fields strengths of up to $B/B_c \approx 10^5$ with the critical magnetic field $B_c = m_e^2/e$ [12, 13]. At photon energies of the order of 100 MeV, also charged virtual

scalar and vector particles (in particular pions, kaons and rho mesons) can contribute at leading order in α.

1.2 Basics and units

From now on we will us natural units with $\hbar = 1 = c$ and the elementary charge $e = \sqrt{4\pi\alpha}$ with α being the fine structure constant. There are several equivalent ways to write down the Euler-Heisenberg Lagrangian

$$\mathcal{L} = -\frac{1}{4}F_{\mu\nu}F^{\mu\nu} + \mathcal{L}^{(1)}. \tag{1.6}$$

Using the Lorentz invariants

$$\mathcal{F} = \frac{1}{4}F^{\mu\nu}F_{\mu\nu} = \frac{1}{2}(\mathbf{B}^2 - \mathbf{E}^2) \tag{1.7}$$

$$\mathcal{G} = \frac{1}{4}F^{\mu\nu}\tilde{F}_{\mu\nu} = \mathbf{E}\cdot\mathbf{B} \tag{1.8}$$

with the Hodge dual $\tilde{F}^{\mu\nu} = \frac{1}{2}\epsilon^{\mu\nu\alpha\beta}F_{\alpha\beta}$, we can write the integral term $\mathcal{L}^{(1)}$ of the Euler-Heisenberg Lagrangian as

$$\begin{aligned}\mathcal{L}^{(1)} = -\frac{1}{8\pi^2}\int_0^\infty \frac{ds}{s^3}e^{-ism^2}\Bigg[&(es)^2|\mathcal{G}|\cot\Big(es(\sqrt{\mathcal{F}^2+\mathcal{G}^2}+\mathcal{F})^{\frac{1}{2}}\Big)\\ &\times\coth\Big(es(\sqrt{\mathcal{F}^2+\mathcal{G}^2}-\mathcal{F})^{\frac{1}{2}}\Big) + \frac{2}{3}(es)^2\mathcal{F} - 1\Bigg].\end{aligned} \tag{1.9}$$

If one further defines

$$a = (\sqrt{\mathcal{F}^2+\mathcal{G}^2}+\mathcal{F})^{1/2} \tag{1.10}$$

and

$$b = (\sqrt{\mathcal{F}^2+\mathcal{G}^2}-\mathcal{F})^{1/2} \tag{1.11}$$

(one can show that $\pm a$ and $\pm ib$ are the eigenvalues of the matrix $F_{\mu\nu}$) then the Euler-Heisenberg for spinor QED can be rewritten as

$$\mathcal{L}^{(1)}_{\text{spinor}} = -\frac{1}{8\pi^2}\int_0^\infty \frac{ds}{s^3}e^{-m^2s}\left[(es)^2ab\cot(ebs)\coth(eas) - \frac{1}{3}(es)^2(a^2-b^2) - 1\right] \tag{1.12}$$

and for scalar QED

$$\mathcal{L}^{(1)}_{\text{scalar}} = -\frac{1}{16\pi^2}\int_0^\infty \frac{ds}{s^3}e^{-m^2s}\left[\frac{(es)^2ab}{\sinh(eb\eta)\sin(ea\eta)} + \frac{1}{6}(es)^2(a^2-b^2) - 1\right]. \tag{1.13}$$

These are the representations we will mostly work with.

Supersymmetric quantum electrodynamics (SUSY QED), a theory that contains two complex scalar fields and one Dirac fermion, can then be described with

$$\mathcal{L}^{(1)}_{\text{SUSY}} = 2\mathcal{L}^{(1)}_{\text{scalar}} + \mathcal{L}^{(1)}_{\text{spinor}}. \tag{1.14}$$

For charged vector particles with a gyromagnetic ratio $g = 2$ an effective one-loop Lagrangian was first obtained by Vanyashin and Terent'ev in [14] where they found that the Lagrangian has the integral representation

$$\begin{aligned}\mathcal{L}^{(1)} = \frac{e^2}{4\pi^2}\int_0^\infty \frac{ds}{s}\left[e^{-im^2 s}\, a\left(b\,\frac{\sin eas}{\sinh ebs} - a\right) - e^{-m^2 s}\, b\left(a\,\frac{\sin ebs}{\sinh eas} - b\right)\right] \\ + \frac{3}{16\pi^2}\int_0^\infty \frac{ds}{s} e^{-m^2 t}\left(\frac{e^2 ab}{\sin ebs \sinh eas} - \frac{1}{s^2} - \frac{e^2}{6}(b^2 - a^2)\right).\end{aligned} \tag{1.15}$$

We will refer to this as vector QED.

Chapter 2

The scattering matrix element

2.1 Euler-Heisenberg 4-Vertex

In QED the lowest order contribution to light-light scattering comes from diagram (2.1) that couples four external photons through an internal fermion loop.

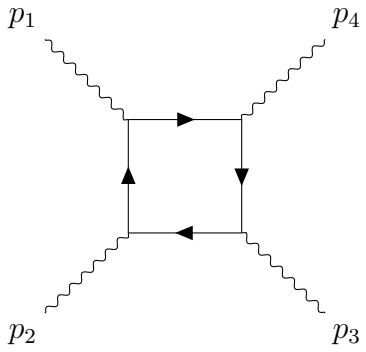

(2.1)

The effective theory is obtained by integrating out these internal loops. In this effective theory we can then describe the same process with a tree level diagram where quantum correction of the internal fermion loop is incorporated in the new vertex. Figure (2.2) shows this in Euler-Heisenberg theory.

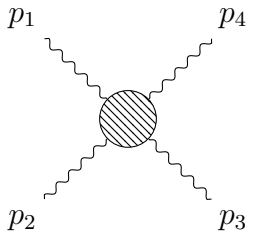

(2.2)

Evaluation of (2.2) then gives us the matrix element for light-light scattering. Therefore, if we want to compute the light-light scattering matrix all that is left to do is to compute the tree-level four-Vertex in Euler-Heisenberg theory.

To do that we need to evaluate the path integral

$$Z(J) \cong \langle 0|0\rangle_J \cong \int \mathcal{D}A \, \exp\left(i \int d^4x [-\frac{1}{4} F^{\mu\nu} F_{\mu\nu} + J^\mu A_\mu + \mathcal{L}^{(1)}]\right).$$

Using functional derivatives $\frac{\delta}{\delta J(x)}$ one can rewrite this as

$$Z(J) = e^{i \int d^4x \mathcal{L}_1 \left(\frac{1}{i} \frac{\delta}{\delta J_\mu(x)} \right)} \int \mathcal{D}A \, e^{i \int d^4x [-\frac{1}{4} F^{\mu\nu} F_{\mu\nu} + J^\mu A_\mu]}.$$

The second term which describes the result in the free field theory can be computed explicitly

$$\begin{aligned} Z_0 &:= \int \mathcal{D}A \, e^{i \int d^4x [-\frac{1}{4} F^{\mu\nu} F_{\mu\nu} + J^\mu A_\mu]} \\ &\propto \exp\left[\frac{i}{2} \int \frac{d^4k}{(2\pi)^4} \tilde{J}_\mu(k) \frac{P^{\mu\nu}}{k^2 - i\epsilon} \tilde{J}_\nu(-k) \right] \\ &\propto \exp\left[\frac{i}{2} \int d^4x d^4y \, J_\mu(x) \Delta^{\mu\nu}(x-y) J_\nu(y) \right] \end{aligned}$$

where $\Delta^{\mu\nu}$ denotes the photon propagator and we wrote proportional to account for normalization factors. For the full derivation see for example [15]. With this we can write

$$Z(J) \propto \exp\left[i \int d^4x \, \mathcal{L}_1 \left(\frac{1}{i} \frac{\delta}{\delta J_\mu(x)} \right) \right] \times \exp\left[\frac{i}{2} \int d^4x \, d^4y \, J_\mu(x) \Delta^{\mu\nu}(x-y) J_\nu(y) \right]. \tag{2.3}$$

We are interested in the result for a constant homogeneous background field A_μ^{BG} therefore we can perform a Taylor expansion of $\mathcal{L}^{(1)}$ around $A_\mu = A_\mu^{\mathrm{BG}}$:

$$\begin{aligned} \mathcal{L}^{(1)} \left(\frac{1}{i} \frac{\delta}{\delta J_\mu(x)} \right) = \mathcal{L}^{(1)}(A_\mu^{\mathrm{BG}}) + \sum_{n=0}^{\infty} \frac{1}{n!} \frac{\partial^n}{\partial F_{\mu_1\nu_1} \cdots \partial F_{\mu_n\nu_n}} \mathcal{L}^{(1)}(A_\mu) \Big|_{A_\mu = A_\mu^{\mathrm{BG}}} \\ \times \left(\frac{1}{i} \right)^n \prod_{k=1}^{n} \left(\partial^{\mu_k} \frac{\delta}{\delta J_{\nu_k}(x)} - \partial^{\nu_k} \frac{\delta}{\delta J_{\mu_k}(x)} \right) \end{aligned}$$

where $\partial^{\mu_k} \frac{\delta}{\delta J_\mu(x)}$ can be understood as $\partial^{\mu_k} \circ \frac{\delta}{\delta J_\mu(x)}$. If we plug this in (2.3) and perform the dual Taylor expansion of the exponentials we get the sum of all Feynman diagrams. For the effective tree-level diagram with four external photon lines (Diagram (2.2)) the lowest order contribution is given by the term with four derivatives. Ignoring the

higher order terms we obtain for the time ordered product of four operators at tree level

$$\begin{aligned}\langle 0|\,\mathrm{T}A_{\rho_1}(x_1)A_{\rho_2}(x_2)A_{\rho_3}(x_3)A_{\rho_4}(x_4)\,|0\rangle = \\ &= \left[\prod_{n=1}^{4}\frac{1}{i}\frac{\delta}{\delta J_{\rho_n}(x_n)}\right] iW(J)\Big|_{J=0} \\ &= ii^4\int d^4y\prod_{k=1}^{4}\left(\partial_y^{\mu_k}\Delta^{\nu_k}{}_{\rho_k}(x_k-y)-\partial_y^{\nu_k}\Delta^{\mu_k}{}_{\rho_k}(x_k-y)\right) \\ &\qquad\times\frac{\partial^n}{\partial F_{\mu_1\nu_1}\cdots\partial F_{\mu_n\nu_n}} i\mathcal{L}^{(1)}(A_\mu(y))\Big|_{A_\mu=A_\mu^{\mathrm{BG}}},\end{aligned}$$

where $W(J)$ is given by the sum of all fully connected diagrams with no tadpoles and at least two sources. Using the LSZ formula for photons we find that the scattering matrix element $\langle f|i\rangle = \langle\gamma(3)+\gamma(4)|\gamma(1)+\gamma(2)\rangle$ is given by

$$\langle f|i\rangle = i^4\int\prod_{j=1}^{4}d^4x_j\,\epsilon_j^{\rho_j}e^{-ik_jx_j}(-\partial_j^2)\,\langle 0|\,\mathrm{T}A_{\rho_1}(x_1)A_{\rho_2}(x_2)A_{\rho_3}(x_3)A_{\rho_4}(x_4)\,|0\rangle\,.$$

Inserting our expression for the time ordered 4 product gives

$$\begin{aligned}\langle f|i\rangle = ii^4i^4\int d^4y\prod_{j=1}^{4}d^4x_j\,\epsilon_j^{\rho_j}e^{-ik_jx_j}\left(\partial_y^{\mu_j}\delta^{\nu_j}{}_{\rho_j}(x_j-y)-\partial_y^{\nu_j}\delta^{\mu_j}{}_{\rho_j}(x_j-y)\right) \\ \times\frac{\partial^n}{\partial F_{\mu_1\nu_1}\cdots\partial F_{\mu_n\nu_n}} i\mathcal{L}^{(1)}(A_\mu(y))\Big|_{A_\mu=A_\mu^{\mathrm{BG}}}.\end{aligned}$$

The integration over d^4x is trivial because of the Dirac delta and we obtain

$$\begin{aligned}\langle f|i\rangle = i\int d^4y\,e^{-i(k_1+k_2+k_3+k_4)y}\prod_{j=1}^{4}\left(\partial_y^{\mu_k}\epsilon_j^{\nu_j}-\partial_y^{\nu_k}\epsilon_j^{\mu_j}\right) \\ \times\frac{\partial^n}{\partial F_{\mu_1\nu_1}\cdots\partial F_{\mu_n\nu_n}} i\mathcal{L}^{(1)}(A_\mu(y))\Big|_{A_\mu=A_\mu^{\mathrm{BG}}}.\end{aligned}$$

The remaining integral performs a Fourier transformation after which we obtain

$$\langle f|i\rangle = i\prod_{j=1}^{4}\left(k_j^{\mu_k}\epsilon_j^{\nu_j}-k_j^{\nu_k}\epsilon_j^{\mu_j}\right)\frac{\partial^n}{\partial F_{\mu_1\nu_1}\cdots\partial F_{\mu_n\nu_n}} i\mathcal{L}^{(1)}(A_\mu)\Big|_{A_\mu=A_\mu^{\mathrm{BG}}} \tag{2.4}$$

with $\sum k_j = 0$.

2.2 Geometry and Kinematics

With the general form of the matrix element at hand we can start with the evaluation. We are investigating the process $\gamma(k_1) + \gamma(k_2) \to \gamma(k_3) + \gamma(k_4)$ in the center-of-mass system. The scattering plane is the linear span of

$$\hat{\mathbf{k}} = (1, 0, 0) \tag{2.5}$$

$$\hat{\mathbf{k}}' = (\cos\eta, \sin\eta, 0) \tag{2.6}$$

with the scattering angle η. and the momentum vectors of our photons in this system are given by

$$k_1 = (\omega, \omega\hat{\mathbf{k}}), \tag{2.7}$$

$$k_2 = (\omega, -\omega\hat{\mathbf{k}}), \tag{2.8}$$

$$k_3 = (\omega, \omega\hat{\mathbf{k}}'), \tag{2.9}$$

$$k_4 = (\omega, -\omega\hat{\mathbf{k}}'), \tag{2.10}$$

where ω denotes the photon energy. For linear polarizations we denote the unit polarization vectors in and out of the scattering plane with $\hat{\boldsymbol{\epsilon}}_i^n$ and $\hat{\boldsymbol{\epsilon}}_o^n$ respectively. They are chosen so that they form a right-handed orthogonal basis together with the photon momenta:

$$\hat{\boldsymbol{\epsilon}}_i^1 = (0, 1, 0), \qquad \hat{\boldsymbol{\epsilon}}_o^1 = (0, 0, 1), \tag{2.11}$$

$$\hat{\boldsymbol{\epsilon}}_i^2 = (0, 1, 0), \qquad \hat{\boldsymbol{\epsilon}}_o^2 = (0, 0, -1), \tag{2.12}$$

$$\hat{\boldsymbol{\epsilon}}_i^3 = (-\sin\eta, \cos\eta, 0), \qquad \hat{\boldsymbol{\epsilon}}_o^3 = (0, 0, 1), \tag{2.13}$$

$$\hat{\boldsymbol{\epsilon}}_i^4 = (-\sin\eta, \cos\eta, 0), \qquad \hat{\boldsymbol{\epsilon}}_o^4 = (0, 0, -1). \tag{2.14}$$

With the preparations being done we can finally work out the

2.3 Light-light scattering matrix element

As discussed in section 2.1 the matrix element for low energy light-light scattering is given by the derivative of the Euler-Heisenberg Lagrangian. It turns that in order to obtain these derivatives it is useful to introduce the three-vectors

$$\mathbf{F}^{\pm} = \mathbf{B} \pm i\mathbf{E}$$

With these the Lorentz invariant $\mathcal{F}$ and $\mathcal{G}$ can be expressed as

$$\mathcal{F} = \frac{1}{2}(\mathbf{B}^2 - \mathbf{E}^2) = \frac{1}{4}(\mathbf{F}^{+2} + \mathbf{F}^{-2}),$$

$$\mathcal{G} = -\mathbf{E}\cdot\mathbf{B} = \frac{i}{4}(\mathbf{F}^{+2} - \mathbf{F}^{-2}).$$

We can use this to express the partial derivatives with respect to $\mathbf{F}^{\pm}$ in terms of derivatives with respect to our Lorentz invariants

$$\frac{\partial}{\partial F_r^{\pm}} = \frac{1}{2}F_r^{\pm}\left(\frac{\partial}{\partial \mathcal{F}} \mp i\frac{\partial}{\partial \mathcal{G}}\right) + \text{rest}. \tag{2.15}$$

Where *rest* denotes all the other derivatives. We can ignore them when we apply the derivative to the Euler-Heisenberg Lagrangian because it only depends on $\mathcal{F}$ and $\mathcal{G}$. Our incoming photon field tensors can also be expressed as three vectors

$$\begin{aligned}
\mathbf{f}_{i/o}^{1\pm} &= \omega(\hat{k} \times \hat{\epsilon}_{i/o}^{1} \pm i\epsilon_{i/o}^{1}),\\
\mathbf{f}_{i/o}^{2\pm} &= \omega(-\hat{k} \times \hat{\epsilon}_{i/o}^{2} \pm i\epsilon_{i/o}^{2}),\\
\mathbf{f}_{i/o}^{3\pm} &= \omega(\hat{k}' \times \hat{\epsilon}_{i/o}^{3} \pm i\epsilon_{i/o}^{3}),\\
\mathbf{f}_{i/o}^{4\pm} &= \omega(-\hat{k}' \times \hat{\epsilon}_{i/o}^{4} \pm i\epsilon_{i/o}^{4}).
\end{aligned}$$

With our new vector notation for the fields we can rewrite the matrix element (2.4) in terms of the vectors given above

$$\begin{aligned}
\mathcal{M} = &\left(f_r^{1+}\cdot\frac{\partial}{\partial F_r^{+}} + f_r^{1-}\cdot\frac{\partial}{\partial F_r^{-}}\right)\left(f_r^{2+}\cdot\frac{\partial}{\partial F_r^{+}} + f_r^{2-}\cdot\frac{\partial}{\partial F_r^{-}}\right)\\
&\times\left(f_r^{3+}\cdot\frac{\partial}{\partial F_r^{+}} + f_r^{3-}\cdot\frac{\partial}{\partial F_r^{-}}\right)\left(f_r^{4+}\cdot\frac{\partial}{\partial F_r^{+}} + f_r^{4-}\cdot\frac{\partial}{\partial F_r^{-}}\right)\times\mathcal{L}^{(1)},
\end{aligned} \tag{2.16}$$

where r, s, t and u are three dimensional indices that need to be summed over. Explicitly performing the multiplication gives the following expression

$$\begin{aligned}
\mathcal{M} = &f_r^{1+}f_r^{2+}f_r^{3+}f_r^{4+}\frac{\partial^4\mathcal{L}^{(1)}}{\partial F_r^{+}\partial F_s^{+}\partial F_t^{+}\partial F_u^{+}}\\
&+ (f_r^{1+}f_r^{2+}f_r^{3+}f_r^{4-} + f_r^{1+}f_r^{2+}f_r^{4+}f_r^{3-} + f_r^{1+}f_r^{3+}f_r^{4+}f_r^{2-}\\
&\qquad + f_r^{2+}f_r^{3+}f_r^{4+}f_r^{1-})\frac{\partial^4\mathcal{L}^{(1)}}{\partial F_r^{+}\partial F_s^{+}\partial F_t^{+}\partial F_u^{-}}\\
&+ (f_r^{1+}f_r^{2+}f_r^{3-}f_r^{4-} + f_r^{1+}f_r^{3+}f_r^{2-}f_r^{4-} + f_r^{1+}f_r^{4+}f_r^{2-}f_r^{3-} + f_r^{2+}f_r^{3+}f_r^{1-}f_r^{4-}\\
&\qquad + f_r^{3+}f_r^{4+}f_r^{1-}f_r^{2-} + f_r^{2+}f_r^{4+}f_r^{1-}f_r^{3-})\frac{\partial^4\mathcal{L}^{(1)}}{\partial F_r^{+}\partial F_s^{+}\partial F_t^{-}\partial F_u^{-}}\\
&+ (f_r^{1-}f_r^{2-}f_r^{3-}f_r^{4+} + f_r^{1-}f_r^{2-}f_r^{4-}f_r^{3+} + f_r^{1-}f_r^{3-}f_r^{4-}f_r^{2+}\\
&\qquad + f_r^{2-}f_r^{3-}f_r^{4-}f_r^{1+})\frac{\partial^4\mathcal{L}^{(1)}}{\partial F_r^{-}\partial F_s^{-}\partial F_t^{-}\partial F_u^{+}}\\
&+ f_r^{1-}f_r^{2-}f_r^{3-}f_r^{4-}\frac{\partial^4\mathcal{L}^{(1)}}{\partial F_r^{-}\partial F_s^{-}\partial F_t^{-}\partial F_u^{-}}
\end{aligned}$$

This rather lengthy expression can be expanded by expressing the derivatives with respect to $\boldsymbol{F}^{\pm}$ through derivatives with respect to $\mathcal{F}$ and $\mathcal{G}$ using (2.15). This makes taking the derivatives easier and the problem numerically nicer to handle. We obtain

$$\begin{aligned}
\frac{\partial^4\mathcal{L}^{(1)}}{\partial F_r^+\partial F_s^+\partial F_t^+\partial F_u^+} =&\frac{1}{4}(\delta_{rs}\delta_{tu}+\delta_{st}\delta_{ru}+\delta_{su}\delta_{rt})\left(\frac{\partial^2\mathcal{L}^{(1)}}{\partial^2\mathcal{F}}-\frac{\partial^2\mathcal{L}^{(1)}}{\partial^2\mathcal{G}}\right)\\
&+\frac{1}{8}(\delta_{tu}F_s^+F_r^+ + \delta_{st}F_r^+F_u^+ + \delta_{su}F_r^+F_t^+ + \delta_{rs}F_t^+F_u^+\\
&\qquad + \delta_{rt}F_s^+F_u^+ + \delta_{ru}F_s^+F_t^+)\times\left(\frac{\partial^3\mathcal{L}^{(1)}}{\partial^3\mathcal{F}}-3\frac{\partial^3\mathcal{L}^{(1)}}{\partial\mathcal{F}\partial^2\mathcal{G}}\right)\\
&+\frac{1}{16}F_r^+F_s^+F_t^+F_u^+\left(\frac{\partial^4\mathcal{L}^{(1)}}{\partial^4\mathcal{F}}-6\frac{\partial^4\mathcal{L}^{(1)}}{\partial^2\mathcal{F}\partial^2\mathcal{G}}\right)
\end{aligned}$$

$$\begin{aligned}
\frac{\partial^4\mathcal{L}^{(1)}}{\partial F_r^+\partial F_s^+\partial F_t^+\partial F_u^-} =&\frac{1}{8}(\delta_{st}F_r^+F_u^- + \delta_{rs}F_t^+F_u^- + \delta_{rt}F_s^+F_u^-)\left(\frac{\partial^3\mathcal{L}^{(1)}}{\partial^3\mathcal{F}}+\frac{\partial^3\mathcal{L}^{(1)}}{\partial\mathcal{F}\partial^2\mathcal{G}}\right)\\
&+\frac{1}{16}F_r^+F_s^+F_t^+F_u^-\left(\frac{\partial^4\mathcal{L}^{(1)}}{\partial^4\mathcal{F}}-\frac{\partial^4\mathcal{L}^{(1)}}{\partial^4\mathcal{G}}\right)
\end{aligned}$$

$$\begin{aligned}
\frac{\partial^4\mathcal{L}^{(1)}}{\partial F_r^+\partial F_s^+\partial F_t^-\partial F_u^-} =&\frac{1}{4}\delta_{rs}\delta_{tu}\left(\frac{\partial^2\mathcal{L}^{(1)}}{\partial^2\mathcal{F}}+\frac{\partial^2\mathcal{L}^{(1)}}{\partial^2\mathcal{G}}\right)\\
&+\frac{1}{8}(\delta_{rs}F_t^-F_u^- - \delta_{tu}F_r^+F_s^+)\left(\frac{\partial^3\mathcal{L}^{(1)}}{\partial^3\mathcal{F}}+\frac{\partial^3\mathcal{L}^{(1)}}{\partial\mathcal{F}\partial^2\mathcal{G}}\right)\\
&+\frac{1}{16}F_r^+F_s^+F_t^-F_u^-\left(\frac{\partial^4\mathcal{L}^{(1)}}{\partial^4\mathcal{F}}+2\frac{\partial^2\mathcal{L}^{(1)}}{\partial^2\mathcal{F}\partial^2\mathcal{G}}+\frac{\partial^4\mathcal{L}^{(1)}}{\partial^4\mathcal{G}}\right)
\end{aligned}$$

$$\begin{aligned}
\frac{\partial^4\mathcal{L}^{(1)}}{\partial F_r^-\partial F_s^-\partial F_t^-\partial F_u^+} =&\frac{1}{8}(\delta_{st}F_r^-F_u^+ + \delta_{rs}F_t^-F_u^+ + \delta_{rt}F_s^-F_u^+)\left(\frac{\partial^3\mathcal{L}^{(1)}}{\partial^3\mathcal{F}}+\frac{\partial^3\mathcal{L}^{(1)}}{\partial\mathcal{F}\partial^2\mathcal{G}}\right)\\
&+\frac{1}{16}F_r^-F_s^-F_t^-F_u^+\left(\frac{\partial^4\mathcal{L}^{(1)}}{\partial^4\mathcal{F}}-\frac{\partial^4\mathcal{L}^{(1)}}{\partial^4\mathcal{G}}\right)
\end{aligned}$$

$$\begin{aligned}
\frac{\partial^4\mathcal{L}^{(1)}}{\partial F_r^-\partial F_s^-\partial F_t^-\partial F_u^-} =&\frac{1}{4}(\delta_{rs}\delta_{tu}-\delta_{st}\delta_{ru}-\delta_{su}\delta_{rt})\left(\frac{\partial^2\mathcal{L}^{(1)}}{\partial^2\mathcal{F}}-\frac{\partial^2\mathcal{L}^{(1)}}{\partial^2\mathcal{G}}\right)\\
&+\frac{1}{8}(\delta_{tu}F_s^-F_r^- - \delta_{st}F_r^-F_u^- - \delta_{su}F_r^-F_t^- - \delta_{rs}F_t^-F_u^-\\
&\qquad - \delta_{rt}F_s^-F_u^- - \delta_{ru}F_s^-F_t^-)\times\left(\frac{\partial^3\mathcal{L}^{(1)}}{\partial^3\mathcal{F}}-3\frac{\partial^3\mathcal{L}^{(1)}}{\partial\mathcal{F}\partial^2\mathcal{G}}\right)\\
&+\frac{1}{16}F_r^-F_s^-F_t^-F_u^-\left(\frac{\partial^4\mathcal{L}^{(1)}}{\partial^4\mathcal{F}}-6\frac{\partial^4\mathcal{L}^{(1)}}{\partial^2\mathcal{F}\partial^2\mathcal{G}}\right)
\end{aligned}\tag{2.17}$$

Above we neglected terms with an uneven number of $\mathcal{G}$ derivatives because they vanish for $\boldsymbol{E} = \mathbf{0}$.

These expressions were computed in Mathematica. In the general case where we had to integrate numerically we performed the differentiation on the integrand and integrated afterwards. The swap of differentiation and integration is justified if the differentiated integrand is integrable. This is the case because the numerical integration is performed on a compact interval and the fact that the integrand is a C^∞ function in a and b. This implies that the differentiated function is continuous and therefore integrable on every compact interval.

Chapter 3

Results for spinor QED

3.1 Method

The matrix element described in (2.16 - 2.17) was evaluated using Mathematica 10.1. The proper time integration was only evaluated analytically in the weak field limit. In the general case we evaluated the integrals numerically using the built-in functions for numerical integration.

We evaluated the matrix element for the case of a spatially homogeneous magnetic background field and vanishing electric background i.e. $\partial_i \mathbf{B} = \mathbf{0}$ and $\mathbf{E} = \mathbf{0}$. To do this we used the Lagrangian given in (1.12) Taylor expanded in a around $a = 0$ to fourth order. This enabled us to take the limit $a \to 0$ nicely which is the limit of vanishing electric fields.

For the low field limit we also performed a Taylor expansion in b around $b = 0$. Furthermore we define the critical field strength

$$B_c = \frac{m_e^2}{e} \tag{3.1}$$

and the ratio of the magnetic field and the critical field strength is denoted by

$$\xi = \frac{B}{B_c}. \tag{3.2}$$

3.2 No background fields

In this section we want to present the well known scattering cross section for light-light scattering in vacuum. This has been obtained the first time by Euler and Kockel in 1935 [1]. The differential cross section for the scattering process $\gamma(\epsilon_1) + \gamma(\epsilon_2) \to \gamma(\epsilon_3) + \gamma(\epsilon_4)$ in the center-of-mass frame is given by

$$\frac{d\sigma}{d\Omega} = \frac{1}{(16\pi)^2 \omega^2} |\mathcal{M}_{\epsilon_1 \epsilon_2 \epsilon_3 \epsilon_4}|^2.$$

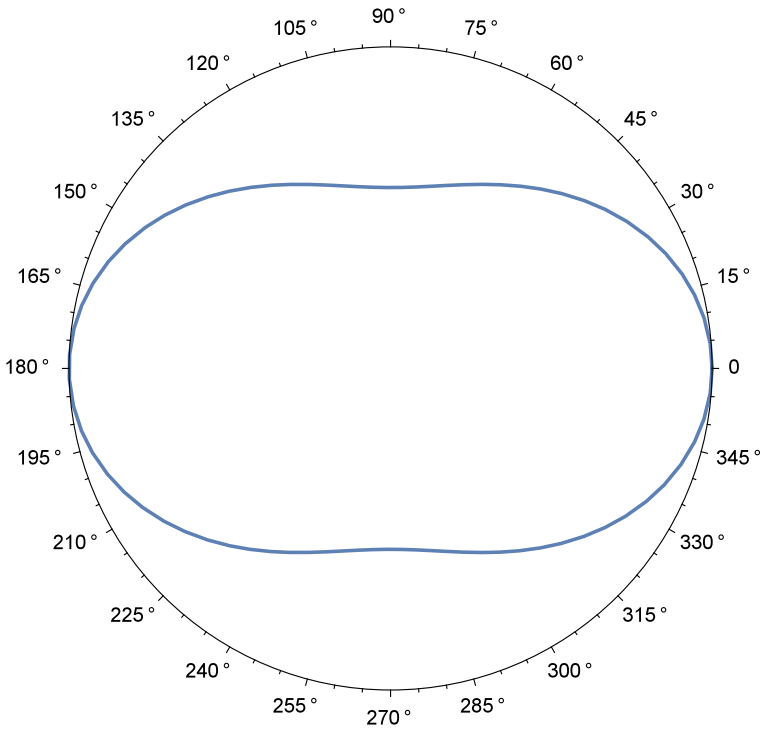

Figure 3.1: The differential cross section for unpolarized initial states with summation over final polarizations without background fields.

The differential cross section for unpolarized initial states with summation over final polarizations is then obtained by averaging over initial polarizations

$$\frac{d\sigma^{\text{unpol}}}{d\Omega} = \frac{1}{(16\pi)^2\omega^2}\frac{1}{4}\sum_{\epsilon_1\epsilon_2\epsilon_3\epsilon_4}|\mathcal{M}_{\epsilon_1\epsilon_2\epsilon_3\epsilon_4}|^2.$$

For light-light scattering this gives the well known result

$$\frac{d\sigma^{\text{unpol}}}{d\Omega}_{B=0} = \frac{139\alpha^4\omega^6}{(180\pi)^2 m^8}(3+\cos^2\eta)^2.$$

Figure 3.1 shows the angular dependence of the cross section given above. The total cross section is given by the solid angle integral

$$\begin{aligned}\sigma &= \frac{1}{2}\int d\Omega\frac{d\sigma}{d\Omega}\\ &= \frac{1}{2}\int d\eta d\theta\sin\eta\frac{d\sigma}{d\Omega}\end{aligned}$$

Table 3.1: The Lagrangian coefficient for (3.3) without the factor $C = \frac{\alpha^2}{m^4}$.

	c_1	c_2	$\hat{c}_1$	$\hat{c}_2$
Spinor QED	$\frac{8}{45}$	$\frac{14}{45}$	$\frac{64}{315}$	$\frac{104}{315}$
Scalar QED	$\frac{7}{90}$	$\frac{1}{90}$	$\frac{31}{315}$	$\frac{11}{315}$
SUSY QED	$\frac{1}{3}$	$\frac{1}{3}$	$\frac{2}{5}$	$\frac{2}{5}$
Charged Vector bosons	$\frac{29}{10}$	$\frac{27}{10}$	$-\frac{137}{105}$	$-\frac{157}{105}$

where the factor of $1/2$ appears because we have identical particles in the final state. With this we obtain

$$\sigma_{B=0}^{\text{unpol}} = \frac{937}{10125}\frac{\alpha^4\omega^6}{\pi m^8}$$

in agreement with the results in the literature (for example [9]).

3.3 Weak Magnetic fields

The case of weak magnetic fields covers background fields with $\xi \ll 1$. In this regime we can use the Taylor expansion for

$$\coth z = \frac{1}{z} + \frac{z}{3} - \frac{z^3}{45} + \dots$$

and

$$\cot z = \frac{1}{z} - \frac{z}{3} - \frac{z^3}{45} - \dots$$

to obtain a weak field approximation of our Lagrangian (1.12).

$$\mathcal{L}^{(1)} = \frac{e^4}{8\pi^2}\int_0^{\inf} ds\, s e^{-m^2 s}\left(\frac{a^4 + 5a^2b^2 + b^4}{45} - (es)^2\frac{2a^6 + 7a^4b^2 - 7a^2b^4 - 2b^6}{945}\right) \pm \dots.$$

This integration can be performed analytically. Using (1.10) and (1.11) we can express the result in terms of the Lorentz invariants $\mathcal{F}$ and $\mathcal{G}$

$$\mathcal{L}^{(1)} = c_1\mathcal{F} + c_2\mathcal{G} - \hat{c}_1\frac{\mathcal{F}^3}{B_c^2} - \hat{c}_2\frac{\mathcal{F}\mathcal{G}^2}{B_c^2} \tag{3.3}$$

With $c_1 = \frac{8}{45}C, c_2 = \frac{14}{45}C, \hat{c}_1 = \frac{64}{315}C, \hat{c}_2 = \frac{104}{315}C$ and $C = \frac{\alpha^2}{m^4}$. (3.3) also describes the weak field Lagrangian for scalar QED, supersymmetric QED and even for charged vector bosons if one chooses the coefficients according to table 3.1.

With this Lagrangian we can obtain an analytical expression for the matrix elements for photons with polarization in (i) and out (o) of the scattering plane for weak magnetic background fields. The curly brackets denote the direction of the magnetic field. The results given show the lowest order correction in the magnetic fields meaning the expression are exact up to correction of order $\mathcal{O}(\xi^4)$. The first, second and third row each show the corresponding terms for magnetic fields in $\hat{x}$, $\hat{y}$ and $\hat{z}$ direction

$$\frac{\mathcal{M}_{oooo}}{\omega^4} = 4c_1(3+\cos^2\eta) + \left\{ \begin{array}{c} -30\hat{c}_1 \\ -30\hat{c}_1 \\ -18\hat{c}_1 + 16\hat{c}_2 \end{array} \right\} \xi^2 + \left\{ \begin{array}{c} 6\hat{c}_1 \\ 42\hat{c}_1 \\ -6\hat{c}_1 \end{array} \right\} \xi^2 \cos^2\eta,$$

$$\frac{\mathcal{M}_{iiii}}{\omega^4} = 4c_1(3+\cos^2\eta) + \left\{ \begin{array}{c} -18\hat{c}_1 + 4\hat{c}_2 \\ -18\hat{c}_1 + 4\hat{c}_2 \\ -66\hat{c}_1 \end{array} \right\} \xi^2 + \left\{ \begin{array}{c} -6\hat{c}_1 - 4\hat{c}_2 \\ -6\hat{c}_1 + 12\hat{c}_2 \\ -6\hat{c}_1 \end{array} \right\} \xi^2 \cos^2\eta,$$

$$\frac{\mathcal{M}_{ooii}}{\omega^4} = -8c_1 + 4c_2(1+\cos^2\eta) + \left\{ \begin{array}{c} -12\hat{c}_1 - 6\hat{c}_2 \\ 24\hat{c}_1 - 2\hat{c}_2 \\ 24\hat{c}_1 - 14\hat{c}_2 \end{array} \right\} \xi^2 + \left\{ \begin{array}{c} 2\hat{c}_2 \\ -14\hat{c}_2 \\ -2\hat{c}_2 \end{array} \right\} \xi^2 \cos^2\eta,$$

$$\begin{aligned} \frac{\mathcal{M}_{iioo}}{\omega^4} =& -8c_1 + 4c_2(1+\cos^2\eta) \\ &+ \left\{ \begin{array}{c} 24\hat{c}_1 - 2\hat{c}_2 \\ -12\hat{c}_1 - 6\hat{c}_2 \\ 24\hat{c}_1 - 14\hat{c}_2 \end{array} \right\} \xi^2 + \left\{ \begin{array}{c} -12\hat{c}_1 - 2\hat{c}_2 \\ 12\hat{c}_1 - 10\hat{c}_2 \\ -2\hat{c}_2 \end{array} \right\} \xi^2 \cos^2\eta, \end{aligned}$$

$$\begin{aligned} \frac{\mathcal{M}_{ioio}}{\omega^4} =& 4(c_1+c_2)(1+\cos\eta) + 2(c_2-c_1)(3+\cos^2\eta) \\ &+ \left\{ \begin{array}{c} 3\hat{c}_1 - 9\hat{c}_2 \\ 3\hat{c}_1 - 9\hat{c}_2 \\ 9\hat{c}_1 - 19\hat{c}_2 \end{array} \right\} \xi^2 + \left\{ \begin{array}{c} -3\hat{c}_1 + \hat{c}_2 \\ -3\hat{c}_1 - 15\hat{c}_2 \\ -9\hat{c}_1 - 5\hat{c}_2 \end{array} \right\} \xi^2 \cos^2\eta \\ =& \frac{\mathcal{M}_{oioi}}{\omega^4}, \end{aligned}$$

$$\mathcal{M}_{iooi/oiio} = \mathcal{M}_{ioio/oioi}\Big|_{\cos\eta\to-\cos\eta}$$

All of the other matrix elements (those with an odd number of i's and o's) vanish identically. Notice that the symmetries $\mathcal{M}_{oooo} = \mathcal{M}_{iiii}|_{B=0}$ and $\mathcal{M}_{iioo} = \mathcal{M}_{ooii}|_{B=0}$ which are valid in vacuum are broken for finite magnetic background fields.

With these matrix elements we can compute the full differential cross section for unpolarized incoming photons and summed over final photon polarizations in a magnetic background with $\mathbf{B} = (B_x, B_y, B_z)$:

$$\begin{aligned}
\frac{d\sigma^{\text{unpol}}}{d\Omega} =& \frac{\omega^6}{256\pi^2}(3c_1^2 - 2c_1c_2 + 3c_2^2)(7+\cos 2\eta)^2 \\
&+ \frac{\omega^6}{512\pi^2}\frac{1}{B_c^2}\Big[\\
&\quad B_x^2(-1017c^1\hat{c}_1 + 327\hat{c}_1c_2 + 161c_1\hat{c}_2 - 391c_2\hat{c}_2 \\
&\quad + (60c_2\hat{c}_1 + 4c_2\hat{c}_2 - 132c_1\hat{c}_1 - 28c_1\hat{c}_2)\cos 2\eta \\
&\quad - (3c_2\hat{c}_1 - c_2\hat{c}_2 - 3c_1\hat{c}_1 - 5c_1\hat{c}_2)\cos 4\eta) \\
&\quad + B_y^2(-1563c^1\hat{c}_1 + 501\hat{c}_1c_2 + 459c_1\hat{c}_2 - 813c_2\hat{c}_2 \\
&\quad + (292c_1\hat{c}_2 - 708c_1\hat{c}_1 + 252c_2\hat{c}_1 - 444c_2\hat{c}_2)\cos 2\eta \\
&\quad + (15c_2\hat{c}_1 - 23c_2\hat{c}_2 - 33c_1\hat{c}_1 + 17c_1\hat{c}_2)\cos 4\eta) \\
&\quad + B_y^2(-1875c^1\hat{c}_1 + 657\hat{c}_1c_2 + 667c_1\hat{c}_2 - 1073c_2\hat{c}_2 \\
&\quad + (108c_2\hat{c}_1 - 420c_1\hat{c}_1 - 204c_2\hat{c}_2 + 100c_1\hat{c}_2)\cos 2\eta \\
&\quad + (c_1\hat{c}_2 - 9c_1\hat{c}_1 + 3c_2\hat{c}_1 - 3c_2\hat{c}_2)\cos 4\eta \\
&\quad + B_xB_y((516c_1\hat{c}_1 - 156\hat{c}_1c_2 - 276c_1\hat{c}_2 + 396c_2\hat{c}_2)\sin 2\eta \\
&\quad + (30c_1\hat{c}_1 - 18\hat{c}_1c_2 - 22c_1\hat{c}_2 + 26c_2\hat{c}_2)\sin 4\eta)\Big] + \mathcal{O}(\xi^4)
\end{aligned}$$

Performing the solid angle integral we obtain the total cross section

$$\begin{aligned}
\sigma^{\text{unpol}} =& \frac{7\omega^6}{20\pi}(3c_1^2 - 2c_1c_2 + 3c_2^2) \\
&+ \frac{\omega^6}{15\pi}\frac{B_x^2}{B_c^2}(-57c_1\hat{c}_1 + 18\hat{c}_1c_2 + 10c_1\hat{c}_2 - 23c_2\hat{c}_2) \\
&+ \frac{\omega^6}{120\pi}\frac{B_y^2 + B_z^2}{B_c^2}(-717c_1\hat{c}_1 + 243\hat{c}_1c_2 + 233c_1\hat{c}_2 - 391c_2\hat{c}_2)
\end{aligned}$$

Inserting the values of spinor QED for $c_1, c_2, \hat{c}_1$ and $\hat{c}_2$ gives

$$\sigma^{\text{unpol}}_{\text{spinor}} = \frac{973\alpha^4\omega^6}{10125\pi m^8}\left(1 - \frac{38224B_x^2 + 65602(B_y^2 + B_z^2)}{20433B_c^2} + \mathcal{O}(\xi^4)\right) \tag{3.4}$$

One thing that is immediately apparent is that the lowest order contribution in the magnetic fields is negative, meaning the cross section seems to be diminishing for stronger fields. However it turns out that for most magnetic field directions there is another effect that kicks in at around $\xi \approx 1$ and which eventually leads to a quadratic growth. We will discuss the reason for this and the behavior at strong fields in chapter 7.

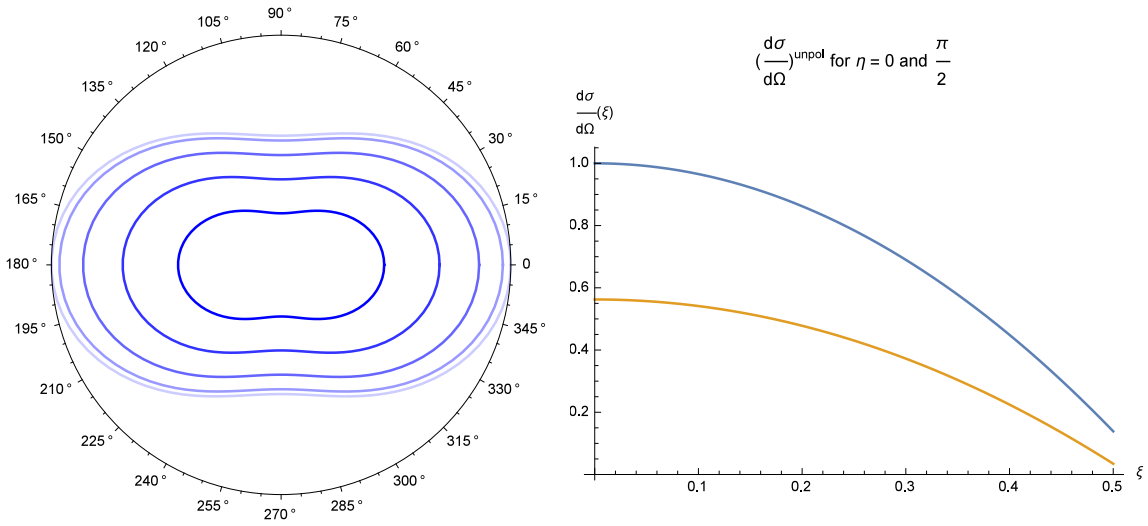

Figure 3.2: The left plot shows the differential cross section for unpolarized initial photons summed over final photons in the weak field approximation for $\mathbf{B} = (0, 0, B)$ with ξ varying from 0 (most transparent) to 0.4 (least transparent). The plot on the right shows the differential cross section as a function of the field strength for the scattering angles 0 (blue) and $\pi/2$ (orange).

We want to explain the case of scattering in a magnetic field perpendicular to the scattering plane in a little bit more detail. This case should serve as an example showing the effects of the magnetic field on the cross section. After setting B_x and B_y to zero the differential cross section simplifies to

$$\begin{aligned}\frac{d\sigma^{\text{unpol}}}{d\Omega} =& \frac{139\alpha^4\omega^6}{(180\pi)^2 m^8}(3+\cos^2\eta)^2 \\ &- \xi^2 \frac{\alpha^4\omega^6}{453600\pi^2 m^8}(86167 + 20756\cos(2\eta) + 341\cos(4\eta)) + \mathcal{O}(\xi^4)\end{aligned}$$

and in particular for forward scattering where $\eta = 0$

$$\frac{d\sigma^{\text{unpol}}}{d\Omega} = \frac{139\alpha^4\omega^6}{(45\pi)^2 m^8}\left[1 - \xi^2\frac{648}{139}\right] + \mathcal{O}(\xi^4)$$

The effect of this quadratic contribution can be seen in figure 3.2.

3.4 Strong magnetic fields

The case of strong magnetic fields covers background fields with $\xi \gg 1$. The plots were all obtained by numerical computations. Analytical results are harder to come

by in this regime however there are some approximations that can be done. The full unrenormalized Euler-Heisenberg term is

$$\mathcal{L}^{(1)}_{\text{spinor}} = -\frac{1}{8\pi^2}\int_0^\infty \frac{ds}{s^3} e^{-m^2 s}\left[(es)^2 ab\cot(ebs)\coth(eas)\right]. \tag{3.5}$$

The variables a and b behave in the limit of $E \to 0$ and $B \to \infty$ (assuming $a, b \geq 0$) according to

$$a = \left[\sqrt{\frac{1}{4}(B^4 - 2B^2E^2 + E^2) + (\mathbf{E}\cdot\mathbf{B})^2} + \frac{1}{2}(B^2 - E^2)\right]^{\frac{1}{2}} \to B,$$
$$b = \left[\sqrt{\frac{1}{4}(B^4 - 2B^2E^2 + E^2) + (\mathbf{E}\cdot\mathbf{B})^2} - \frac{1}{2}(B^2 - E^2)\right]^{\frac{1}{2}} \to 0.$$

Therefore in the limit above we find that

$$\coth(eas) \to 1$$

and therefore for the integrand (3.5)

$$\frac{1}{s^3} e^{-m^2 s}\left[(es)^2 ab\cot(ebs)\coth(eas)\right] \to \frac{1}{s^3} e^{-m^2 s}\left[(es)^2 ab\cot(ebs)\right].$$

point wise. Furthermore we can perform a Taylor expansion in b around $b = 0$ using $\cot(esb) = \frac{1}{esb} - \frac{1}{3}esb - \ldots$.

Using these approximations and renormalizing the theory we obtain a new approximate expression for our Lagrangian

$$\mathcal{L}^{(1)}_{\text{spinor,strong fields}} = \frac{e^2}{360\pi^2} ab^4 \int_0^\infty ds\, s^2 e^{-m^2 s}.$$

This can be integrated analytically and we obtain

$$\mathcal{L}^{(1)}_{\text{spinor,strong fields}} = \frac{e^2}{180\pi^2 m^6} ab^4. \tag{3.6}$$

As we will see, this Lagrangian contains all dominant effects for light-light scattering in the regime for ultra strong magnetic fields.

J. Heyl and L. Hernquist also found an expression for the Euler-Heisenberg Lagrangian in the limit where the component of the electric field parallel to the magnetic field; ultra strong magnetic fields ($B \to \infty$) and vanishing electric fields are a special case. With the assumption given above they found that if the Lagrangian is expressed as a series in $\mathbf{E}\cdot\mathbf{B}$, then the lowest contributions are

$$\begin{aligned}\mathcal{L}^{(1)}_{\text{Spinor}} = \frac{e^2}{2\pi^2 m^6}\Bigg[&a^2\left(\frac{\ln a}{12} - \ln A + \frac{\ln 2}{12}\right) + \frac{a}{4}(\ln a + 1 - \ln\pi) + \frac{\ln a}{8} + \frac{3}{16} \\ &+ \frac{\ln 2 - \gamma}{8} - \frac{b^2}{12}(\ln a + \ln 2 - \gamma) + a\left(\frac{b^2}{12} + \frac{b^4}{90} + \cdots\right) + \cdots\Bigg].\end{aligned} \tag{3.7}$$

Here γ is the Euler-Mascheroni constant and $\ln A$ is defined by

$$\ln A = \frac{1}{12} - \zeta^{(1)}(-1) = 0.24875\ldots \tag{3.8}$$

with the first derivative of the ζ function $\zeta^{(1)}$. The Lagrangian (3.6) is contained in the last term in (3.7).

We will use the Lagrangian (3.6) to obtain a very compact form of the differential cross section for ultra strong magnetic field later. However, first we want to discuss the general features that can be observed in this limit.

3.4.1 Angular dependency of the cross section

We are investigating the angular dependence of the cross section for strong magnetic fields. The angular dependence of the cross section depends heavily on the orientation of the magnetic field. What we find is that scattering processes in which the involved photons (in- and outgoing photons) are moving orthogonal to the magnetic field are amplified and scattering processes in which one of the photons moves parallel to the magnetic field are suppressed. The left plot of figure 3.3 shows the angular

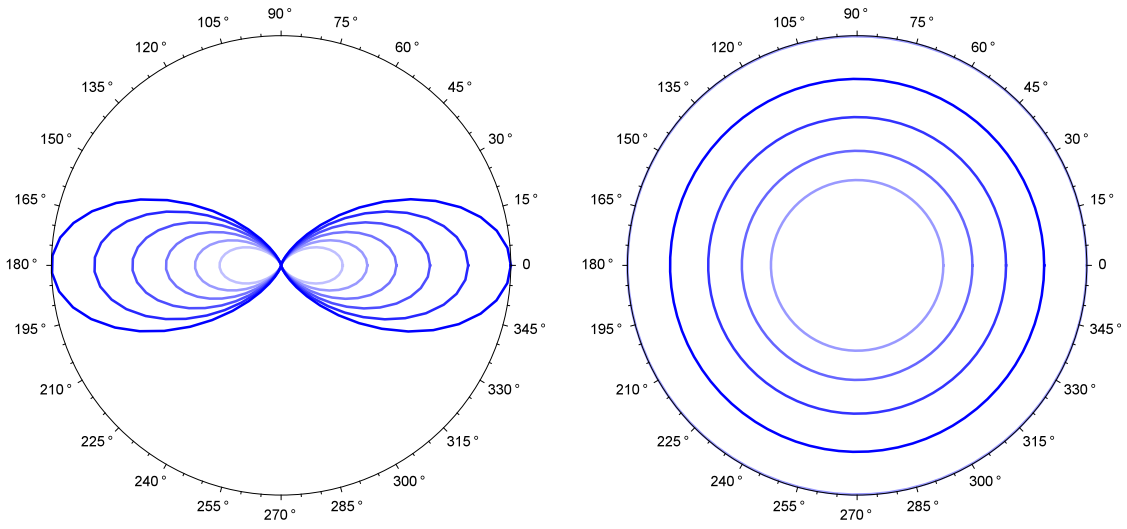

Figure 3.3: The scattering cross sections for $\mathbf{B} = (0, B, 0)$ (left) and $\mathbf{B} = (0, 0, \xi)$ (right) for unpolarized incoming photons and summed over final photons with ξ varying from 6 (most transparent) to 10 (least transparent). The cross section increases quadratically with increasing magnetic fields.

dependence for $\mathbf{B} = (0, B, 0)$ for different ξ. We find quadratic growth of the cross section as a function of the magnetic field strength for every scattering angle except

$\pm\pi/2$ where the outgoing photons propagate parallel to the magnetic field. The maximum amplification is at 0 and π where the angle between scattered photons and the magnetic field vector is maximal.

A special configuration is $\mathbf{B} \parallel \hat{\mathbf{z}}$ where the magnetic field is orthogonal to the scattering plane and scattering in every direction is equally amplified. We then find no angular dependence in the cross section as can be seen in the plot on the right hand side in figure 3.3.

Another special case is for magnetic fields parallel to the incoming photons i.e. $\mathbf{B} \parallel \hat{\mathbf{x}}$, where scattering in every direction is suppressed and the cross section is proportional to $1/\xi^2$. This can be seen in figure 3.4 where we plotted the differential cross section for different magnetic field strengths. Notice that unlike in figure 3.3 the cross section diminishes with growing magnetic field strengths. In the general case where the photons are neither orthogonal nor parallel to the magnetic field the angle to the magnetic field decides the amount of amplification. In general we observe that, except for processes where photons move parallel to the magnetic field, the differential cross section increases quadratically in ξ.

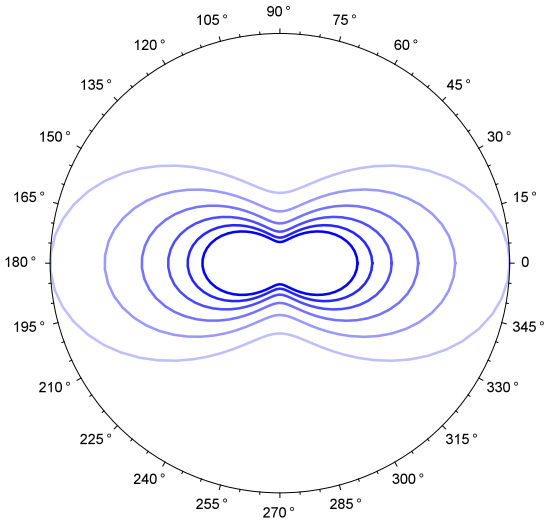

Figure 3.4: The scattering cross sections for $\mathbf{B} = (B, 0, 0)$ for unpolarized incoming photons and summed over final photons with ξ varying from 6 (most transparent) to 10 (least transparent). The cross section decreases quadratically with increasing magnetic fields.

Figure 3.5 shows an example of the general case where the magnetic field is neither orthogonal nor parallel to the scattering plane for three different magnetic field strengths. We find the mentioned quadratic growth for every scattering angle with the maximum amplification at $3\pi/4$ and $-\pi/4$ where the angle between scattered

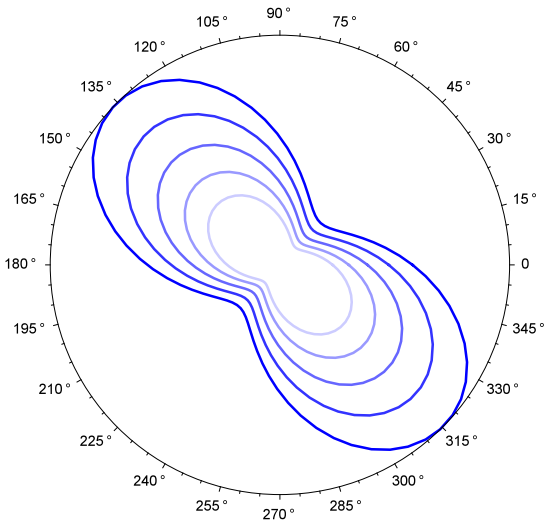

Figure 3.5: The scattering cross sections for $\mathbf{B} = B/2(1, 1, \sqrt{2})$ for unpolarized incoming photons and summed over final photons with ξ varying from 6 (most transparent) to 10 (least transparent). The cross section increases quadratically for every scattering angle

photons and the magnetic field vector is maximal and the minimal amplification at $\pm\pi/4$ where the angle between photons and magnetic field vector is minimal.

A precise formula for the observed behavior can be obtained from our approximation (3.6). We find that for a magnetic field $\mathbf{B} = (B_x, B_y, B_z)$ the asymptotic behavior of the unpolarized scattering cross section summed over final polarizations is given by

$$\frac{d\sigma^{\text{unpol}}_{\text{spinor,strong}}}{d\Omega} \approxeq B^2 \frac{\alpha^5\omega^6}{225\pi m^{12}}(B_y^2 + B_z^2)^2 \times ((B_y^2 - B_x^2)\cos(2\eta) + B_x^2 - 2B_xB_y\sin(2\eta) + B_y^2 + 2B_z^2)^2.$$

which can be further simplified to

$$\frac{d\sigma^{\text{unpol}}_{\text{spinor,strong}}}{d\Omega} \approxeq \frac{\alpha^4\omega^6}{225\pi^2 m^8}\xi^2 \sin^4\alpha \sin^4\beta \tag{3.9}$$

where α and β are the angles between the magnetic field $\mathbf{B}$ and the incoming and outgoing photons $\hat{k}$ and $\hat{k}'$. It shows exactly the features described above and gives the exact coefficient for the quadratic growth in the field strength. Performing the solid angle integral we can compute the total cross section for ultra strong magnetic background fields. We obtain

$$\sigma^{\text{unpol}}_{\text{spinor,strong}} \approxeq \frac{16\alpha^4\omega^6}{3375\pi m^8}\xi^2 \sin^4\alpha, \tag{3.10}$$

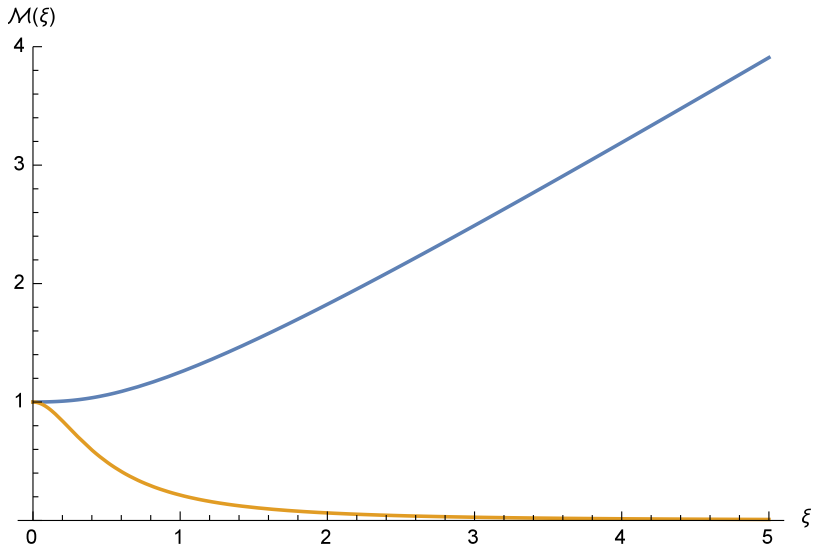

Figure 3.6: The Matrix elements $\mathcal{M}_{oooo}$ and $\mathcal{M}_{iiii}$ for the case of a Magnetic field $\mathbf{B} = (0, 0, B)$ scaled to 1 for $\xi = 0$. The matrix element $\mathcal{M}_{oooo}$ (blue) with all polarizations parallel to the magnetic field shows quadratic growth for small and linear growth for strong magnetic fields. The element $\mathcal{M}_{iiii}$ (orange) with polarizations perpendicular to the magnetic field drops proportional to $1/\xi$ for strong fields.

where α is again the angle between the magnetic field $\mathbf{B}$ and the incoming photons.

3.4.2 Effects for specific polarizations

If the background fields are turned off, matrix elements are identical if every photon polarization is swapped. This means for example that $\mathcal{M}_{oooo} = \mathcal{M}_{iiii}$ for vanishing background fields. Turning on the magnetic field breaks this symmetry. Not only that but in the limit case of strong magnetic fields it is "maximally" broken in the sense that a matrix element where the polarization of every photon is parallel to the magnetic field shows linear growth for strong magnetic field whereas the matrix element where the polarizations of all photons are orthogonal to the magnetic field drops proportional to $1/\xi$. Figure 3.6 shows this for the special case of a magnetic field orthogonal to the scattering plane. What we find is that a matrix element shows no linear growth if and only if the polarizations of the incoming or the outgoing photons are orthogonal to the magnetic field $\mathbf{B}$. Furthermore only scattering processes where some of the photons have polarizations orthogonal to the scattering plane and therefore parallel to the magnetic field show linear growth in the limit of strong fields.

Another effect of the magnetic background is that certain scattering processes that are forbidden in vacuum can take place in a magnetic background. Take for example the scattering process $\gamma_1(o) + \gamma_2(i) \to \gamma_3(i) + \gamma_4(i)$ that is forbidden in vacuum and

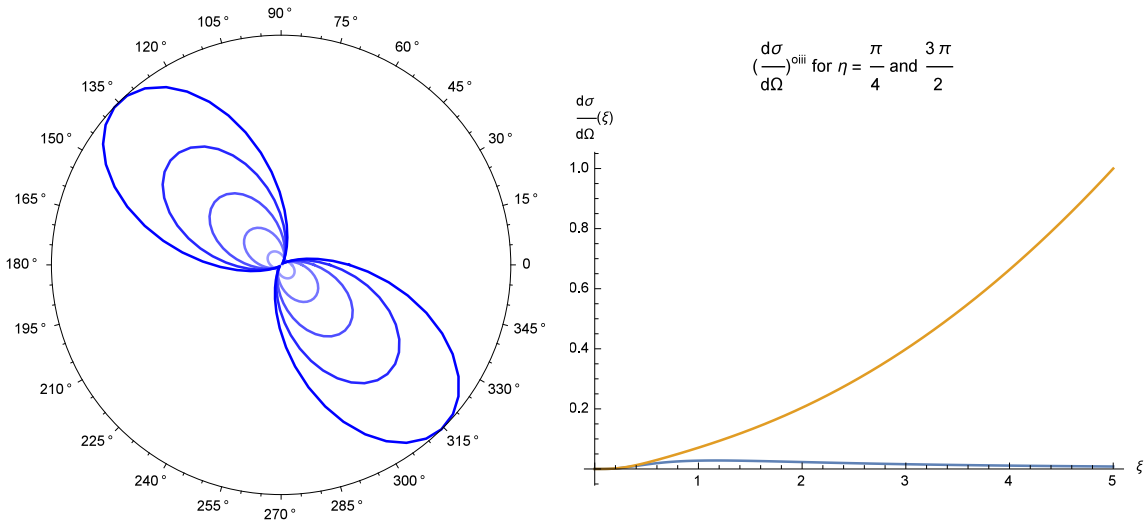

Figure 3.7: The left plot shows the differential cross section of $oi \to ii$ for $\mathbf{B} = B/2(1,1,\sqrt{2})$ with ξ varying from 0 (most transparent) to 5 (least transparent). The plot on the right shows the differential cross section as function of the magnetic field for the scattering angles $\pi/4$ (blue) and $3\pi/4$ (orange).

also for some magnetic field configurations (for example when the field is pointing in $\hat{x}, \hat{y}$ or $\hat{z}$ direction) but for a magnetic field $\mathbf{B} = B/2(1,1,\sqrt{2})$ for which we plotted the differential cross section in figure 3.7 we find a non-vanishing differential cross section for finite field strength that grows quadratically for stronger fields.

We covered all the generic cases (magnetic field in $\hat{x}, \hat{y}$ or $\hat{z}$ direction for different polarizations of the incoming and outgoing photons) in the appendix. We found intricate angular distributions that differ immensely for different polarization configurations. Furthermore for different circular polarization we found no differences in the strong field behavior.

Using the ultra-strong field approximation (3.6) we described in the first chapter we can derive the strong field behavior of a matrix element for $\gamma_1(\epsilon_1) + \gamma_2(\epsilon_2) \to \gamma_3(\epsilon_3) + \gamma_4(\epsilon_4)$. We find that the strong field approximation is given by

$$\mathcal{M}^{\text{spinor,strong}}_{\epsilon_1\epsilon_2\epsilon_3\epsilon_4} \approxeq \frac{32\alpha^2}{15}\left(\frac{\omega}{m}\right)^4 \xi \prod_{I=1}^{4} \epsilon^I \cdot \hat{\mathbf{B}} + \mathcal{O}(1) \tag{3.11}$$

where $\hat{\mathbf{B}} = \mathbf{B}/|\mathbf{B}|$. The formula is in agreement with the observed cross sections discussed above. In the case where all polarizations are orthogonal to the magnetic field the product above equals zero and we find no linear growth in the matrix element. Maximal growth is achieved exactly when all polarizations are parallel to the magnetic

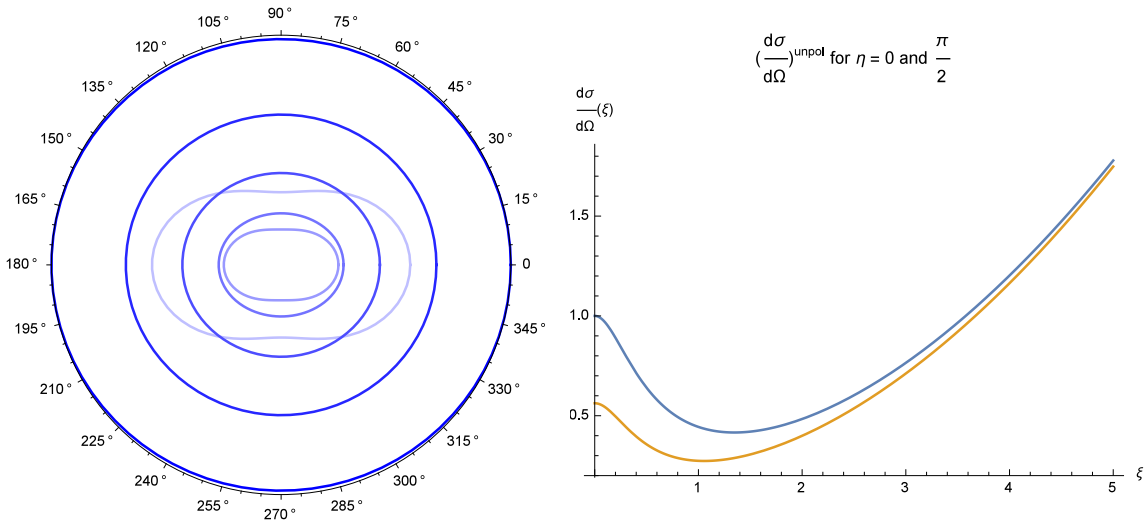

Figure 3.8: The left plot shows the differential cross section for unpolarized photons summed over final polarizations for a magnetic background field $\mathbf{B} = (0, 0, B)$ with ξ varying from 0 (most transparent) to 5 (least transparent). The plot on the right shows the differential cross section as function of the magnetic field for the scattering angles 0 (blue) and $\pi/2$ (orange)

background field.

3.5 Intermediate magnetic field strengths

We saw in the section about weak magnetic fields that the lowest order contribution to the differential cross section leads to a quadratic reduction, however in the limit of strong fields we find quadratic growth in the magnetic field. It is an interesting question to ask what the full picture for arbitrary magnetic fields looks like. The following three figures show the differential cross section for different magnetic field strengths with the magnetic field pointing in $\hat{x}$,$\hat{y}$ and $\hat{z}$ direction.

Figure 3.8 shows the case of a magnetic field in $\hat{z}$ direction. We saw earlier that in this configuration the differential cross section in the strong field limit is independent of the scattering angle. This is clearly visible in the left plot. It is interesting however that the differential cross section decreases and only at a field strength around $\xi \approx 1$ (the exact value depends on the scattering angle) starts to grow.

Similar behavior can be observed in the case where the magnetic field points in $\hat{y}$ direction. This is depicted in figure 3.9. In this case scattering in $\hat{y}$ direction is suppressed by the magnetic field because the outgoing photons point parallel to

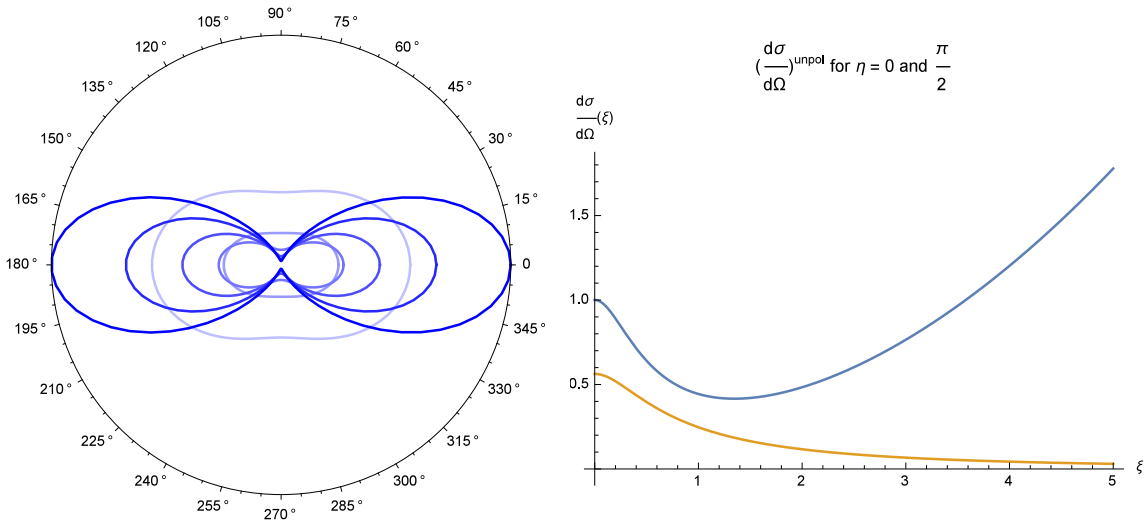

Figure 3.9: The left plot shows the differential cross section for a magnetic background field $\mathbf{B} = (0, B, 0)$ with ξ varying from 0 (most transparent) to 5 (least transparent). The plot on the right shows the differential cross section as function of the magnetic field for the scattering angles 0 (blue) and $\pi/2$ (orange)

the magnetic field. Also the differential cross section for scattering in $\hat{x}$ direction decreases at first until the quadratic growth kicks in at around $\xi \approx 1.35$.

For magnetic fields in $\hat{x}$ direction see figure 3.10. Here scattering in every direction is suppressed because the magnetic field is parallel to the incoming photons. The differential cross section decreases for $\xi \to \infty$ proportional to $1/\xi^2$.

As the last example we show the evolution of the differential cross section for a magnetic field $\mathbf{B} = B/\sqrt{2}(1, 1, 0)$. Figure 3.11 shows the unpolarized cross section for this case for different field strengths. For the limit of strong fields the cross section has the angular distribution described above, however for weaker fields we find that the cross section seems to rotate counter clockwise first and clockwise afterwards. The plot on the right gives some insight in what is happening. Scattering at $\pi/4$ and $3\pi/4$, while being equally likely in vacuum, shows rather different behavior when turning on the magnetic background. While in the limit of strong fields scattering at $3\pi/4$ increases quadratically, for weaker fields it seems to decrease faster as compared to scattering at $\pi/4$.

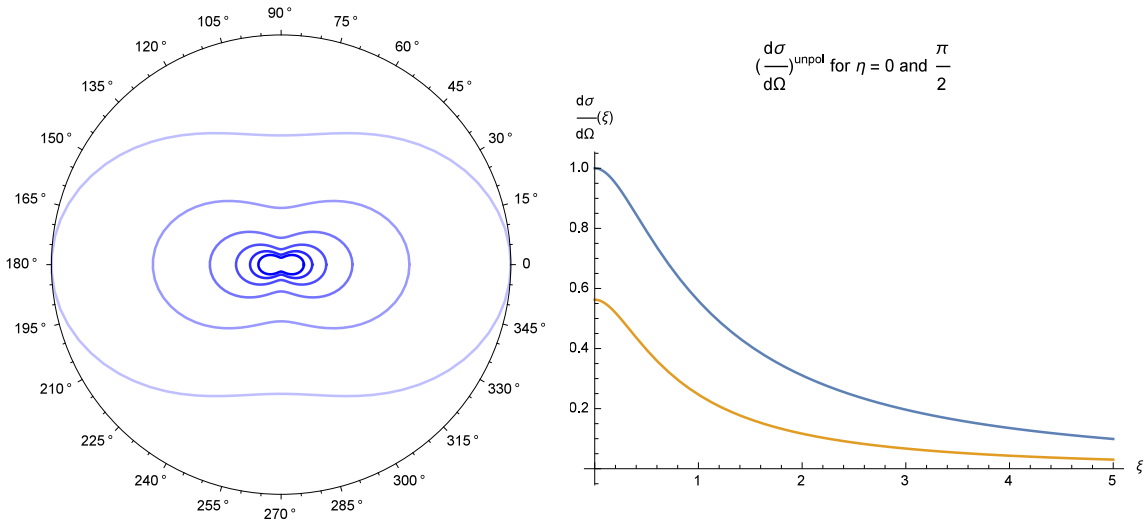

Figure 3.10: The left plot shows the differential cross section for a magnetic background field $\mathbf{B} = (B, 0, 0)$ with ξ varying from 0 (most transparent) to 5 (least transparent). The plot on the right shows the differential cross section as function of the magnetic field for the scattering angles 0 (blue) and $\pi/2$ (orange)

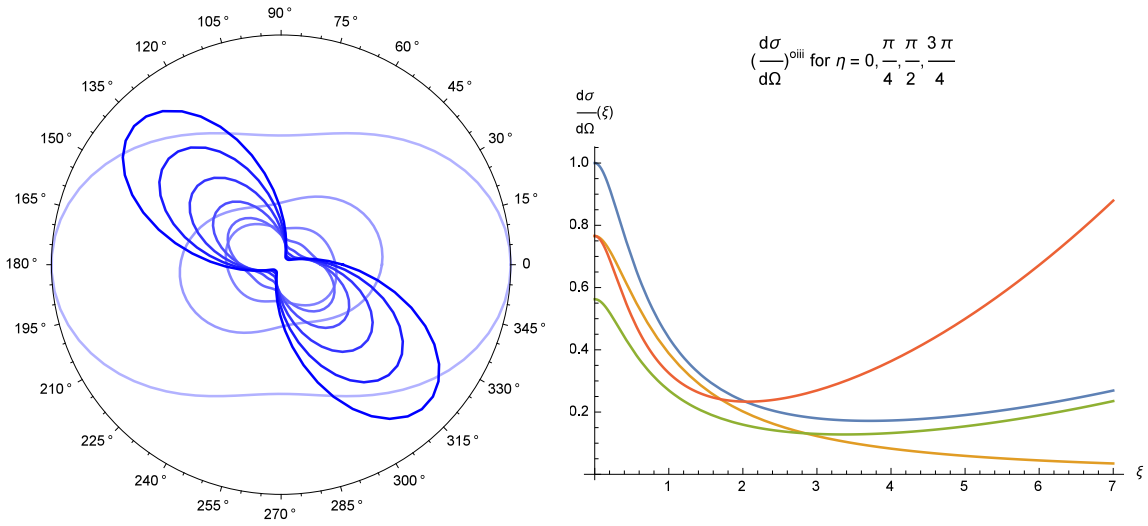

Figure 3.11: The left plot shows the differential cross section for a magnetic background field $\mathbf{B} = B/\sqrt{2}(1, 1, 0)$ with ξ varying from 0 (most transparent) to 5 (least transparent). The plot on the right shows the differential cross section as function of the magnetic field for the scattering angles 0 (blue), $\pi/4$ (orange), $\pi/2$ (green) and $3\pi/4$ (red).

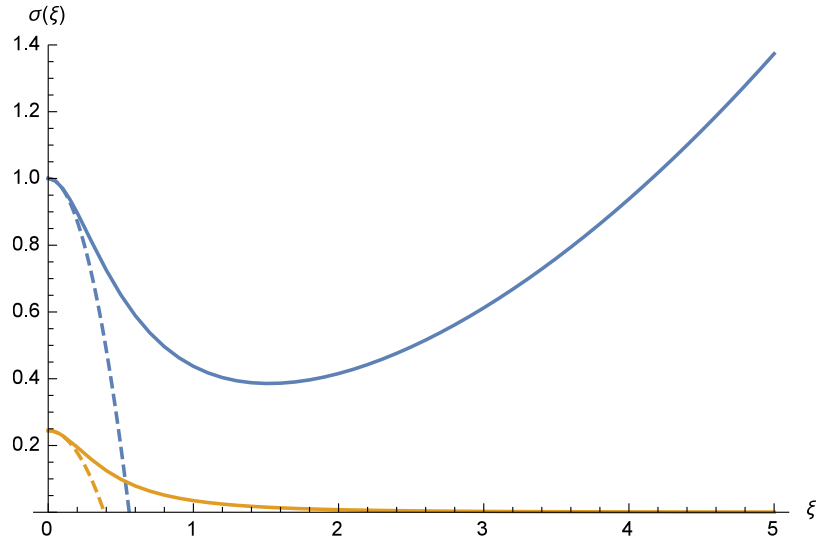

Figure 3.12: The total cross section for a magnetic field orthogonal to the incoming photons for spinor QED (blue) and its weak field approximation (blue dashed) and scalar QED (orange) and its weak field approximation (orange dashed).

Finally we want to present the total cross section as a function of the magnetic field strength for magnetic fields orthogonal and parallel to the collision axis. The case of a orthogonal magnetic field is of particular importance as this is also the field direction (orthogonal to the scattering plane) present at heavy ion collisions at the LHC. We also added the weak field approximation for comparison and the respective total cross section for scalar QED with two complex scalars. The total cross section for the weak field limit was computed analytically using the Lagrangian described above. The general total cross section was computed numerically using Mathematica's built-in functions for numerical integration. Figure 3.12 shows the the result of these computations for a magnetic field orthogonal to the incoming photons and ξ from 0 to 5 scaled to the total cross section for spinor QED in vacuum. For spinor QED the strong field behavior shows quadratic growth, for small field strengths we find that it decreases quadratically and in agreement with the results from the weak field approximation. For the scalar case we find that it decreases rapidly for large field strengths. We will discuss this in the next chapter. Figure 3.13 shows the total cross section for a magnetic field in $\hat{x}$ direction i.e. parallel to the collision axis. Here the total cross section decreases for growing field strength.

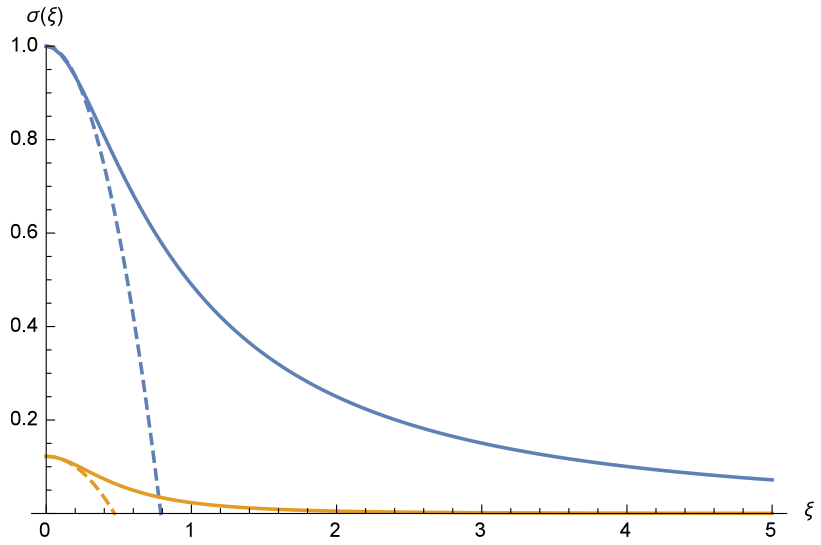

Figure 3.13: The total cross section for a magnetic field parallel to the incoming photons for spinor QED (blue) and its weak field approximation (blue dashed) and scalar QED (orange) and its weak field approximation (orange dashed).

Chapter 4

Results for scalar QED

4.1 Method

The computations (not the results) for the case of scalar QED are almost identical to spinor QED with the only difference being the different Lagrangian. Again we used Mathematica 10.1 and the built-in functions for numerical integration for the numerical results. We evaluated the matrix element for the case of $\mathbf{E} = \mathbf{0}$ and a spatially homogeneous magnetic background field and used the same evaluation methods as described in the section for spinor QED.

4.2 No background fields

We found for the differential cross section for unpolarized initial photons and summed over final photons the expression

$$\frac{d\sigma}{d\Omega} = \frac{17\alpha^4\omega^6}{2(180\pi)^2 m^8}(3+\cos^2\eta)^2 \tag{4.1}$$

It has the same angular dependency (see figure 3.1) as in the spinor case but has a smaller absolute value. With this we obtained the total cross section by performing the solid angle integration

$$\sigma = \frac{1}{2}\int d\Omega \frac{d\sigma}{d\Omega} = \frac{119}{20250}\frac{\alpha^4\omega^6}{\pi m^8} \tag{4.2}$$

Comparing this with the case of spinor QED we find that the total cross section of scalar QED is about 6.4% of the one for spinor QED i.e.

$$\frac{\sigma_{\text{scalar}}}{\sigma_{\text{spinor}}} \approx 0.064 \tag{4.3}$$

4.3 Weak Magnetic fields

Here we discuss the effects for $\xi \ll 1$. As in the spinor case we can Taylor expand the Lagrangian 1.13 using

$$\sinh z = z + \frac{1}{6}z^3 + \frac{1}{120}z^5 + \dots \tag{4.4}$$

and

$$\sin z = 1 - \frac{1}{6}z^3 + \frac{1}{120}z^5 + \dots . \tag{4.5}$$

The Taylor expanded Lagrangian can be integrated analytically and we arrive at expression 3.3 with $c_1 = \frac{7}{90}C$, $c_2 = \frac{1}{90}C$, $\hat{c}_1 = \frac{31}{315}C$, $\hat{c}_2 = \frac{11}{315}C$ and $C = \frac{\alpha}{m^4}$ in agreement with table 3.1. Using the general results we computed in the chapter for spinor QED we can obtain the results for scalar QED by using the appropriate values for $c_1, c_2, \hat{c}_1$ and $\hat{c}_2$.

Doing this we obtain the total cross section for unpolarized incoming photons summed over the polarizations for outgoing photons in scalar QED

$$\sigma^{\text{unpol}}_{\text{scalar QED}} = \frac{119\alpha^4\omega^6}{20250\pi m^8}\left(1 - \frac{11294B_x^2 + 16802(B_y^2 + B_z^2)}{20433B_c^2}\right). \tag{4.6}$$

Comparing this with 3.4 we find that the coefficients of the second order corrections are approximately twice as big, meaning the cross section in the scalar case decreases faster with rising magnetic field strengths then in the case of spinor QED.

4.4 Strong magnetic fields

In the discussion of strong magnetic fields in the spinor case we derived a very simple Lagrangian by taking the asymptotic version of the integrand of the Euler-Heisenberg Lagrangian. Performing the same naive computation in the scalar case we find that in the limit of vanishing electric and ultra-strong magnetic field, i.e. $B \to \infty, E \to 0$ which implies $a \to \infty, b \to 0$, the integrand converges point wise to 0 with the asymptotic behavior proportional to $(eas)e^{-eas}$.

This leads us to expect that the strong field behavior in the scalar case is significantly different from the spinor case. And indeed, the quadratic growth of the cross section could not be observed for any configuration of the magnetic background field. This means the quadratic growth is not a generic feature but originates from the interaction of the magnetic field with the magnetic moment of the virtual particles of spinor QED. We will discuss this in more detail later, for now we want to present the behavior of the differential cross section for unpolarized photons summed over final photon polarizations for different directions and magnitudes of the magnetic background.

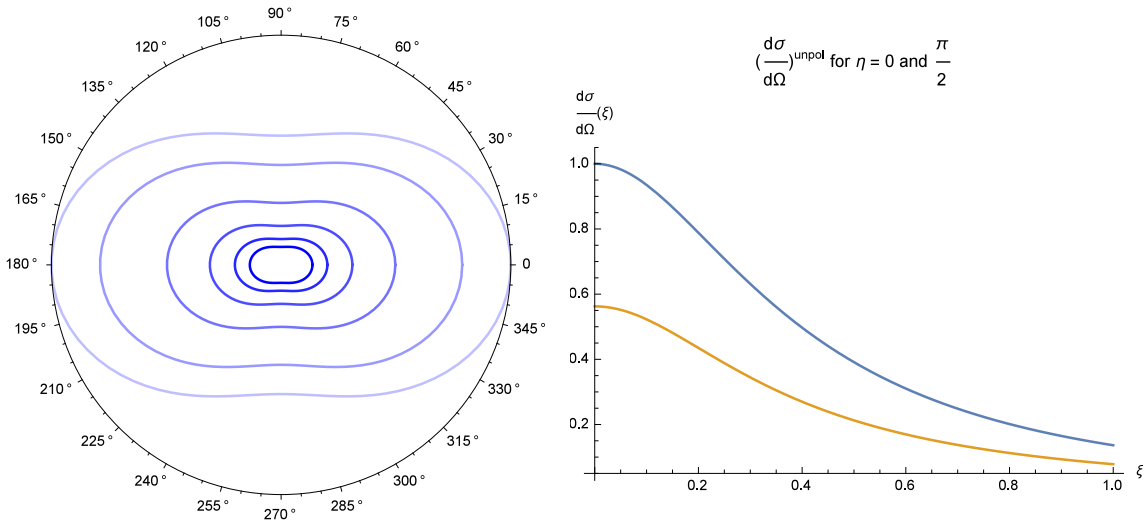

Figure 4.1: The left plot shows the differential cross section for unpolarized photons summed over final polarizations for a magnetic background field $\mathbf{B} = (0, 0, B)$ with ξ varying from 0 (most transparent) to 1 (least transparent). The plot on the right shows the differential cross section as function of the magnetic field for the scattering angles 0 (blue) and $\pi/2$ (orange)

4.5 Intermediate magnetic field strengths

The figures 4.1, 4.2 and 4.3 show each the differential cross section for magnetic field strengths varying from $\xi = 0$ to $\xi = 1$. The graph on the right shows the differential cross section for scattering at angles 0 and $\pi/2$ as a function of the magnetic field strength ξ. We find that contrary to the case of spinor QED the differential cross section does not exhibit the quadratic growth for strong magnetic fields. Instead the differential cross section decreases proportional to $1/\xi^4$. Notice that this is an even faster decline than in the cases in spinor QED for which scattering is suppressed; there we only found that the differential cross section decreased proportional to $1/\xi^2$.

In figure 4.4 we want to show the behavior in the somewhat general case of the magnetic background field $\mathbf{B} = B/2(1, 1, \sqrt{2})$ for field strengths of $\xi = 8, 9, 10$ to demonstrate that the features described above still hold for larger field strengths. The graph on the right hand side of the figure showing the differential cross section as a function of the field strength is scaled to the differential cross section at $\xi = 0$ for better comparison with the figures above. Notice that while in the spinor case (3.5) the differential cross section showed a clear orientation with regards to the magnetic field direction (The maxima were exactly in the directions with the biggest angle between photons and the magnetic field and the minima in the directions with the

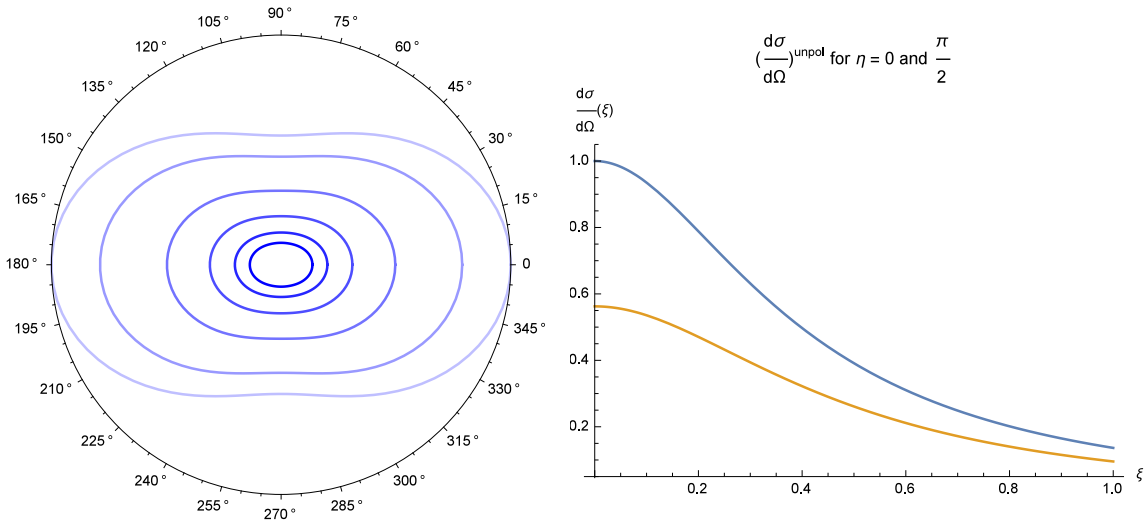

Figure 4.2: The left plot shows the differential cross section for a magnetic background field $\mathbf{B} = (0, B, 0)$ with ξ varying from 0 (most transparent) to 1 (least transparent). The plot on the right shows the differential cross section as function of the magnetic field for the scattering angles 0 (blue) and $\pi/2$ (orange)

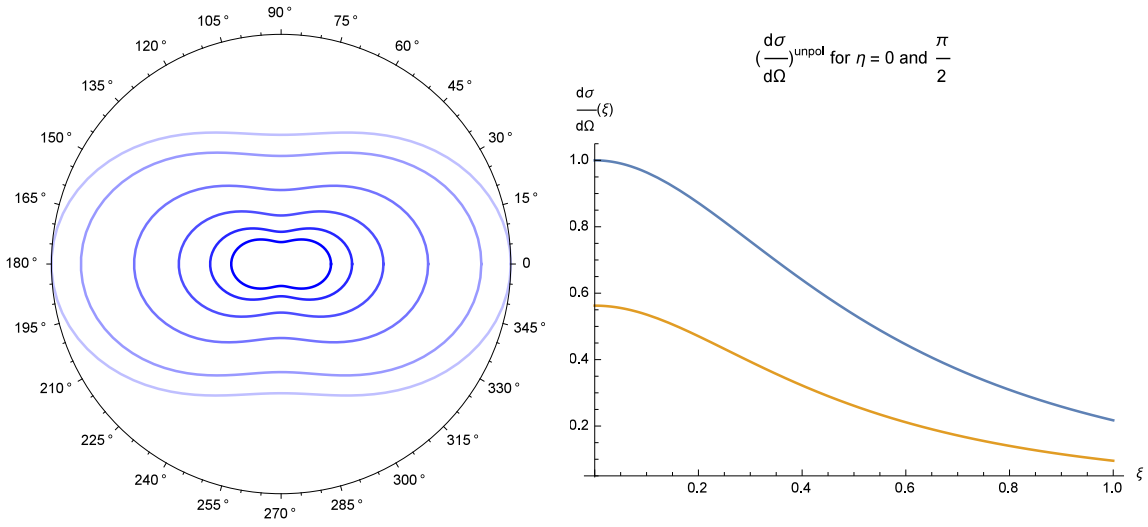

Figure 4.3: The left plot shows the differential cross section for a magnetic background field $\mathbf{B} = (B, 0, 0)$ with ξ varying from 0 (most transparent) to 1 (least transparent). The plot on the right shows the differential cross section as function of the magnetic field for the scattering angles 0 (blue) and $\pi/2$ (orange)

smallest angle) in the scalar case the angular distribution of the cross section seems to be only slightly affected by the direction of the magnetic field.

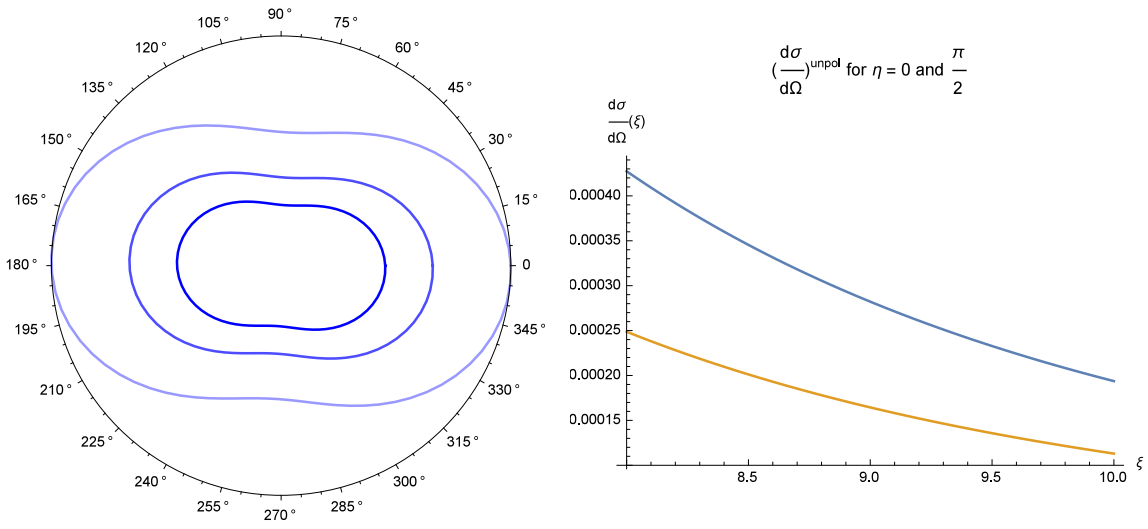

Figure 4.4: The left plot shows the differential cross section for a magnetic background field $\mathbf{B} = B/2\,(1, 1, \sqrt{2})$ with ξ varying from 8 (most transparent) to 10 (least transparent). The plot on the right shows the differential cross section as function of the magnetic field scaled to the value at $\xi = 0$, for the scattering angles 0 (blue) and $\pi/2$ (orange)

Chapter 5

Results for SUSY QED

Supersymmetric QED is a theory with two charged scalar particles and one charged Dirac fermion. It turns out that the cross section for vanishing background fields has an especially simple analytical form as was discussed in [16]. It reads

$$\sigma^{\text{unpol}}_{\text{SUSY QED}} = \frac{7\alpha^4\omega^6}{45\pi m^8}. \tag{5.1}$$

Comparing this with the result for spinor and scalars we find that the total cross section is significantly increased:

$$\frac{\sigma^{\text{unpol}}_{\text{SUSY QED}}}{\sigma^{\text{unpol}}_{\text{spinor QED}}} \approx 1.68$$
$$\frac{\sigma^{\text{unpol}}_{\text{SUSY QED}}}{\sigma^{\text{unpol}}_{\text{scalar QED}}} \approx 26.47$$

To find the cross section for non-vanishing magnetic background fields we can use the general expression that was already evaluated in the chapter about spinor QED. Inserting the corresponding values for SUSY QED from table 3.1 gives the total cross section for unpolarized initial photons summed of final photon polarizations

$$\sigma^{\text{unpol}}_{\text{SUSY QED}} = \frac{7\alpha^4\omega^6}{45\pi m^8}\left(1 - \frac{104B_x^2 + 158(B_y^2 + B_z^2)}{35B_c^2} + \mathcal{O}(\xi^4)\right), \tag{5.2}$$

which has a somewhat simpler form than the corresponding results in spinor and scalar QED. Again, it decreases quadratically for weak magnetic fields.

An interesting feature of SUSY QED that appears for weak magnetic fields is that for some configurations we find that scattering processes are forbidden that are allowed in spinor and scalar QED. Take for example the scattering process $\gamma_1(i) + \gamma_2(i) \to \gamma_3(o) + \gamma_4(o)$ in SUSY QED (Figure A.4.1) where scattering at $B = 0$ in $\hat{x}$ direction is forbidden, even though this process is allowed in spinor (Figure A.2.1)

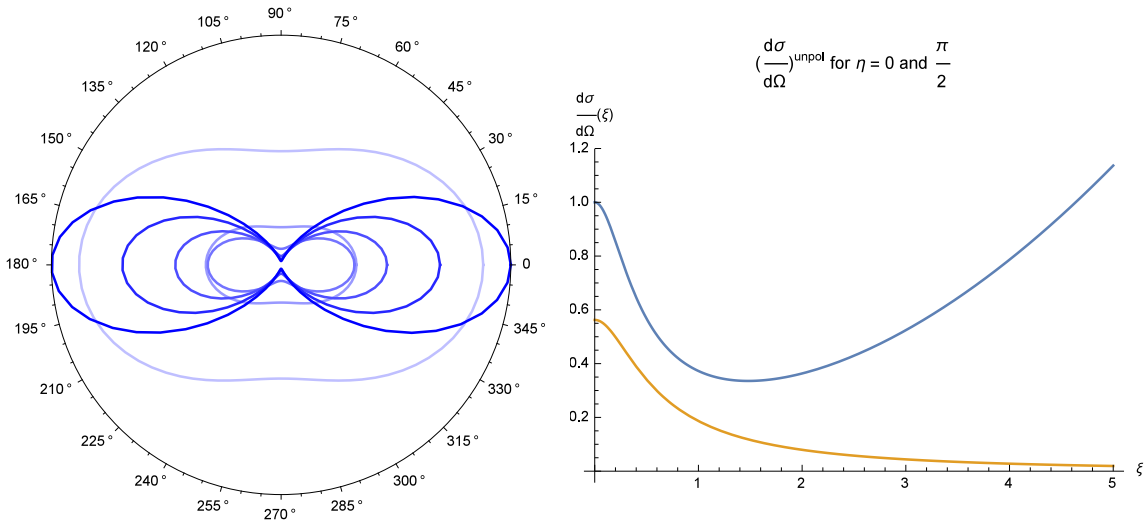

Figure 5.1: The left plot shows the differential cross section for a magnetic background field $\mathbf{B} = (0, B, 0)$ with ξ varying from 0 (most transparent) to 5 (least transparent). The plot on the right shows the differential cross section as function of the magnetic field for the scattering angles 0 (blue) and $\pi/2$ (orange)

and scalar QED (Figure A.3.1). Furthermore if we turn on the magnetic field we find that for $\xi \approx 0.7$ scattering in $\hat{y}$ is again forbidden in SUSY and allowed in spinor and scalar QED. We find destructive interference between the scalar and the fermion content.

For strong magnetic fields we saw in the last chapter that the differential cross section for scalar QED decreases rapidly for strong magnetic background fields. This means the strong field behavior of SUSY QED is completely dominated by the Dirac fermion. It shows the same quadratic growth as spinor QED.

We want to show the behavior by taking a look at the case of a magnetic background field in $\hat{y}$ direction. This can be seen in figure 5.1. Comparing this with figures 3.9 and 4.2 for the respective plots for spinor and scalar QED we see that it decreases faster for weak fields but for strong fields it shows the same behavior as spinor QED, i.e. quadratic growth for every scattering angle expect $\pm\pi/2$ where we find that the differential cross section decreases proportional to $1/\xi^2$.

For the sake of consistency and so that this thesis can be used as an atlas for light-light scattering cross sections we produced the plots for magnetic fields in $\hat{x}$ (Figure 5.2) and $\hat{z}$ (Figure 5.3) direction.

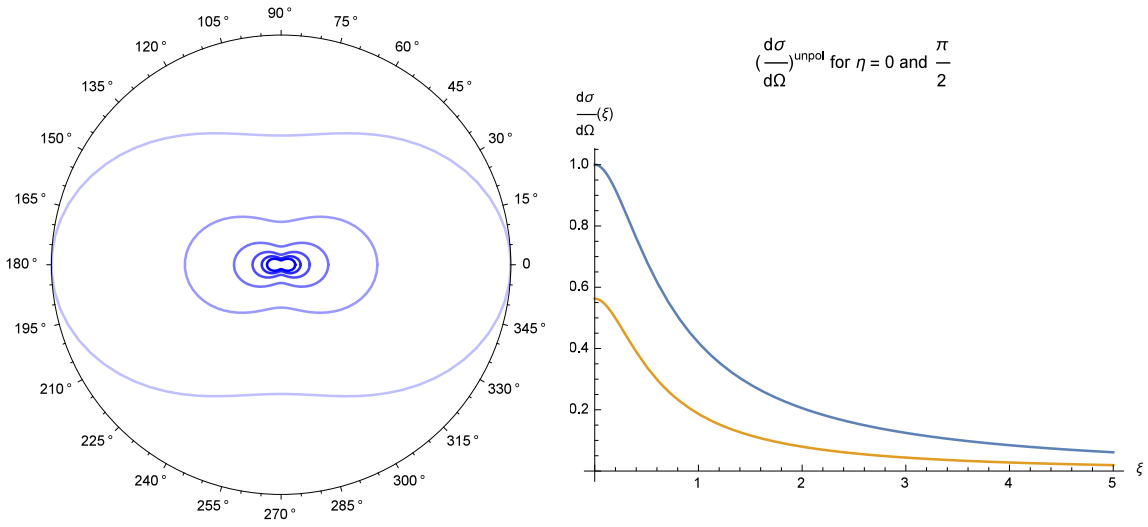

Figure 5.2: The left plot shows the differential cross section for a magnetic background field $\mathbf{B} = (B, 0, 0)$ with ξ varying from 0 (most transparent) to 5 (least transparent). The plot on the right shows the differential cross section as function of the magnetic field for the scattering angles 0 (blue) and $\pi/2$ (orange)

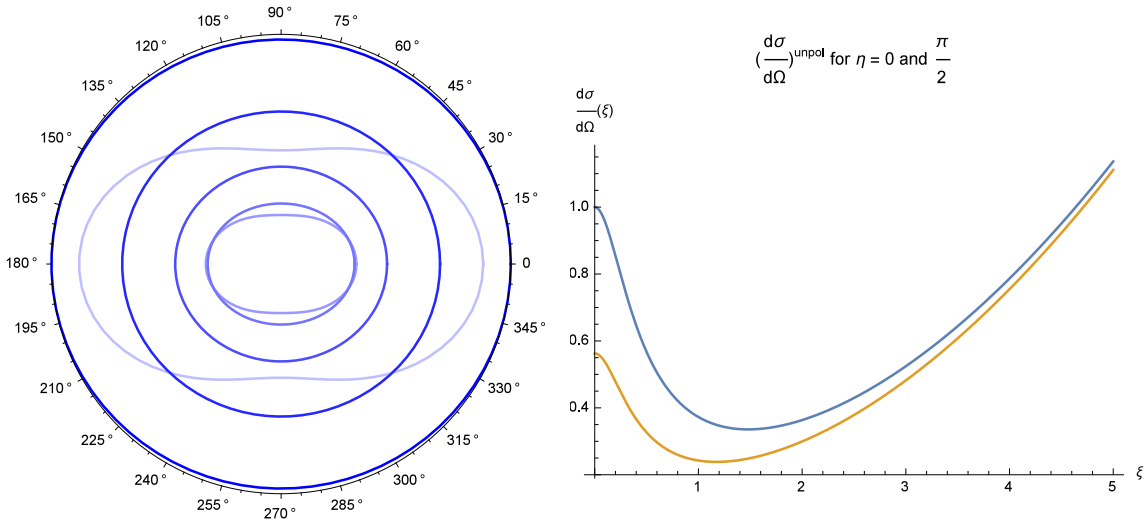

Figure 5.3: The left plot shows the differential cross section for a magnetic background field $\mathbf{B} = (0, 0, B)$ with ξ varying from 0 (most transparent) to 5 (least transparent). The plot on the right shows the differential cross section as function of the magnetic field for the scattering angles 0 (blue) and $\pi/2$ (orange)

Chapter 6

Results for vector QED

In this chapter we want to investigate the scattering behavior in a theory of charged vector particles with a gyromagnetic ratio of $g = 2$. For this case an effective one-loop Lagrangian was first described by Vanyashin and Terent'ev in [14] where they found that the Lagrangian has the integral representation

$$\begin{aligned}\mathcal{L}^{(1)} = \frac{e^2}{4\pi^2}\int_0^\infty \frac{ds}{s}\left[e^{-im^2 s}\,a\left(b\,\frac{\sin eas}{\sinh ebs} - a\right) - e^{-m^2 s}\,b\left(a\,\frac{\sin ebs}{\sinh eas} - b\right)\right] \\ + \frac{3}{16\pi^2}\int_0^\infty \frac{ds}{s}e^{-m^2 t}\left(\frac{e^2 ab}{\sin ebs\sinh eas} - \frac{1}{s^2} - \frac{e^2}{6}(b^2 - a^2)\right).\end{aligned} \tag{6.1}$$

The mass always carries an infinitesimal $-i\epsilon$ to ensure the correct boundary conditions; this also ensures convergence of the integral.

Again we performed the Taylor expansion around $b = 4$ up to fourth order. After the expansion the first of the three terms in the Lagrangian (the term with a complex exponential) can be integrated analytically. This way we do not have to tackle the difficult problem of numerically integrating the first, highly oscillatory, term. After the Taylor expansion, integration and taking the limit to an infinitesimal ϵ (hidden in m) the first term can be written as

$$\begin{aligned}-\frac{ae}{8\pi^2}\left(ae\log\left(1 - a^2\frac{e^2}{m^4}\right) - m^2\log\left(1 - a\frac{e}{m^2}\right) + m^2\log\left(1 + a\frac{e}{m^2}\right) - 2ae\right) \\ -b^2\frac{a^2e^4}{24\pi^2(a^2e^2 - m^4)} + b^4\frac{7a^2e^6(a^2e^2 + 3m^4)}{720\pi^2(m^4 - a^2e^2)} + \mathcal{O}(b^6),\end{aligned} \tag{6.2}$$

the rest of the Lagrangian was integrated numerically.

It should be noted that the Taylor expansion does not mean that the cross section computed will only be an approximation. The cross section can be written as a function of the Lagrangian derivatives with respect to a and b up to fourth order evaluated at $b = 0$. But because the nth coefficient in the Taylor expansion is anyway

the nth derivative of the Lagrangian evaluated at 0 the derivatives of the Taylor expanded Lagrangian coincide with the derivatives of the original Lagrangian at $b = 0$.

The b independent part of the Lagrangian has a non-zero imaginary part for $a > \frac{e}{m^2} = B_c$. Furthermore, as we will see below, the cross section blows up at $\xi = 1$. The theory seems to describe a false vacuum for $a > B_c$. We believe that this, and the behavior at $\xi = 1$ is related to the phase transition to superconductivity that is proposed in [17] where it was found that the vacuum of charged vector particles with a gyromagnetic ratio of $g = 2$ in a strong magnetic fields seems to be unstable towards a superconducting phase.

It should be noted here that the Lagrangian we used describes a pointlike particle. An interpretation of our findings for composite particles like rho mesons (as considered in [17]) is only justified for photons with sufficiently big wavelengths so that the substructure of the vector particles becomes irrelevant.

Before we present the numerical results let us discuss the total cross section in the weak field limit. This can be obtained from our general expression by inserting the values from table 3.1. We obtain for the total cross section

$$\sigma^{\text{unpol}}_{\text{vector QED}} = \frac{2751\alpha^4\omega^6}{250m^8\pi}\left(1 + \frac{211846B_x^2 + 318298(B_y^2 + B_z^2)}{173313B_c^2}\right) \tag{6.3}$$

The lowest order correction to the total cross section for small field strengths is positive! This means the cross section increases compared to the cases of spinor, scalar and SUSY QED discussed above where we found that small magnetic fields act decreasing on the total cross section. Comparing the cross section at $B = 0$ with the corresponding value for spinor QED we find that

$$\frac{\sigma^{\text{unpol}}_{\text{vector QED}}}{\sigma^{\text{unpol}}_{\text{spinor QED}}} \approx 114.5 \tag{6.4}$$

We plotted the total cross section for $0 < \xi < 1$ in figure 6.1. It shows the total cross section for a magnetic field orthogonal (blue) and parallel (orange) to the scattering axis and also the respective weak field approximations (dashed). We find that the weak field limit is a good approximation for $\xi \lessapprox 0.2$. The cross section grows faster for a magnetic field orthogonal to the scattering axis. As described above for $\xi \to 1$ the cross section diverges.

It should be noted that this divergence does not result from numerical errors as it is also present when one analytically investigates the derivatives of the first, analytically integrated, term of the Lagrangian given in (6.2). It is therefore indicative of the breakdown of perturbation theory and the results for the calculations close to the critical field strength and for $\xi > 1$ might not draw the exact picture anymore. This can also be seen in the Lagrangian, where we observe a non-zero imaginary part for

$\xi > 1$ where the cross section diverges. The imaginary part of the Lagrangian can be seen indicative of an unstable false vacuum in this regime.

Nevertheless we still want to present our computations of the total cross section for the case of magnetic fields stronger than the critical field strength i.e. $\xi > 1$ while keeping in mind that the behavior of the cross section around $\xi = 1$ results from a breakdown of perturbation theory.

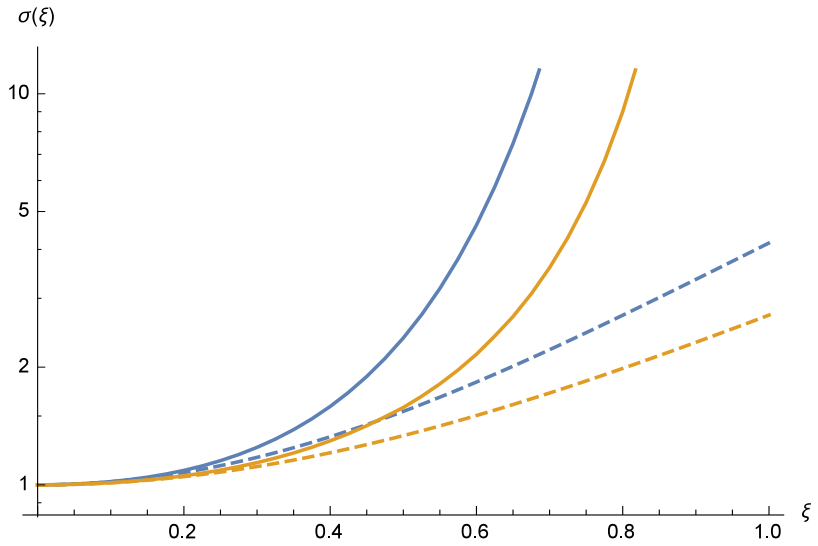

Figure 6.1: The total cross section for $0 < \xi < 1$ scaled to the value for $\xi = 0$ for a magnetic field orthogonal (blue) and parallel (orange) to the scattering axis with the respective weak field approximations (dashed) on a logarithmic scale.

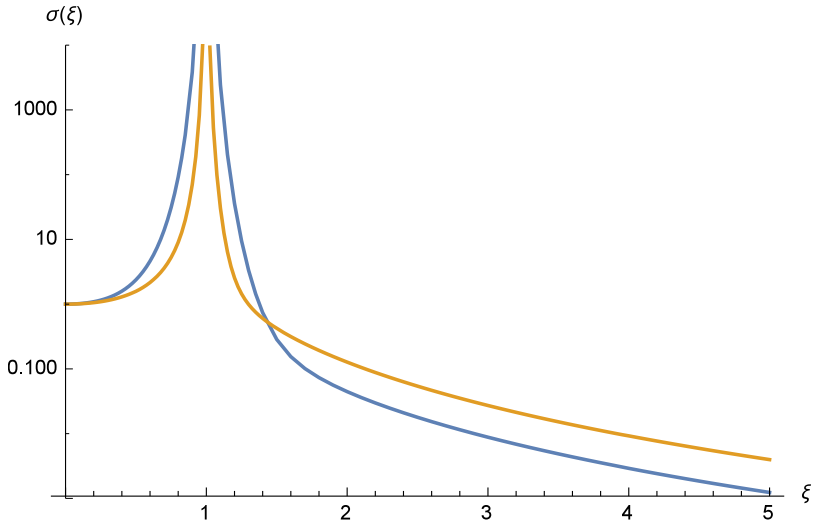

Figure 6.2: The total cross section scaled to the value for $\xi = 0$ for magnetic fields orthogonal (blue) and parallel (orange) to the scattering axis for $0 < \xi < 5$ with

logarithmic scale.

This case is plotted in figure 6.2 for magnetic fields orthogonal (blue) and parallel (orange) to the scattering axis. The plot also shows better the faster divergence in the case of a magnetic field orthogonal to the scattering axis.

Finally, we also plotted the cross sections for the non-vanishing matrix elements in the cases of magnetic fields in $\hat{x}$, $\hat{y}$ and $\hat{z}$ direction in the appendix. Note that in these plots the plot in the middle, showing the behavior of the cross section as a function of the magnetic field strength, has logarithmic scale unlike the plots for spinor, scalar and SUSY QED.

Chapter 7

Discussion

We saw in the chapters above that for SUSY and spinor QED the cross section for unpolarized incoming and averaged over final photons grows quadratically in the magnetic field strength in the limit of strong fields. However in the case of scalar QED this is not the case, as the cross section was found to diminish proportional to $1/\xi^4$. It is therefore natural to assume that the interaction of the spin of the Dirac fermions with the magnetic background field is responsible for the quadratic growth.

To see that this is indeed the case we will use the so-called world-line approach to QED. The formalism was invented by Richard Feynman and presented the first time in the appendix of his famous papers about QED [6, 18]. An overview of the worldline formalism and how it can be used in QED can be found in [19, 20, 21, 7]. We will present the computation for spinor QED. The case of scalar QED can be obtained from this case by ignoring the spin term in the end. A full derivation for scalar QED can be found in [9].

To start we need to derive the worldline formulation for the effective one-loop action in a constant homogeneous background field for QED. This means we want an expression for $\Gamma = \int d^4x \mathcal{L}_{\text{eff}}$ so that[1]

$$\int \mathcal{D}A \, \exp(i\Gamma[A_\mu]) = \int \mathcal{D}A \, \mathcal{D}\bar{\psi} \, \mathcal{D}\psi \, \exp\left[i \int d^4x \Big(-\frac{1}{4} F_{\mu\nu}F^{\mu\nu} + \bar{\psi}(i\not{D} - m)\psi \Big) \right] \tag{7.1}$$

From this we can deduce

$$\exp(i\Gamma[A_\mu]) = \int \mathcal{D}\bar{\psi} \, \mathcal{D}\psi \, \exp\left[i \int d^4x \Big(-\frac{1}{4} F_{\mu\nu}F^{\mu\nu} + \bar{\psi}(i\not{D} - m)\psi \Big) \right] \tag{7.2}$$

To evaluate the integral we note that for n complex Grassmann variables ψ_i and a

[1] To ensure correct boundary conditions one has to set $m \to m - i\varepsilon$. Unless stated otherwise we will always mean $m - i\epsilon$ when we write m for the rest of the article.

Matrix M_{ij} we obtain for the Gaussian integral

$$\int d^n\bar{\psi}\, d^n\psi\, \exp\bigl(-i\bar{\psi}_i M_{ij}\psi_j\bigr) \propto \det M.$$

For Dirac fields the index becomes a continuous index and for $i\not{D}-m \mathrel{\hat{=}} M_{ij}$ we obtain the functional determinant

$$\int \mathcal{D}\bar{\psi}\,\mathcal{D}\psi\, \exp\left[i\int d^4x\Bigl(\bar{\psi}(i\not{D}-m)\psi\Bigr)\right] = \mathcal{N}\det\bigl(i\not{D}-m\bigr),$$

where the proportionality constant $\mathcal{N}$ is fixed by normalization. With this we get

$$\begin{aligned}\exp(i\Gamma[A_\mu]) &= \int \mathcal{D}\bar{\psi}\,\mathcal{D}\psi\, \exp\left[i\int d^4x\Bigl(-\frac{1}{4}F_{\mu\nu}F^{\mu\nu}+\bar{\psi}(i\not{D}-m)\psi\Bigr)\right]\\ &= \mathcal{N}\exp\left[i\int d^4x\Bigl(-\frac{1}{4}F_{\mu\nu}F^{\mu\nu}\Bigr)\right]\det\bigl(i\not{D}-m\bigr),\end{aligned}$$

and thus

$$\exp\left[i\Gamma[A_\mu]+i\int d^4x\frac{1}{4}F_{\mu\nu}F^{\mu\nu}\right] = \mathcal{N}\det\bigl(i\not{D}-m\bigr). \tag{7.3}$$

The functional determinant can be computed by using the identity $\ln(\det A) = \mathrm{tr}(\ln A)$. Taking the logarithm on both sides of (7.3) gives

$$i\Gamma[A_\mu]+i\int d^4x\frac{1}{4}F_{\mu\nu}F^{\mu\nu}-\ln\mathcal{N} = \mathrm{tr}\bigl[\ln\bigl(i\not{D}-m\bigr)\bigr].$$

The trace is independent of the chosen basis which allows us to compute it in position space

$$\mathrm{tr}\bigl[\ln\bigl(i\not{D}-m\bigr)\bigr] = \int d^4x\,\mathrm{Tr}\bigl[\,\langle x|\ln\bigl(i\not{D}-m\bigr)|x\rangle\bigr]$$

where Tr denotes the trace over the spinor indices. With this expression for the effective action we can write down an expression for the effective Lagrangian ($\Gamma = \int d^4x\mathcal{L}_{\text{eff}}(x)$):

$$\mathcal{L}_{\text{eff}} = -\frac{1}{4}F_{\mu\nu}F^{\mu\nu} - i\,\mathrm{Tr}\bigl[\,\langle x|\ln\bigl(i\not{D}-m\bigr)|x\rangle\bigr]. \tag{7.4}$$

We want to compute $\mathrm{Tr}\bigl[\,\langle x|\ln\bigl(i\not{D}-m\bigr)|x\rangle\bigr]$. To do this we will first introduce Schwinger's proper-time formalism. The expression $\hat{G} := \frac{i}{i\not{D}-m}$ can be understood as the formal solution of

$$(i\not{D}-m)\hat{G} = 1.$$

Here 1 denotes the identity operator, which makes $\langle x|\,\hat{G}\,|y\rangle$ the propagator of a Dirac particle. Using

$$\frac{i}{A+i\epsilon} = \int_0^\infty ds e^{is(A+i\epsilon)}$$

we obtain

$$\begin{aligned}\langle x|\,\hat{G}\,|y\rangle &= \langle x|\,\frac{i}{i\not{D}-m}\,|y\rangle \\ &= \langle x|\,(i\not{D}+m)i\int_0^\infty ds e^{-is(m^2+\not{D}^2)}\,|x\rangle\end{aligned}$$

where we introduced the proper time s. Convergence of this integral is ensured because of the $-i\epsilon$ term in m. With this we can finally derive an expression for the effective Lagrangian.

For this we take the derivative of $\mathcal{L}_{\text{eff}}$,

$$\begin{aligned}\frac{d}{dm^2}\mathcal{L}_{\text{eff}}(x) &= \frac{i}{2m}\,\text{Tr}\Big[\,\langle x|\frac{1}{i\not{D}-m}|x\rangle\Big] \\ &= -\frac{1}{2}\int_0^\infty ds e^{-ism^2}\,\text{Tr}\Big[\,\langle x|e^{-is\not{D}^2}|x\rangle\Big],\end{aligned}$$

where we used the fact that the trace of an odd number of gamma matrices is zero. Integrating by m^2 gives

$$\mathcal{L}_{\text{eff}} = -\frac{1}{4}F_{\mu\nu}F^{\mu\nu} + \frac{i}{2}\int_0^\infty \frac{ds}{s}e^{-ism^2}\,\text{Tr}\Big[\,\langle x|e^{-is\not{D}^2}|x\rangle\Big] + \text{const.} \tag{7.5}$$

The result for scalar QED differs in that instead of $\not{D} = (\hat{p}-eA(\hat{x}))^2 - \frac{e}{2}F_{\mu\nu}\sigma^{\mu\nu}$ we have $(\hat{p}-eA(\hat{x}))^2$.

We can now use the path integral formulation of ordinary quantum mechanics. To do this we interpret

$$\hat{H} = -(\hat{p}-eA(\hat{x}))^2 - \frac{e}{2}F_{\mu\nu}\sigma^{\mu\nu}$$

as a Hamilton operator of a fermion in an electromagnetic field. Then $\langle x|\,e^{-is\hat{H}}\,|y\rangle$ can be understood as the propagator of a fermion particle which has the path integral representation

$$\langle x|\,e^{-is\hat{H}}\,|y\rangle = \int_{z(0)=x}^{z(s)=y}\mathcal{D}z(\tau)\,\exp\Big(i\int_0^s d\tau\,\mathcal{L}(z,\dot{z})\Big) \tag{7.6}$$

where $\mathcal{L} = \hat{p}\dot{\hat{x}} - \hat{H}$ denotes the Legendre transform of the Hamiltonian $\hat{H}$. For the case of spinor QED we find

$$\mathcal{L} = -\frac{1}{4}(\frac{d\hat{z}^\mu}{ds})^2 - eA^\mu\frac{d\hat{x}^\mu}{ds} + \frac{e}{2}\sigma^{\mu\nu}F_{\mu\nu}$$

with $\sigma^{\mu\nu} = \frac{i}{2}[\gamma^\mu, \gamma^\nu]$ (The result for scalar QED consists of only the first two terms). Inserting this in (7.6) we obtain for the propagator of a closed loop

$$\begin{aligned}\langle x|\, e^{-is\hat{H}}\, |x\rangle &= \int_{z(0)=x}^{z(s)=x} \mathcal{D}z(\tau)\, \exp\left(-i \int d\tau\, \frac{1}{4}\left(\frac{d\hat{z}^\mu}{ds}\right)^2 + eA^\mu \frac{d\hat{x}^\mu}{ds} - \frac{e}{2}\sigma^{\mu\nu}F_{\mu\nu}\right) \\ &= \int_{z(0)=x}^{z(s)=x} \mathcal{D}z(\tau)\, \exp\left(-i \int d\tau\, \frac{1}{4}\left(\frac{d\hat{z}^\mu}{ds}\right)^2 + eA^\mu \frac{d\hat{x}^\mu}{ds}\right)\sigma[z(\tau), A]\end{aligned} \tag{7.7}$$

with $\sigma[x(\tau), A] = \mathrm{Tr}\,\mathcal{P}\exp\left(i\frac{e}{2}[\gamma^\mu, \gamma^\nu]\int_0^s d\tau F_{\mu\nu}(z(\tau))\right)$ where Tr denotes the Dirac trace and $\mathcal{P}$ the path ordering symbol.

Now for the case of scalar QED one obtains the same expression just without the spin part. It is therefore clear that the reason for the quadratic growth for strong magnetic fields is the term $\sigma[x(\tau), A]$. Writing $F_{\mu\nu} = f_{\mu\nu} + F^{\mathrm{BG}}_{\mu\nu}$ with the constant background field $F^{\mathrm{BG}}_{\mu\nu}$ and the photon field $f_{\mu\nu}$ we find that $\sigma[x(\tau), A]$ contains contributions from the interaction of the spin magnetic moment with the background field and with the scattered photons. We are now going to ignore the latter to investigate how far the strong field behavior can be understood as a consequence of the background field alone.

Doing this we can evaluate the expression explicitly

$$\begin{aligned}\sigma_{\mathrm{BG}}[z(\tau), A_{\mathrm{BG}}] &= \mathrm{Tr}\,\mathcal{P}\exp\left(i\frac{e}{2}[\gamma^\mu, \gamma^\nu]\int_0^s d\tau F^{\mathrm{BG}}_{\mu\nu}(z(\tau))\right) \qquad (7.8)\\ &= \mathrm{Tr}\,\exp\left(-\int_0^s eB_{\mathrm{BG}} \begin{pmatrix}\sigma_3 & 0\\ 0 & \sigma_3\end{pmatrix}\right) \\ &= \mathrm{Tr}\exp\left(-esB_{\mathrm{BG}} \begin{pmatrix}\sigma_3 & 0\\ 0 & \sigma_3\end{pmatrix}\right) \\ &= 4\cosh(esB_{\mathrm{BG}}). \qquad (7.9)\end{aligned}$$

Notice that the result is independent of $z(\tau)$ which means we can pull it out of the path integral. The full result of (7.7) is therefore the product of (7.9) and the result of the path integral (7.7) for scalar QED (for a full derivation see [7]). Inserting this in our Lagrangian (7.5) and renormalizing the expression we obtain

$$\begin{aligned}\mathcal{L} = -\frac{1}{4}F_{\mu\nu}F^{\mu\nu} - \frac{1}{8\pi^2}\int_0^\infty \frac{ds}{s^3} e^{-m^2 s}((es)^2 ab \frac{\cosh(esB_{\mathrm{BG}})}{\sinh(esa)\sin(esb)} - 1 \\ - \frac{1}{6}(es)^2(b^2 - a^2 + 3B^2_{\mathrm{BG}}e^2)).\end{aligned} \tag{7.10}$$

And the differential cross section computed with this Lagrangian shows indeed the quadratic growth in cases where it is expected. Furthermore it reproduces the

same angular angular distribution for the differential cross section for strong magnetic fields as we saw in the chapter about spinor QED. However we find that the coefficient of the growth of matrix elements and differential cross section does not match the result of the full Lagrangian. We think this is an artifact of the neglected interaction between in- and outgoing photons and the spin of the fermion content.

And indeed, if one adds the $\cos(esb)$ term to the Lagrangian, which represents the interaction of the electric fields of the photons with the spin of the fermions to obtain the renormalized Lagrangian

$$\begin{aligned}\mathcal{L} = -\frac{1}{4}F_{\mu\nu}F^{\mu\nu} - \frac{1}{8\pi^2}\int_0^\infty \frac{ds}{s^3}e^{-m^2 s}((es)^2 ab\frac{\cosh(esB_{\mathrm{BG}})\cot(esb)}{\sinh(esa)} - 1 \\ - \frac{1}{6}(es)^2(2b^2 - a^2 + 3B_{\mathrm{BG}}^2 e^2)),\end{aligned} \tag{7.11}$$

then one finds that a better match between the gradient of the matrix elements. We also found that the effects of polarizations on the scattering amplitudes are different in this approximation. For example in the case of a magnetic field $\mathbf{B} = \hat{z}$ we find for the matrix element $\mathcal{M}_{oooo}$ the expected linear growth however for $\mathcal{M}_{iiii}$ the $\frac{1}{\xi}$ decay is not there. We found however that changing from (7.11) to the renormalized Lagrangian

$$\begin{aligned}\mathcal{L} = -\frac{1}{4}F_{\mu\nu}F^{\mu\nu} - \frac{1}{8\pi^2}\int_0^\infty \frac{ds}{s^3}e^{-m^2 s}((es)^2 ab\coth(esB_{\mathrm{BG}})\cot(esb) \\ - \left(\frac{a}{B}\frac{ab^2e^2}{3B}s^2 + \frac{aBe^2}{3}s^2\right),\end{aligned} \tag{7.12}$$

where we replaced $\sinh(esa)$ with $\sinh(esB)$, leads to almost the same results as for the full Euler-Heisenberg Lagrangian.

The discussion above shows that the interaction of the spin magnetic moment with the constant magnetic background field alone is not sufficient to explain the full behavior for strong magnetic fields in spinor QED. And in fact one can show that the behavior only holds in this way for fermions with a gyromagnetic ratio $g = 2$. We implicitly assumed this when we used the Euler-Heisenberg Lagrangian. This can be seen in the derivation of the Euler-Heisenberg Lagrangian presented in [9], in chapter 33.1 where fermions with $g = 2$ are discussed. For a fermion with $g \neq 2$ the derivation remains almost the same with the only difference being that the spin magnetic moment energy carries an extra factor of $g/2$. One can then see that only for $g = 2$ does the spin magnetic moment energy cancel exactly with the energy of the lowest Landau level. If one derives the Euler-Heisenberg Lagrangian for a general g, not necessarily equal to 2, one finds that the effective Lagrangian is then given by (1.12) with the numerator replaced with $\cosh(esag/2)\cos(esbg/2)$ and as we saw in

(7.10 - 7.12) the behavior of the theory depends very sensitively on the fact that the numerator and the denominator cancel each other in the limit of strong fields.

We find that only for $g = 2$ does the numerator compensate the exponential decay of the $\sinh(esa)$ in the denominator and we can find the quadratic growth described here. For $g < 2$ the quadratic growth of the cross section disappears and we have a situation similar to the case of scalar QED where the integrand decreases exponentially with the field strength. For $g > 2$ the derivation in [9] breaks down because the integrand diverges for every finite b and one cannot perform the rotation to imaginary proper time s. Because the asymptotic behavior of a quadratic growth depends on g being exactly 2 the effect only remains as long as we ignore the anomalous magnetic moment. Therefore we expect that eventually the corrections to the anomalous spin-magnetic moment will have a non-negligible effect on the strong field behavior.

For more information on this matter and also a discussion on the implications of these computations for heavy ion collisions at the LHC see [23], especially the discussion at the end and appendix B.3.

Bibliography

[1] H. Euler and B. Kockel, "Über die Streuung von Licht an Licht nach der Diracschen Theorie," *Naturwiss.* **23** (1935) 246.

[2] W. Heisenberg and H. Euler, "Consequences of Dirac's theory of positrons," *Z. Phys.* **98** (1936) 714–732, arXiv:physics/0605038 [physics].

[3] G. V. Dunne, "The Heisenberg-Euler Effective Action: 75 years on," *Int. J. Mod. Phys.* **A27** (2012) 1260004, arXiv:1202.1557 [hep-th]. [Int. J. Mod. Phys. Conf. Ser.14,42(2012)].

[4] V. Fock, "Proper time in classical and quantum mechanics," *Phys. Z. Sowjetunion* **12** (1937) 404–425.

[5] E. C. G. Stueckelberg, "La Mecanique du point materiel en theorie de relativite et en theorie des quanta," *Helv. Phys. Acta* **15** (1942) 23–37.

[6] R. P. Feynman, "Mathematical formulation of the quantum theory of electromagnetic interaction," *Phys. Rev.* **80** (1950) 440–457.

[7] C. Schubert, "Lectures on the worldline formalism," *School of spinning particles in quantum field theory: worldline formalism, higher spins and conformal geometry* (2012) .

[8] W. Dittrich and H. Gies, "Probing the quantum vacuum. Perturbative effective action approach in quantum electrodynamics and its application," *Springer Tracts Mod. Phys.* **166** (2000) 1–241.

[9] M. D. Schwartz, *Quantum Field Theory and the Standard Model*. Cambridge University Press, 2014. http://www.cambridge.org/us/academic/subjects/physics/theoretical-physics-and-mathematical-physics/quantum-field-theory-and-standard-model.

[10] R. R. Wilson, "Scattering of 1.33 Mev Gamma-Rays by an Electric Field," *Phys. Rev.* **90** (1953) 720–721.

[11] **ATLAS** Collaboration, M. Aaboud *et al.*, "Evidence for light-by-light scattering in heavy-ion collisions with the ATLAS detector at the LHC," *Nature Phys.* **13** no. 9, (2017) 852–858, arXiv:1702.01625 [hep-ex].

[12] K. Itakura, "Strong-field physics as a new probe of early-time dynamics in heavy-ion collisions," *J. Phys. Conf. Ser.* **422** (2013) 012029.

[13] D. E. Kharzeev, L. D. McLerran, and H. J. Warringa, "The Effects of topological charge change in heavy ion collisions: 'Event by event P and CP violation'," *Nucl. Phys.* **A803** (2008) 227–253, arXiv:0711.0950 [hep-ph].

[14] V. S. Vanyashin and M. V. Terentev, "The Vacuum Polarization of a Charged Vector Field," *Zh. Eksp. Teor. Fiz.* **48** no. 2, (1965) 565–573. [Sov. Phys. JETP21, no.2, 375 (1965)].

[15] M. Srednicki, *Quantum field theory.* Cambridge University Press, 2007.

[16] A. Rebhan and G. Turk, "Polarization effects in light-by-light scattering: EulerHeisenberg versus BornInfeld," *Int. J. Mod. Phys.* **A32** no. 10, (2017) 1750053, arXiv:1701.07375 [hep-ph].

[17] M. N. Chernodub, "Electromagnetic superconductivity of vacuum induced by strong magnetic field," *Lect. Notes Phys.* **871** (2013) 143–180, arXiv:1208.5025 [hep-ph].

[18] R. P. Feynman, "The Theory of positrons," *Phys. Rev.* **76** (1949) 749–759.

[19] C. Schubert, "QED in the worldline representation," *AIP Conf. Proc.* **917** (2007) 178–194, arXiv:hep-th/0703186 [hep-th].

[20] R. Shaisultanov, "On the string-inspired approach to qed in external field," *Physics Letters B* **378** no. 1-4, (1996) 354–356.

[21] C. Schubert, "An Introduction to the worldline technique for quantum field theory calculations," *Acta Phys. Polon.* **B27** (1996) 3965–4001, arXiv:hep-th/9610108 [hep-th].

[22] J. S. Schwinger, "On gauge invariance and vacuum polarization," *Phys. Rev.* **82** (1951) 664–679.

[23] R. Baier, A. Rebhan, and M. Wödlinger, "Light-by-Light Scattering in the Presence of Magnetic Fields," arXiv:1804.06140 [hep-ph].

Appendices

Appendix A

Polarized differential cross sections

A.1 Introduction

We plotted the differential cross section for each matrix element. For every matrix element we prepared three graphs. The polar plot on the left shows the cross section for $\xi = 0, 0.5, 1, 1.5, 2, 2.5, 3$. The graph in the middle shows the the cross section as a function of the magnetic field for scattering angles $\eta = 0$ (blue) and $\eta = \pi/2$ (orange) scaled to the value for vanishing background field (except for the cases that are zero for vanishing background). The plot on the right shows the behavior for stronger fields, more specifically it shows the cases $\xi = 8, 8.5, 9, 9.5, 10$. The plot on the left and right hand side are scaled to the largest value present. Conclusions for the magnitudes of the cross sections can only be drawn from the graph in the middle. The matrix elements not plotted are either identical to the one shown or vanish completely. More specifically we have $\mathcal{M}_{oiio} = \mathcal{M}_{iooi}$, $\mathcal{M}_{ioio} = \mathcal{M}_{oioi}$ and all matrix elements with an odd number of i's and o's are zero. Note that this is only the case for the magnetic field configurations considered here. In general we found that for non-vanishing background field every matrix element is non-zero for some configurations. The section about vector QED is different in that the plots on the left hand side show the differential cross section for $\xi = 0, 0.1, 0.2, 0.3, 0.4, 0.5$. The plot in the middle shows the differential cross section as a function of ξ from $\xi = 0$ to $\xi = 0.9$ with a logarithmic scale. Finally the plot on the right hand side shows the differential cross section for $\xi = 0.9$ i.e. near the divergence.

A.2 Spinor QED

A.2.1 B in x direction

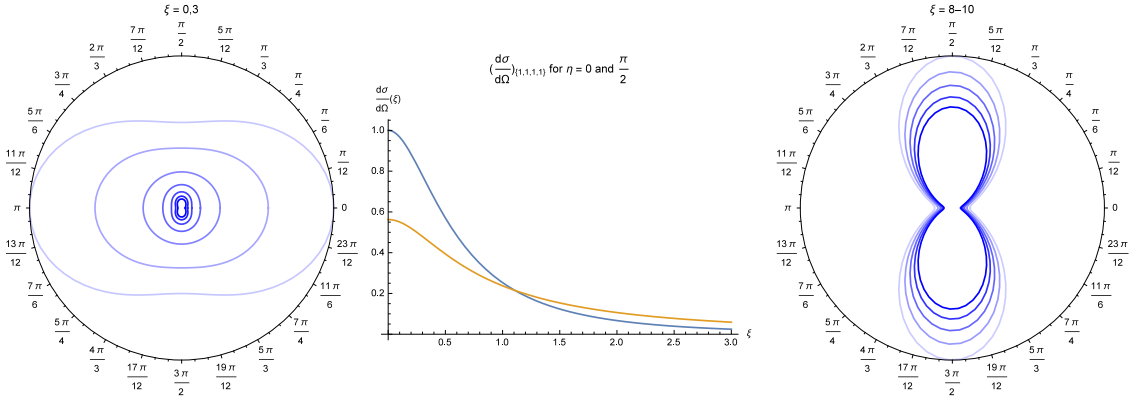

Figure A.1: Differential cross section for $\mathcal{M}_{iiii}$.

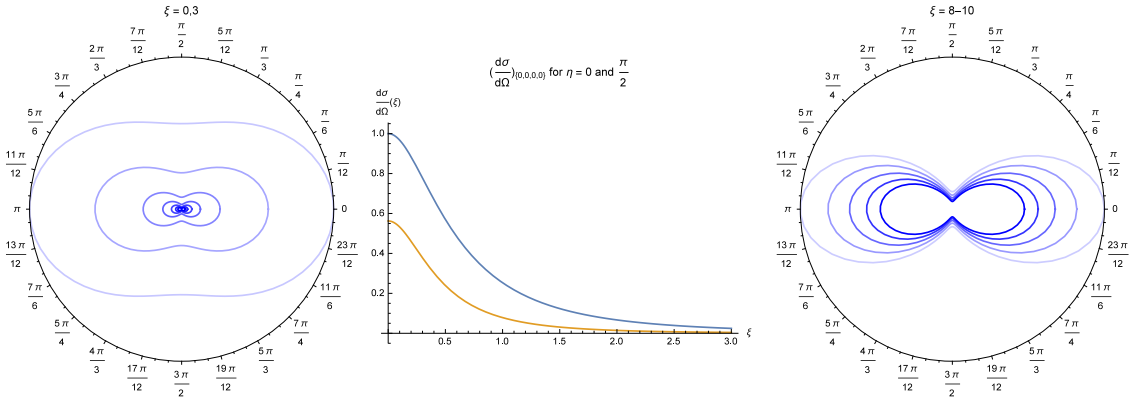

Figure A.2: Differential cross section for $\mathcal{M}_{oooo}$.

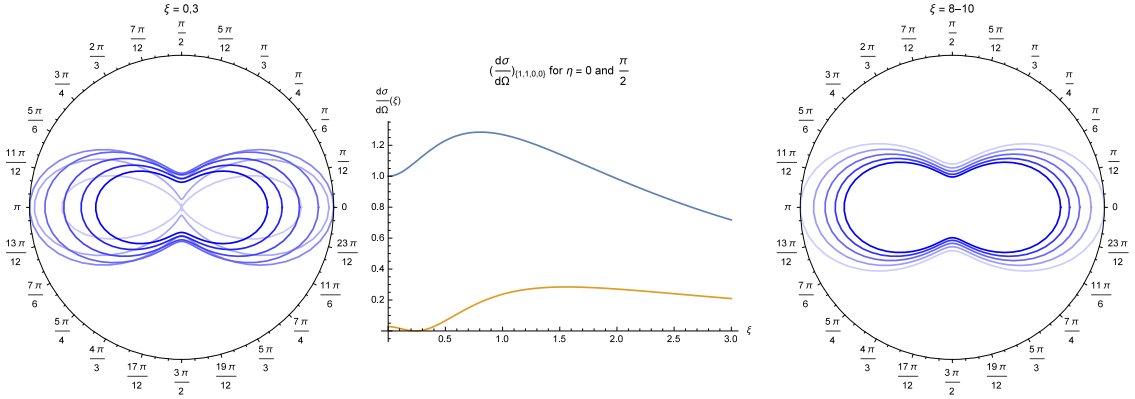

Figure A.3: Differential cross section for $\mathcal{M}_{iioo}$.

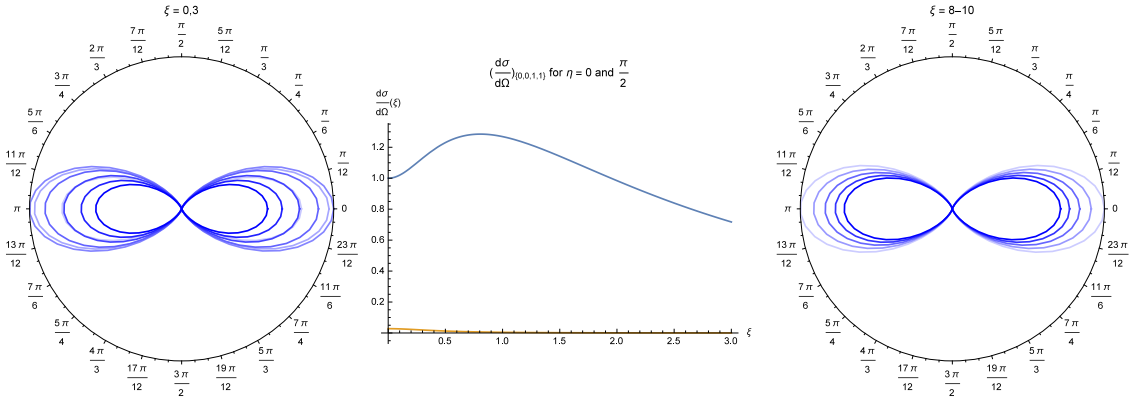

Figure A.4: Differential cross section for $\mathcal{M}_{ooii}$.

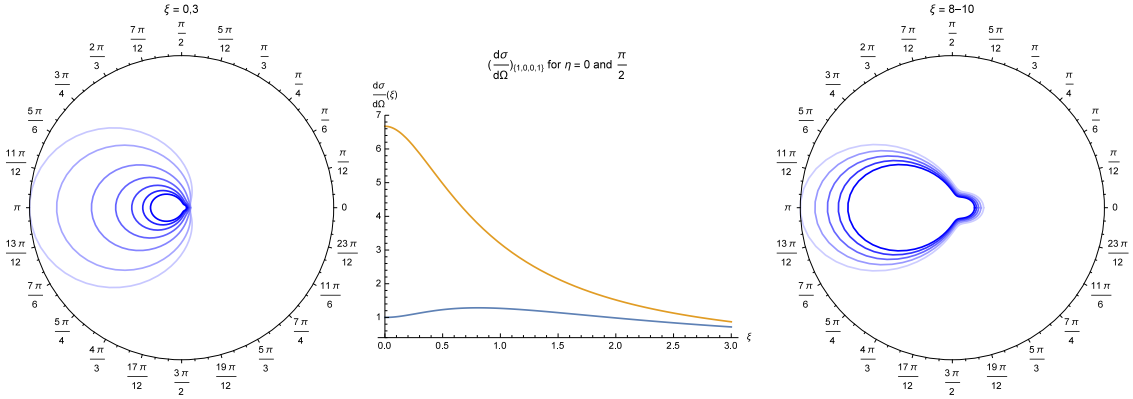

Figure A.5: Differential cross section for $\mathcal{M}_{iooi}$.

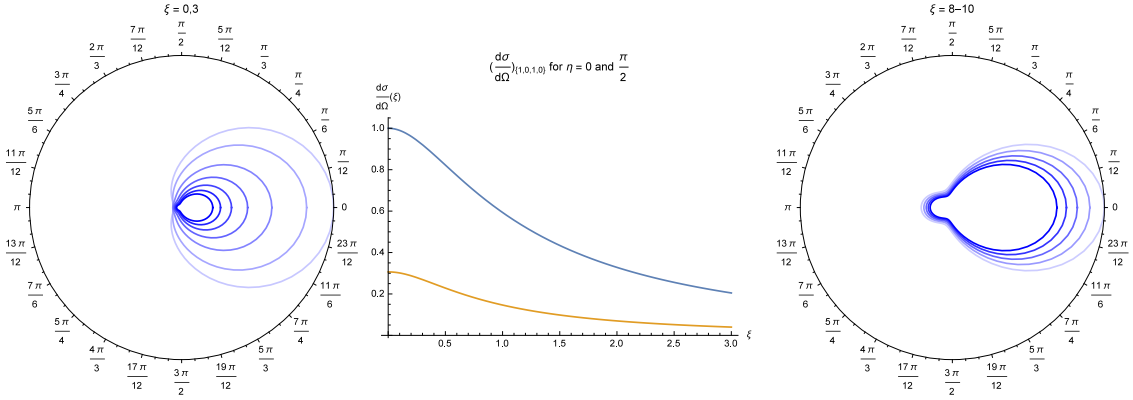

Figure A.6: Differential cross section for $\mathcal{M}_{ioio}$.

A.2.2 B in y direction

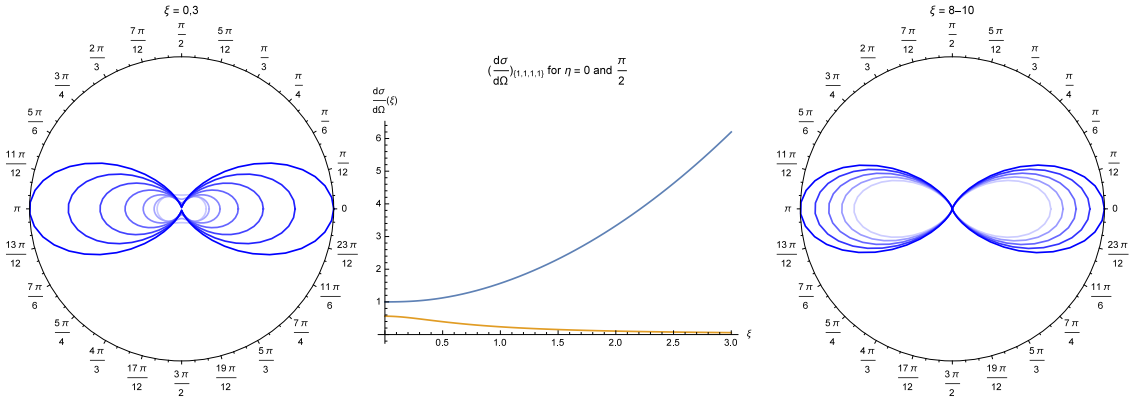

Figure A.7: Differential cross section for $\mathcal{M}_{iiii}$.

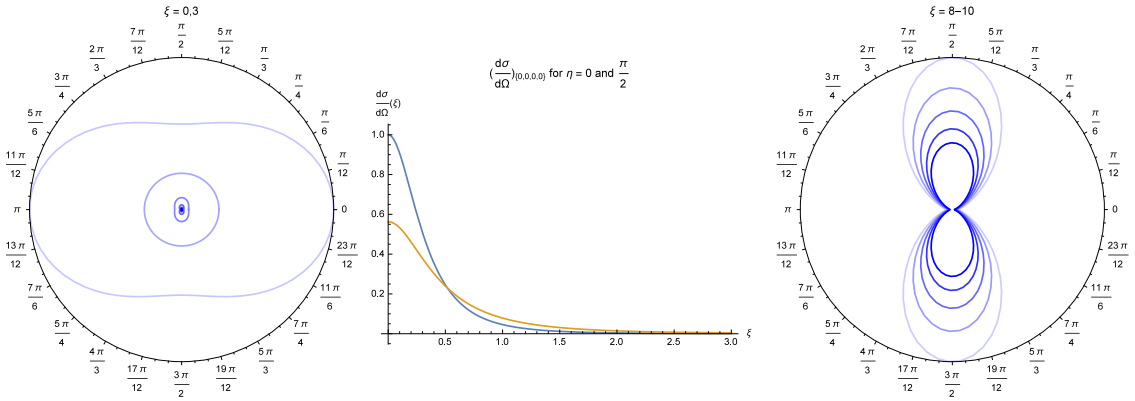

Figure A.8: Differential cross section for $\mathcal{M}_{oooo}$.

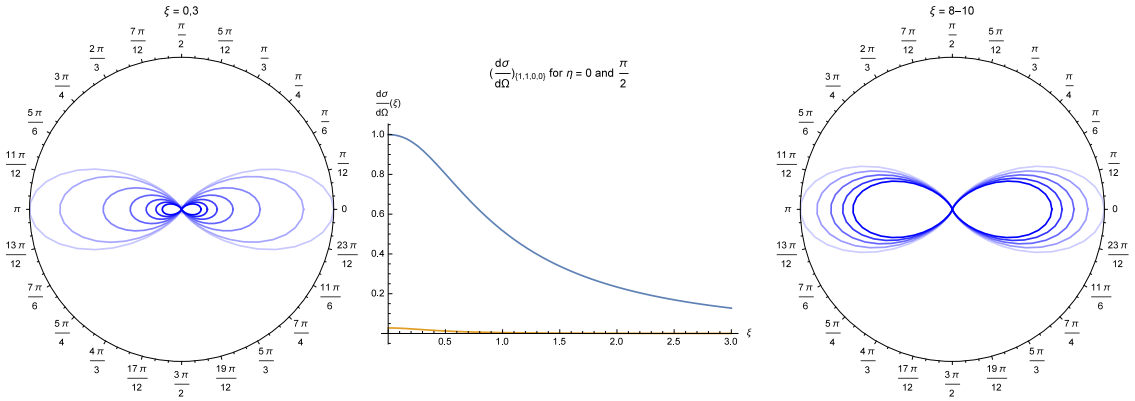

Figure A.9: Differential cross section for $\mathcal{M}_{iioo}$.

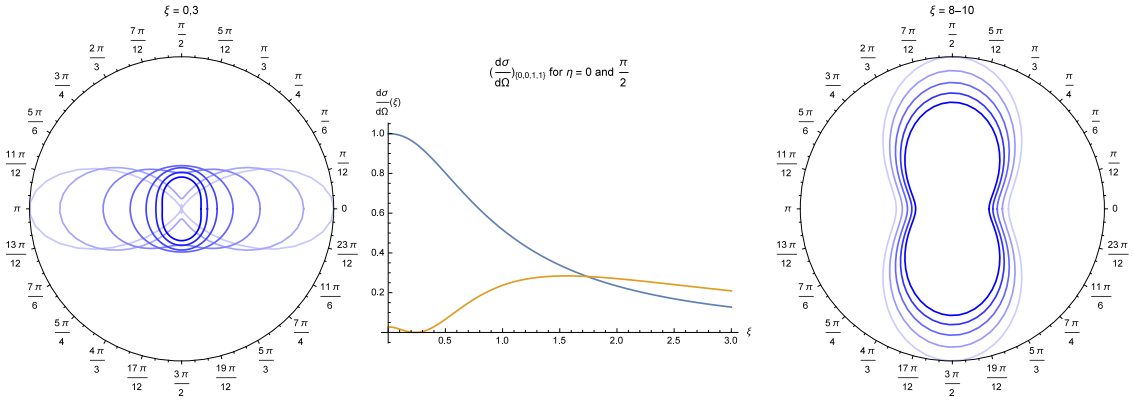

Figure A.10: Differential cross section for $\mathcal{M}_{ooii}$.

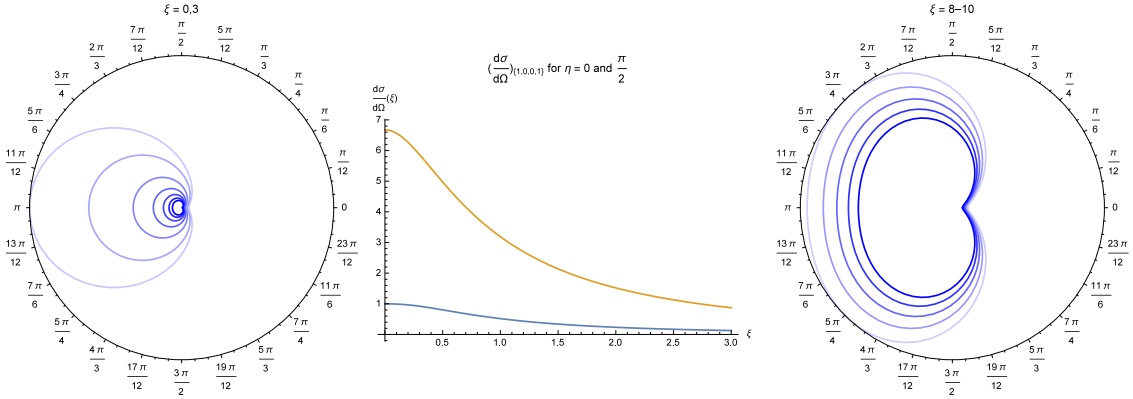

Figure A.11: Differential cross section for $\mathcal{M}_{iooi}$.

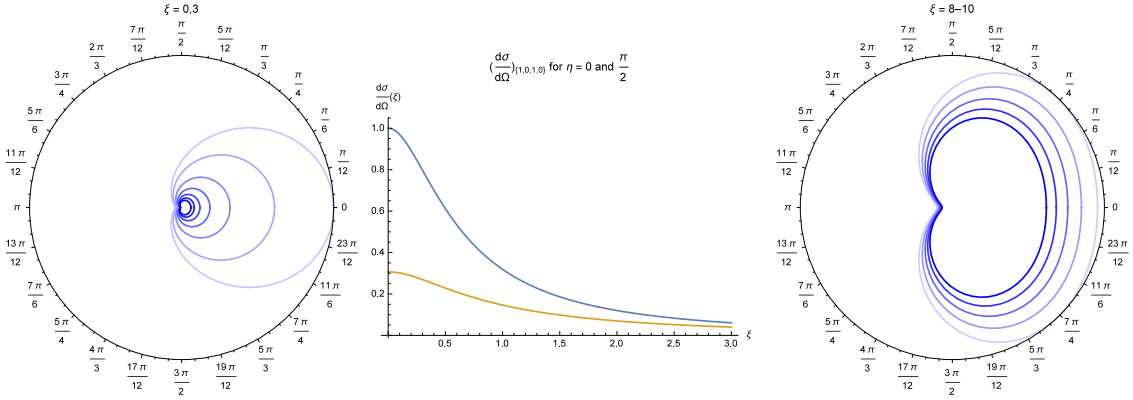

Figure A.12: Differential cross section for $\mathcal{M}_{ioio}$.

A.2.3 B in z direction

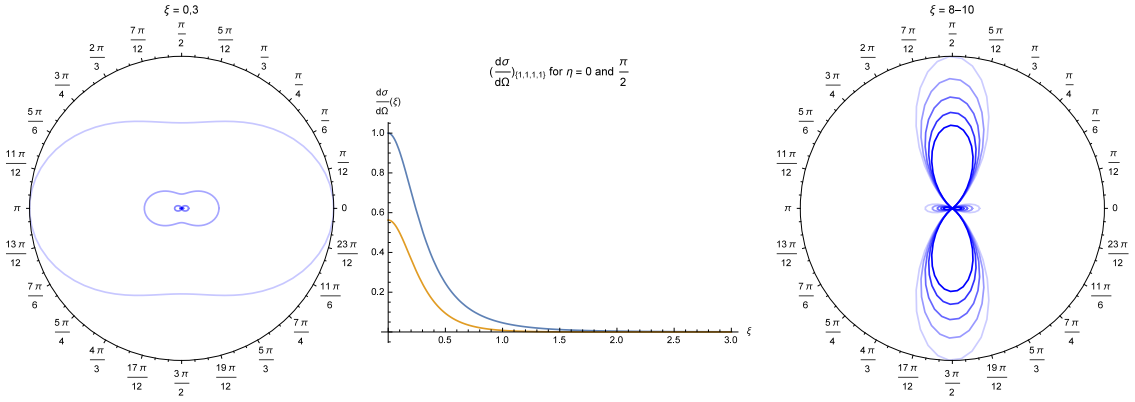

Figure A.13: Differential cross section for $\mathcal{M}_{iiii}$.

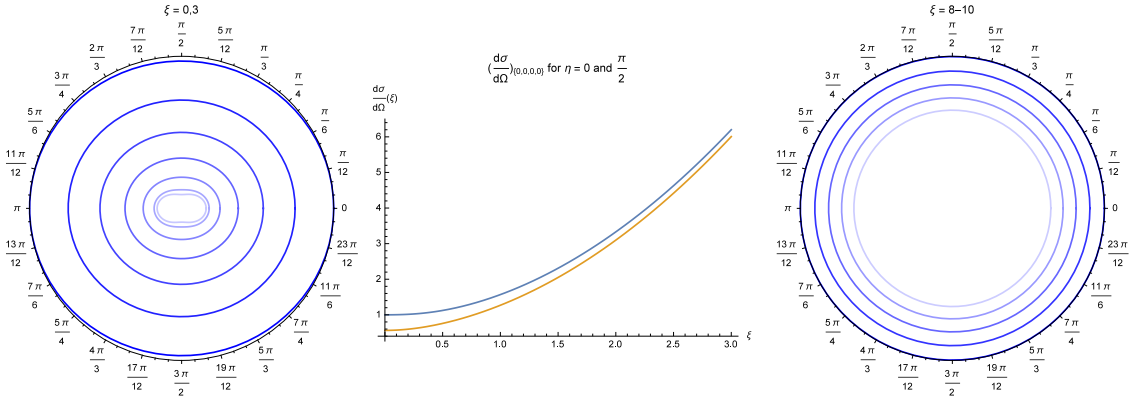

Figure A.14: Differential cross section for $\mathcal{M}_{oooo}$.

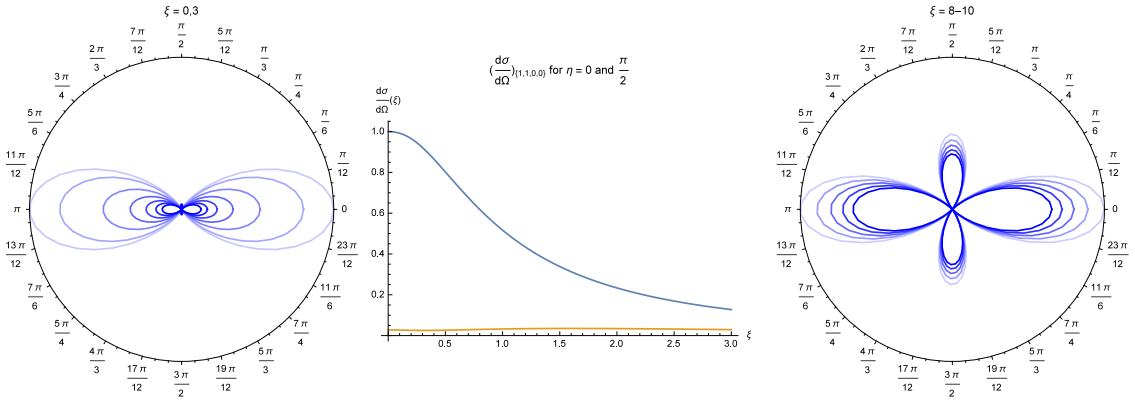

Figure A.15: Differential cross section for $\mathcal{M}_{iioo}$.

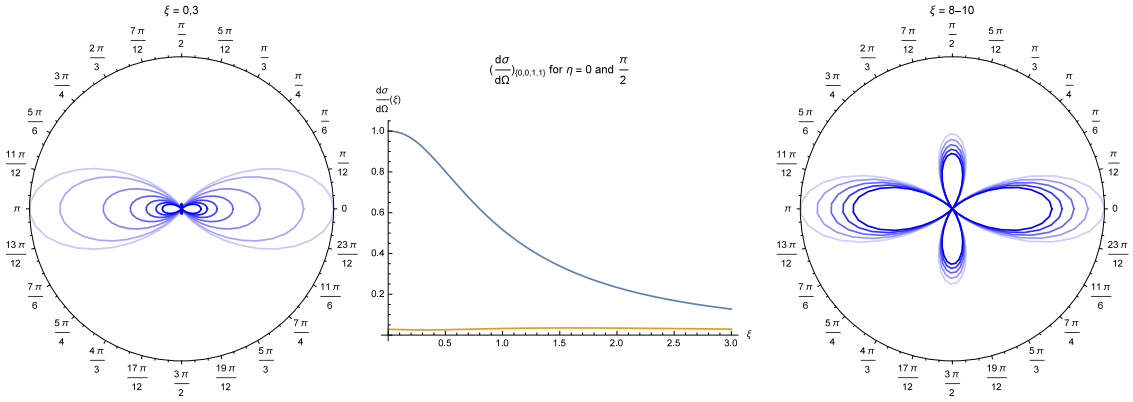

Figure A.16: Differential cross section for $\mathcal{M}_{ooii}$.

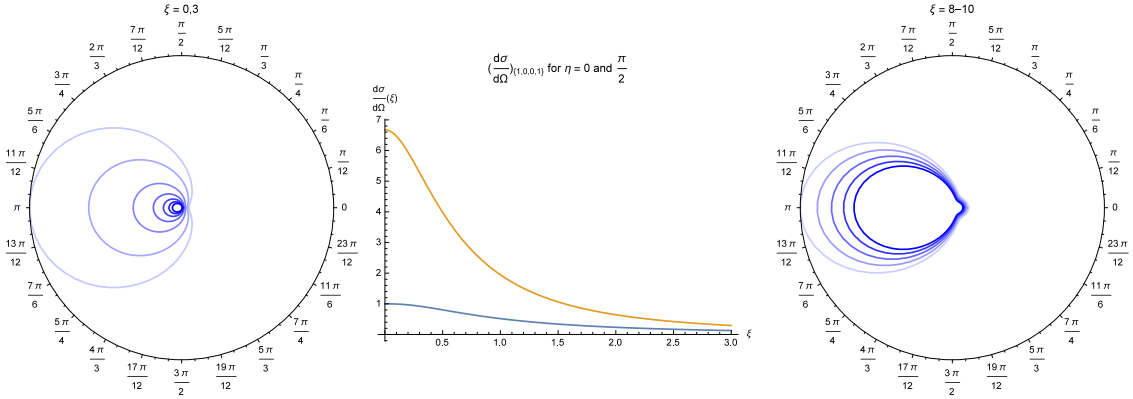

Figure A.17: Differential cross section for $\mathcal{M}_{iooi}$.

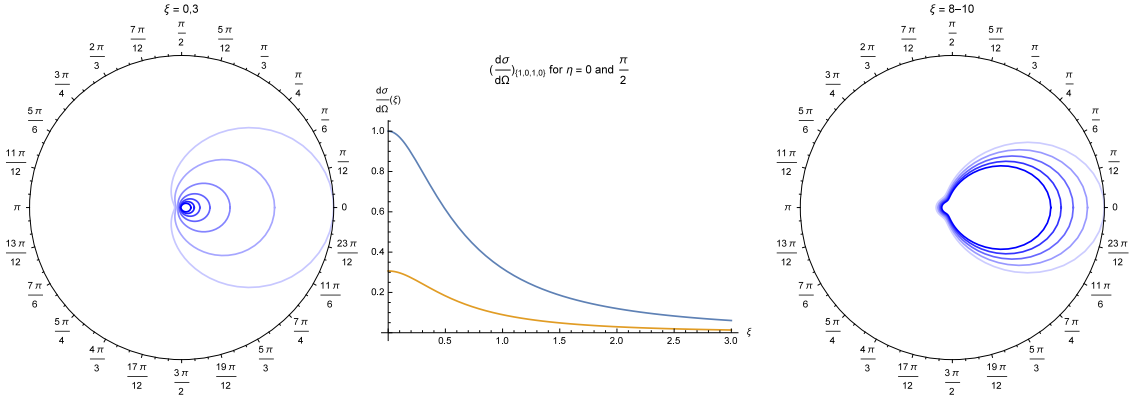

Figure A.18: Differential cross section for $\mathcal{M}_{ioio}$.

A.3 Scalar QED

A.3.1 B in x direction

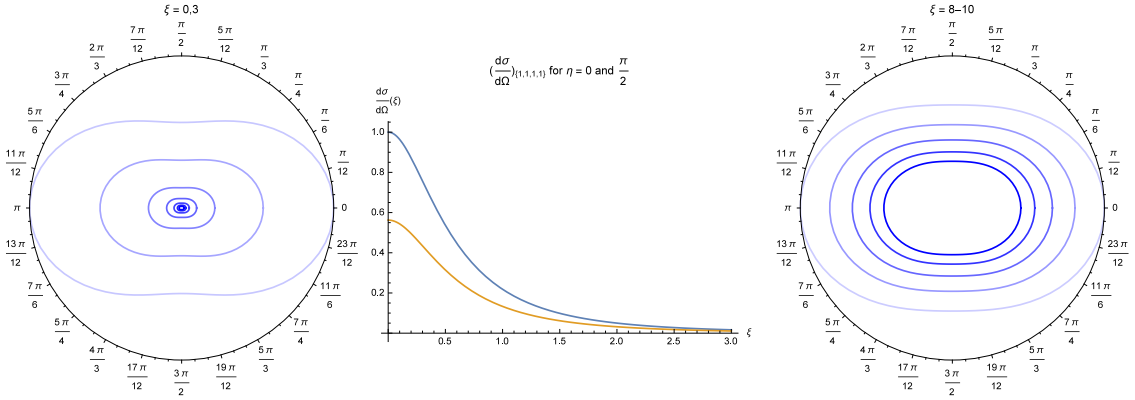

Figure A.19: Differential cross section for $\mathcal{M}_{iiii}$.

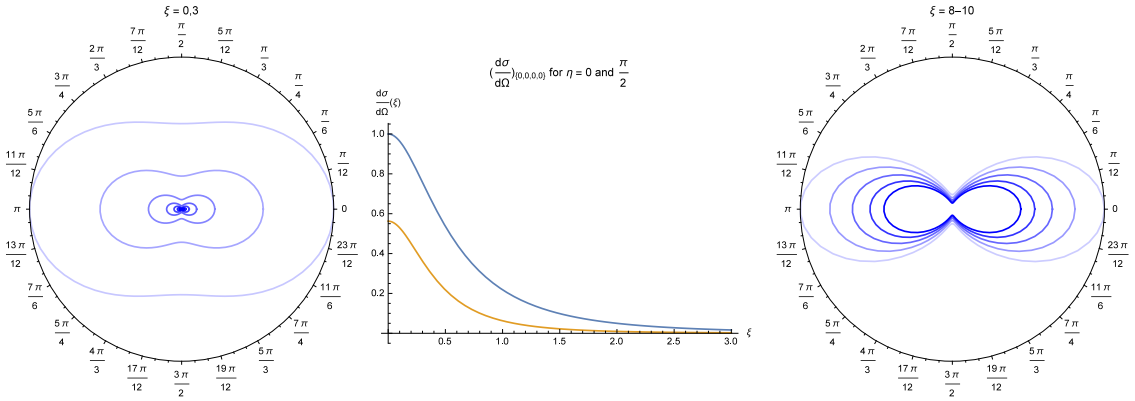

Figure A.20: Differential cross section for $\mathcal{M}_{oooo}$.

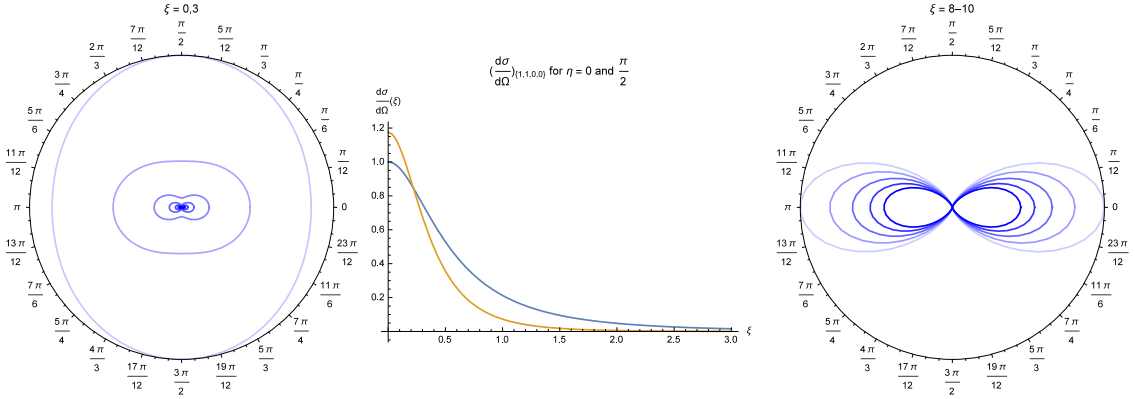

Figure A.21: Differential cross section for $\mathcal{M}_{iioo}$.

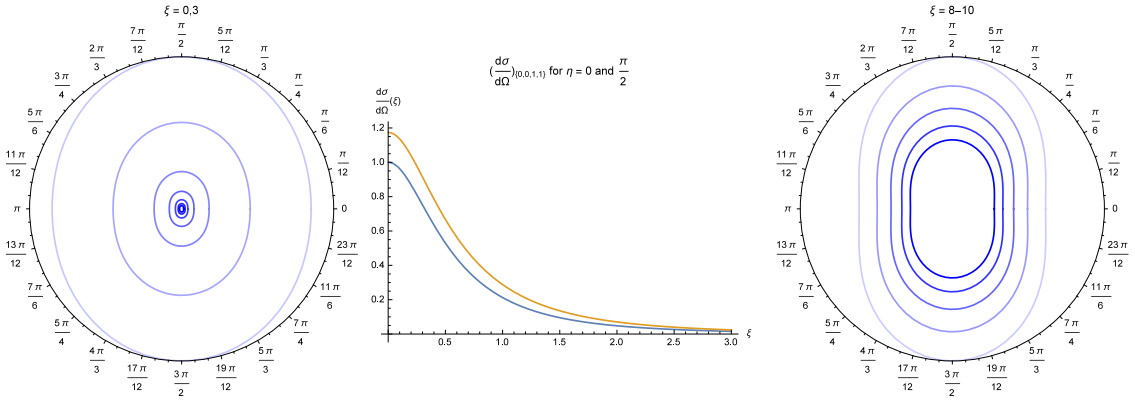

Figure A.22: Differential cross section for $\mathcal{M}_{ooii}$.

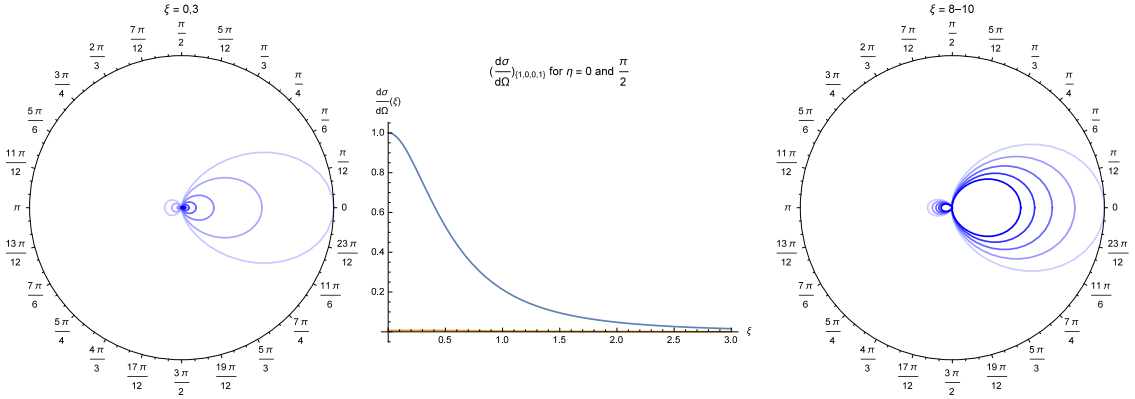

Figure A.23: Differential cross section for $\mathcal{M}_{iooi}$.

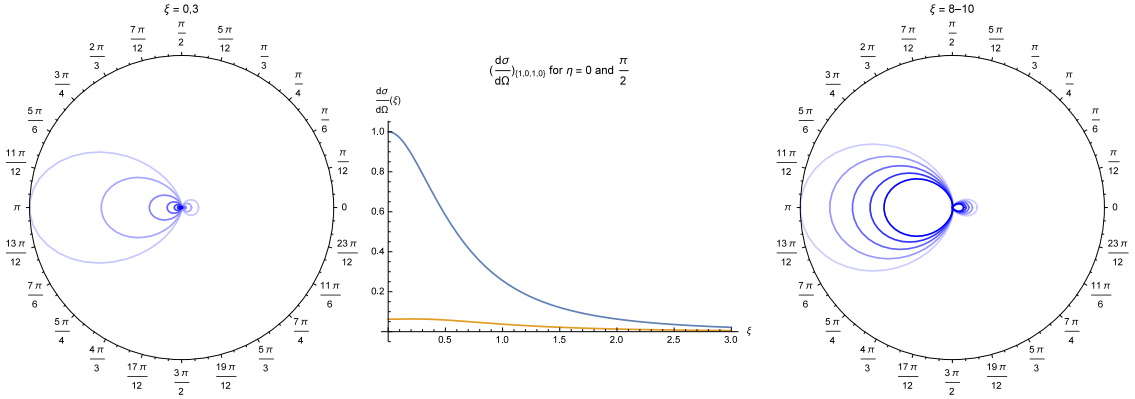

Figure A.24: Differential cross section for $\mathcal{M}_{ioio}$.

A.3.2 B in y direction

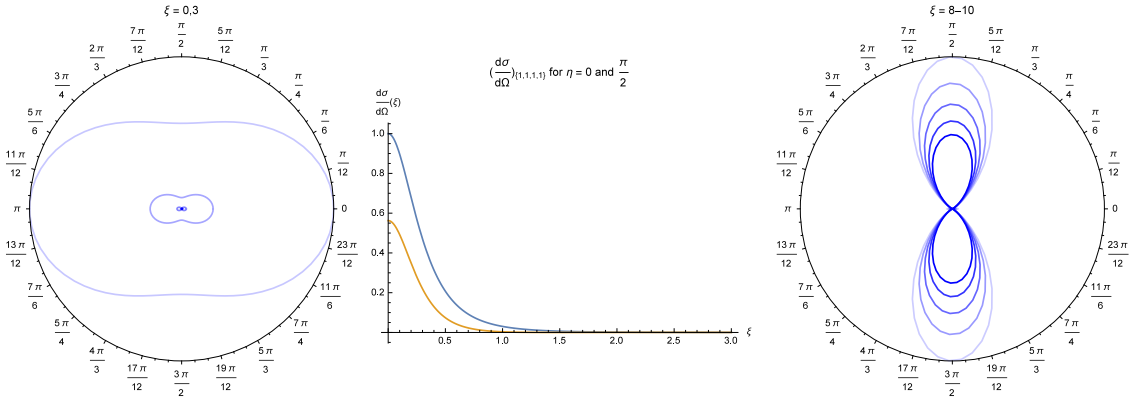

Figure A.25: Differential cross section for $\mathcal{M}_{iiii}$.

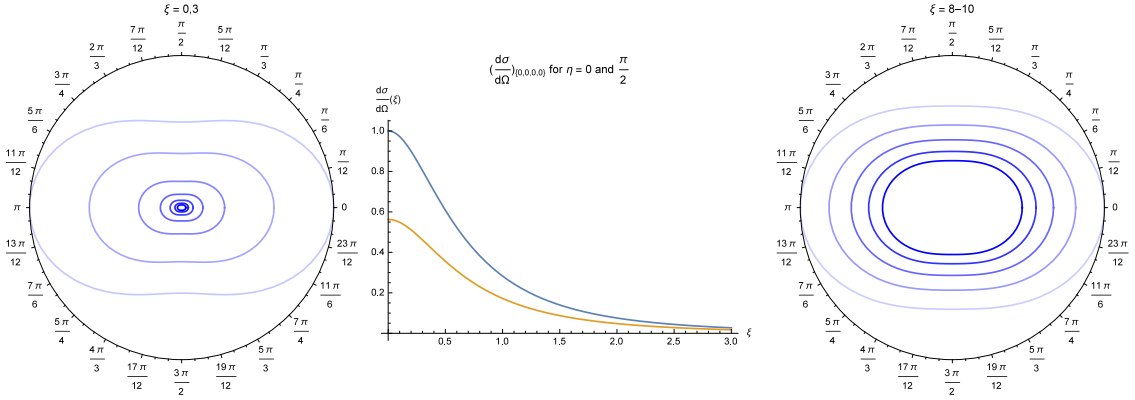

Figure A.26: Differential cross section for $\mathcal{M}_{oooo}$.

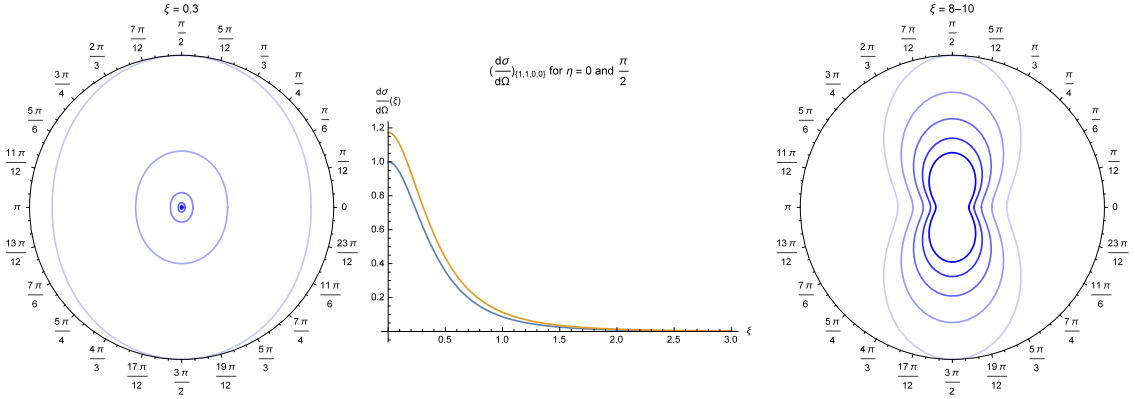

Figure A.27: Differential cross section for $\mathcal{M}_{iioo}$.

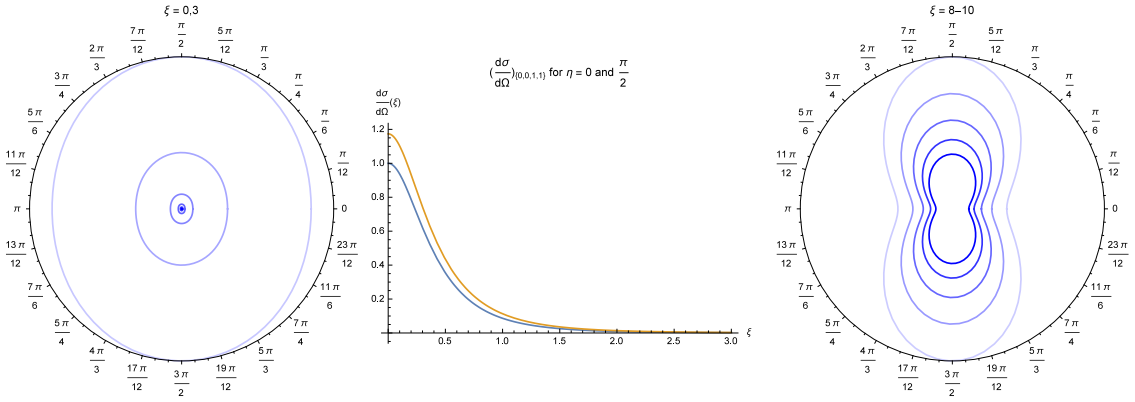

Figure A.28: Differential cross section for $\mathcal{M}_{ooii}$.

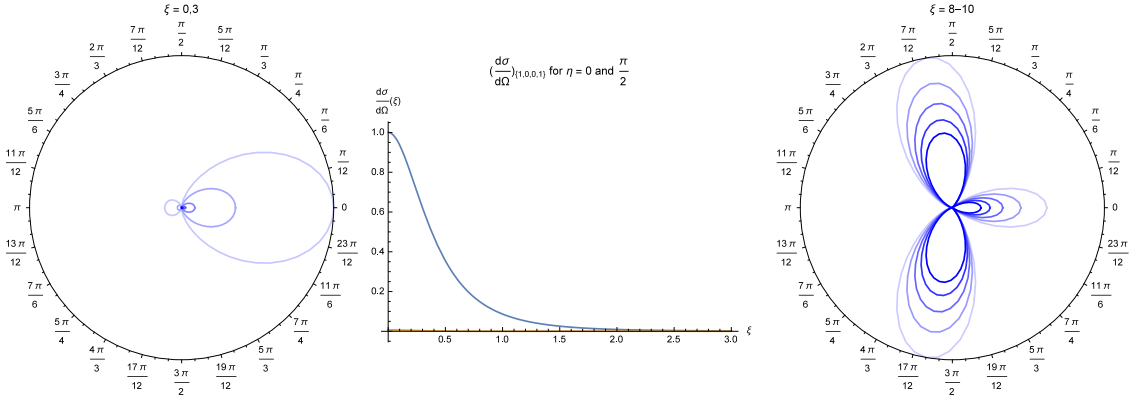

Figure A.29: Differential cross section for $\mathcal{M}_{iooi}$.

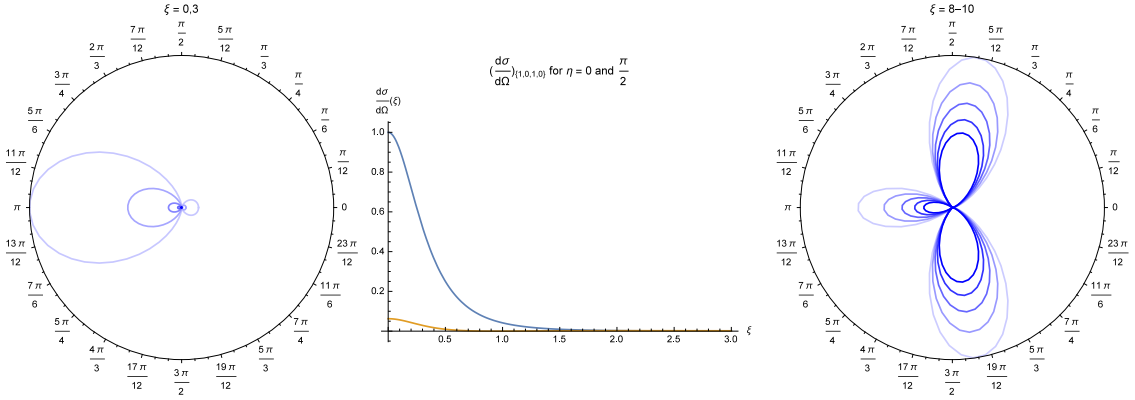

Figure A.30: Differential cross section for $\mathcal{M}_{ioio}$.

A.3.3 B in z direction

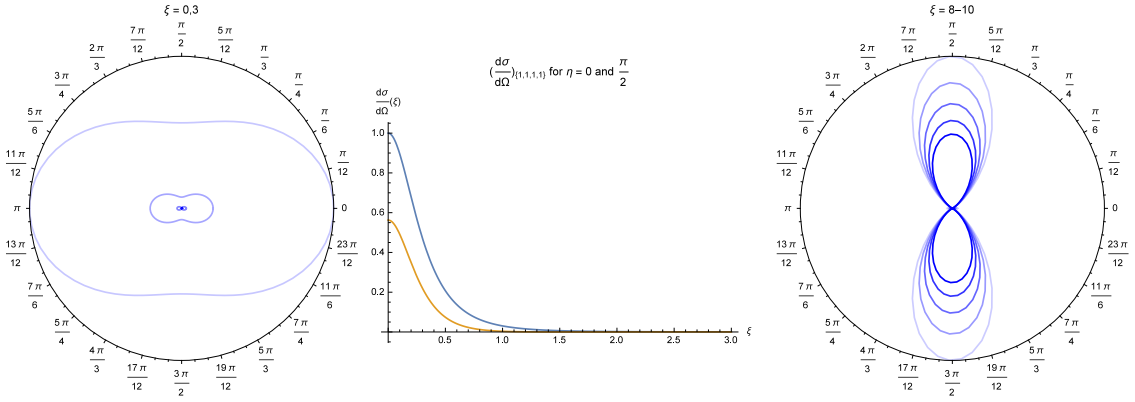

Figure A.31: Differential cross section for $\mathcal{M}_{iiii}$.

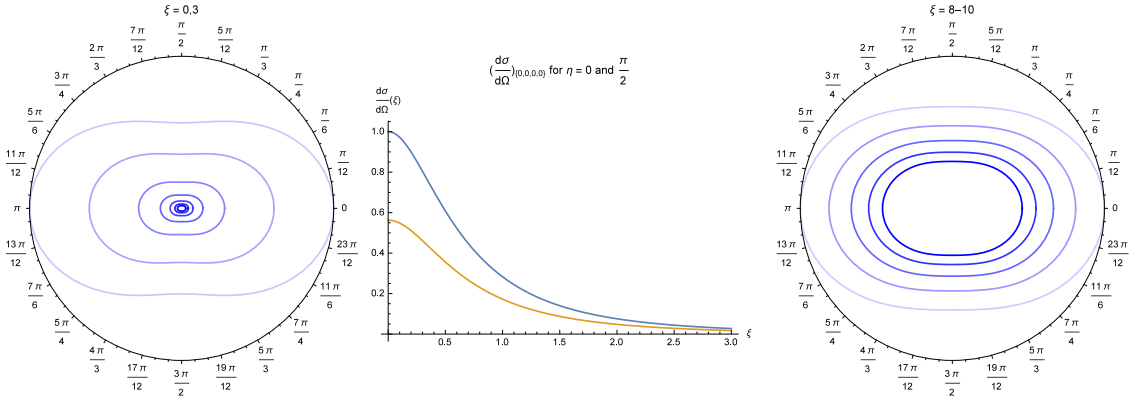

Figure A.32: Differential cross section for $\mathcal{M}_{oooo}$.

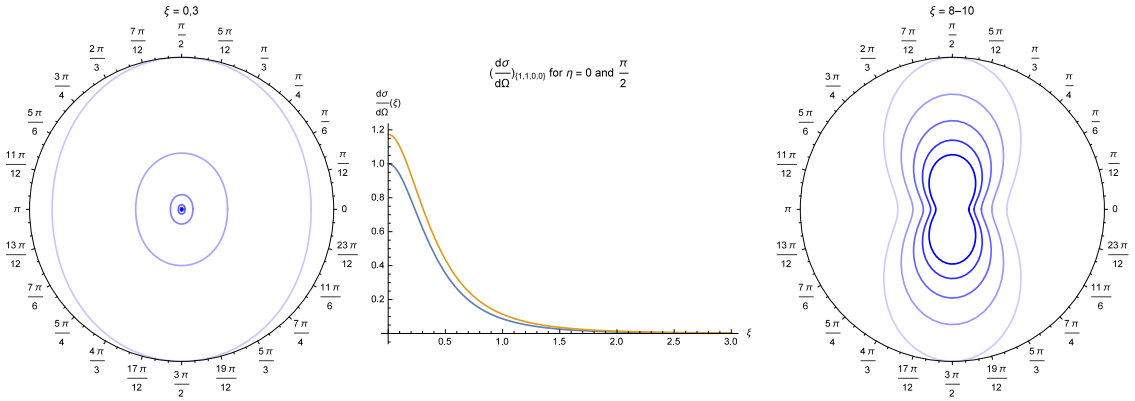

Figure A.33: Differential cross section for $\mathcal{M}_{iioo}$.

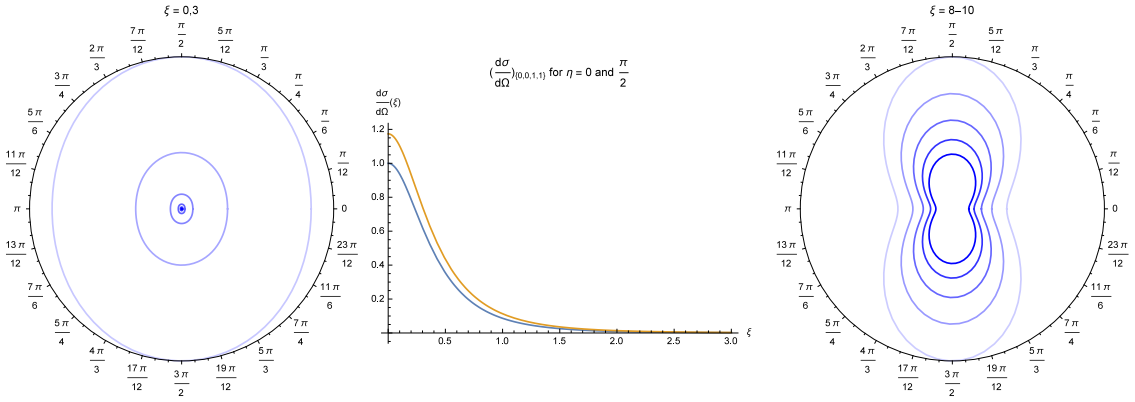

Figure A.34: Differential cross section for $\mathcal{M}_{ooii}$.

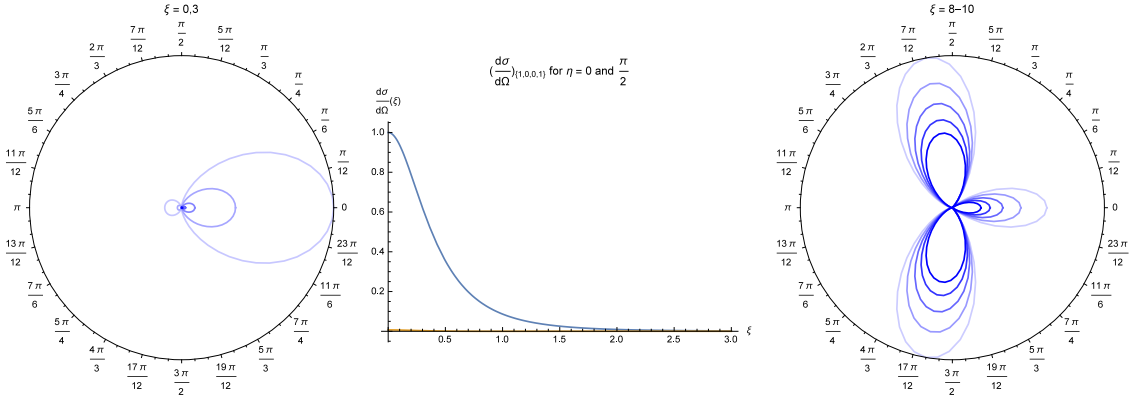

Figure A.35: Differential cross section for $\mathcal{M}_{iooi}$.

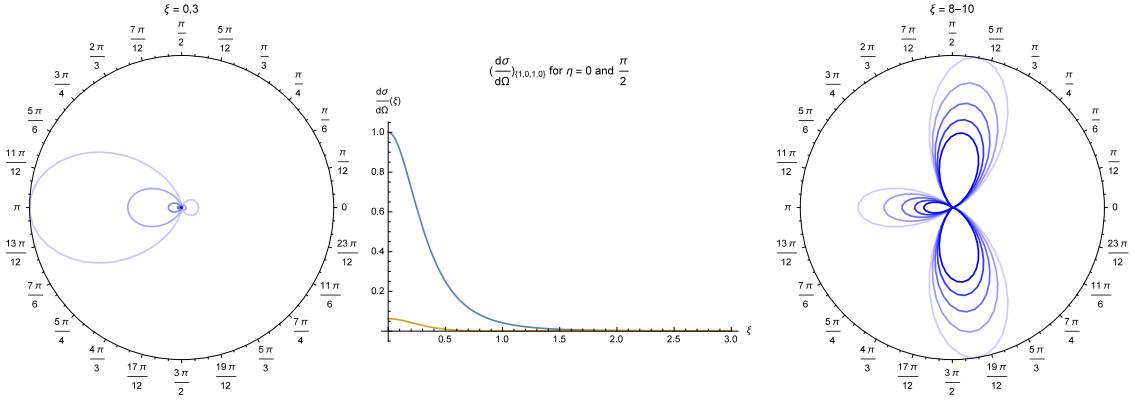

Figure A.36: Differential cross section for $\mathcal{M}_{ioio}$.

A.4 SUSY QED

A.4.1 B in x direction

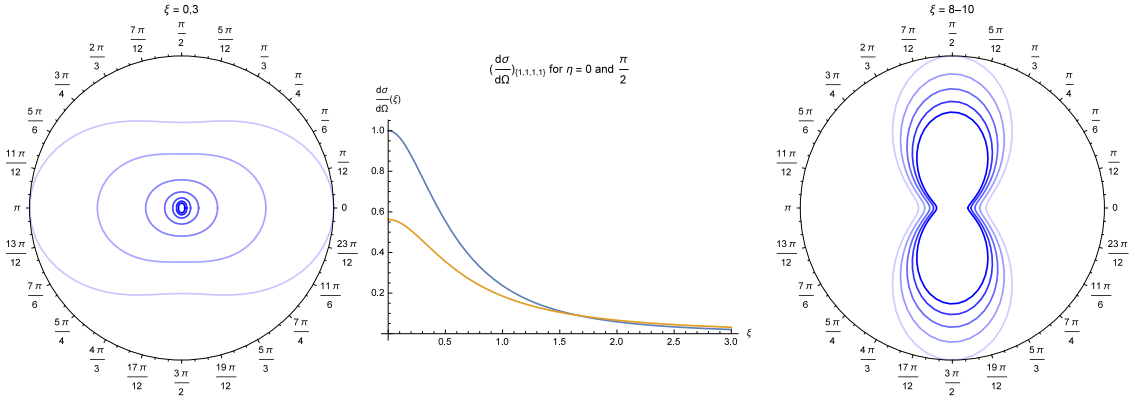

Figure A.37: Differential cross section for $\mathcal{M}_{iiii}$.

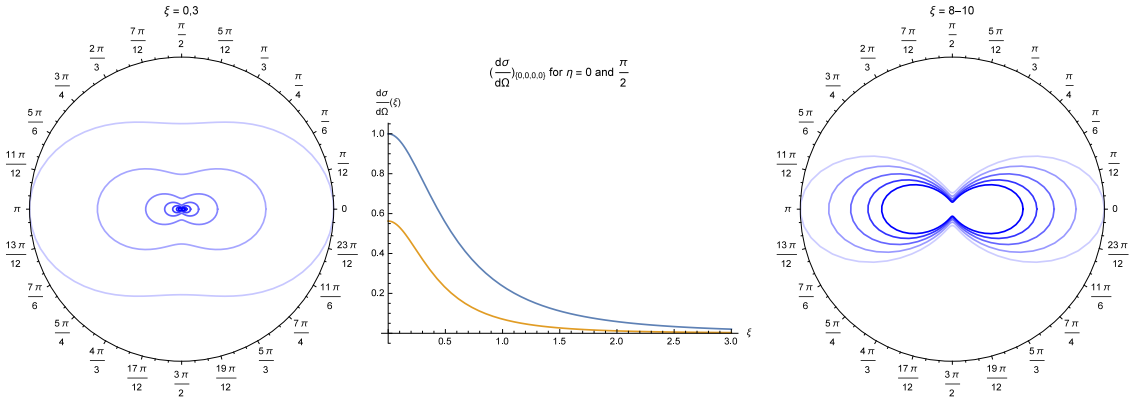

Figure A.38: Differential cross section for $\mathcal{M}_{oooo}$.

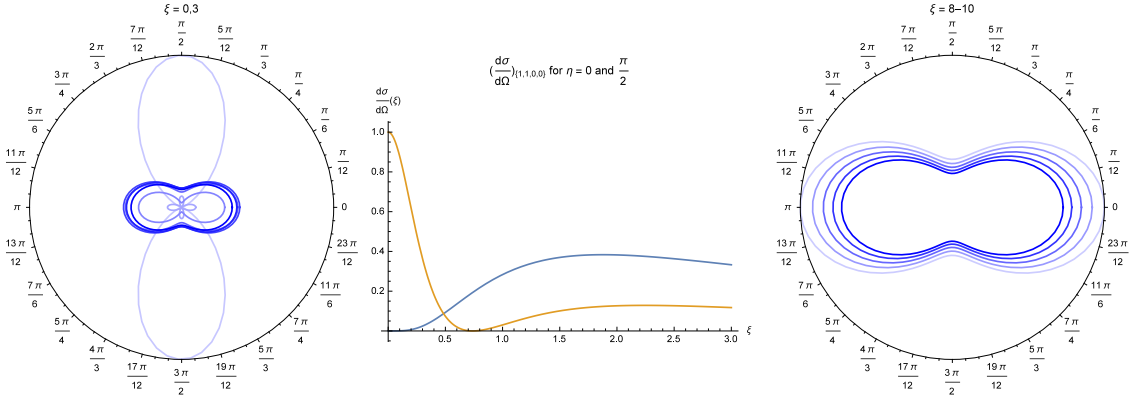

Figure A.39: Differential cross section for $\mathcal{M}_{iioo}$.

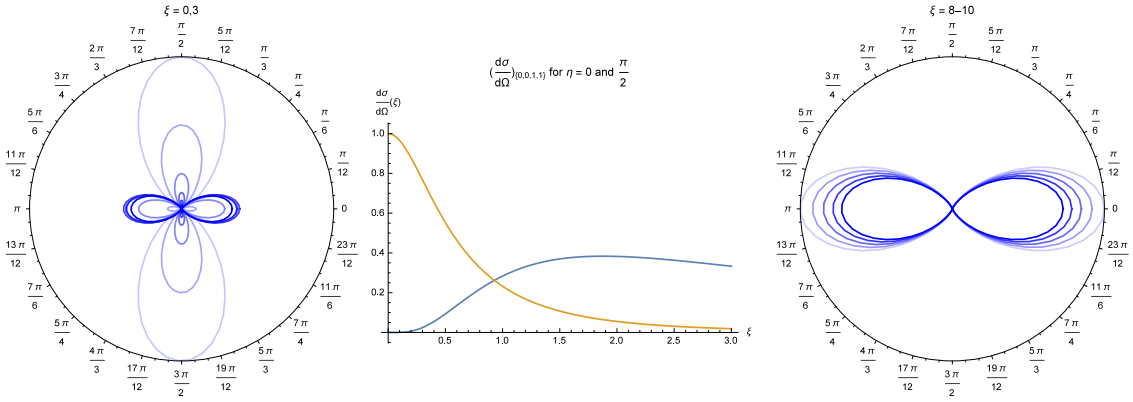

Figure A.40: Differential cross section for $\mathcal{M}_{ooii}$.

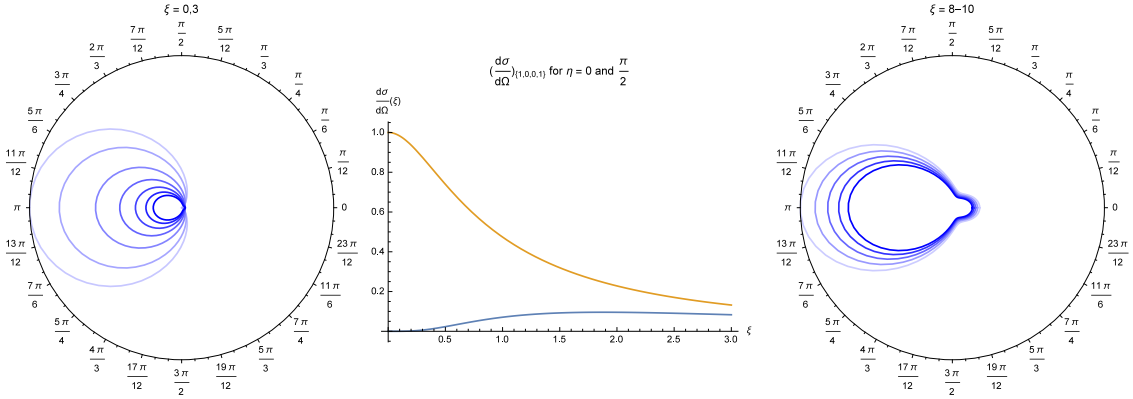

Figure A.41: Differential cross section for $\mathcal{M}_{iooi}$.

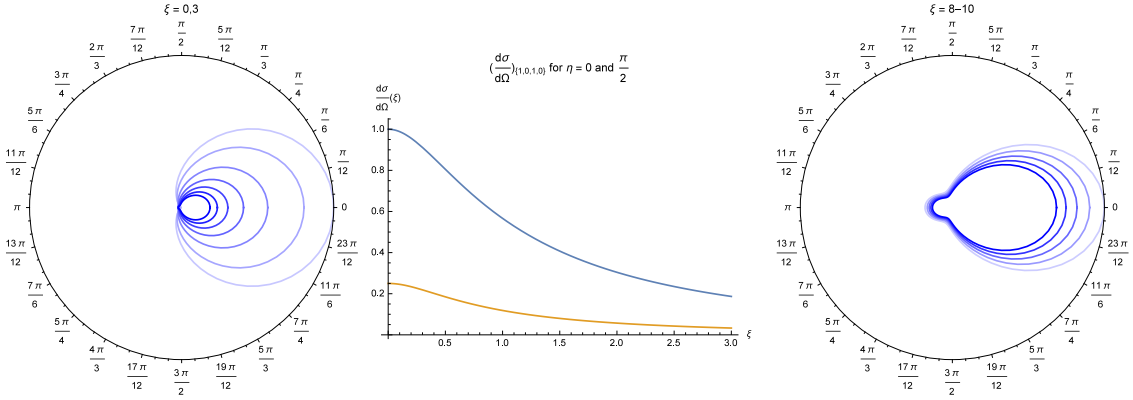

Figure A.42: Differential cross section for $\mathcal{M}_{ioio}$.

A.4.2 B in y direction

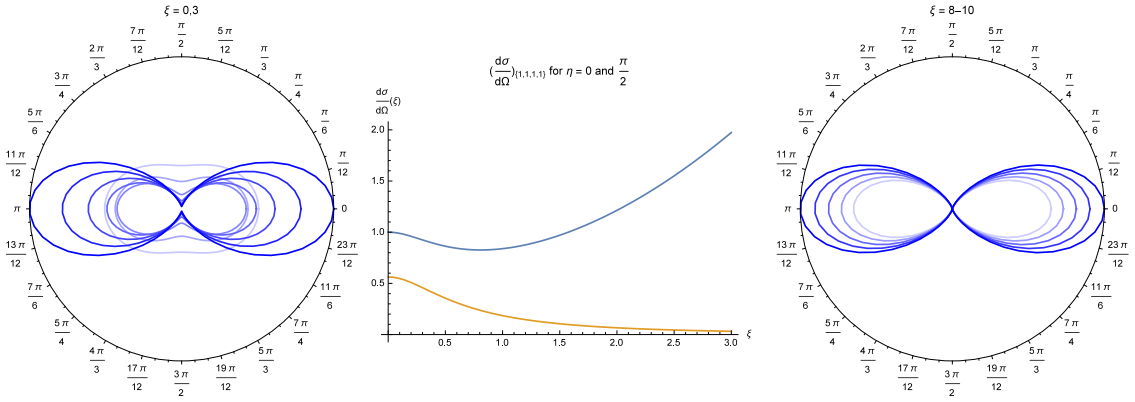

Figure A.43: Differential cross section for $\mathcal{M}_{iiii}$.

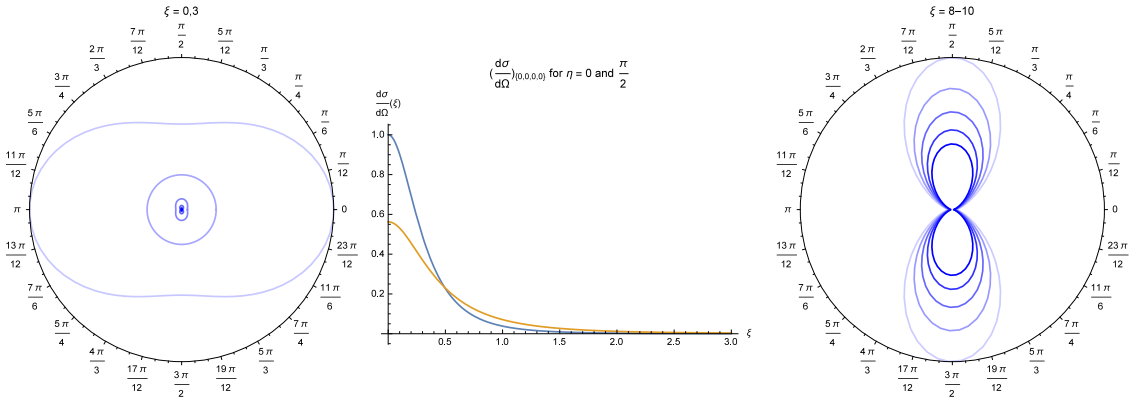

Figure A.44: Differential cross section for $\mathcal{M}_{oooo}$.

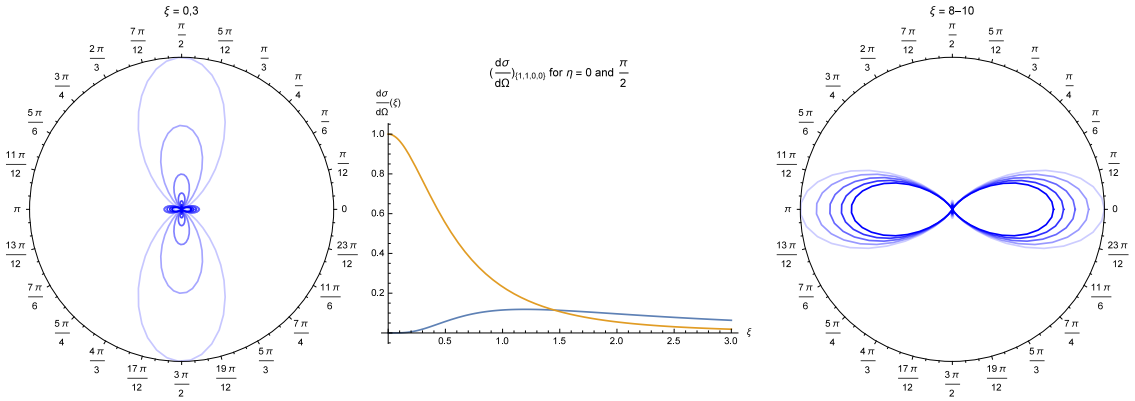

Figure A.45: Differential cross section for $\mathcal{M}_{iioo}$.

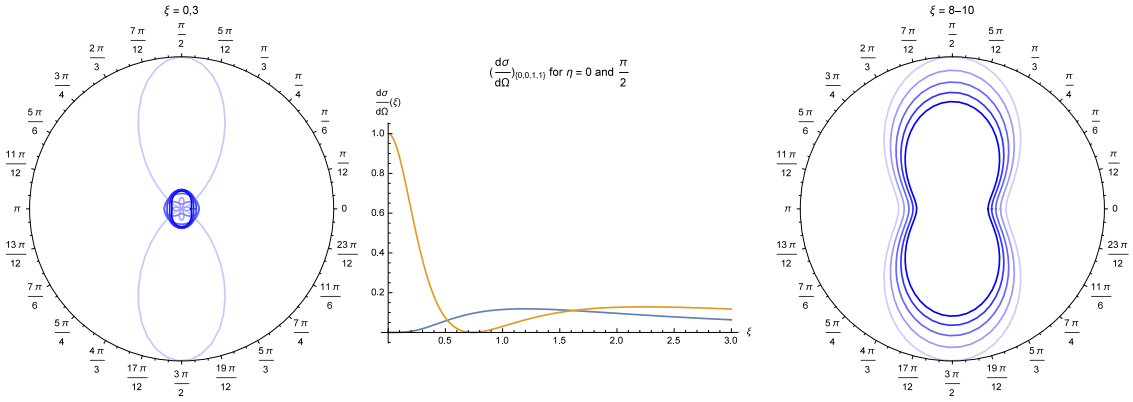

Figure A.46: Differential cross section for $\mathcal{M}_{ooii}$.

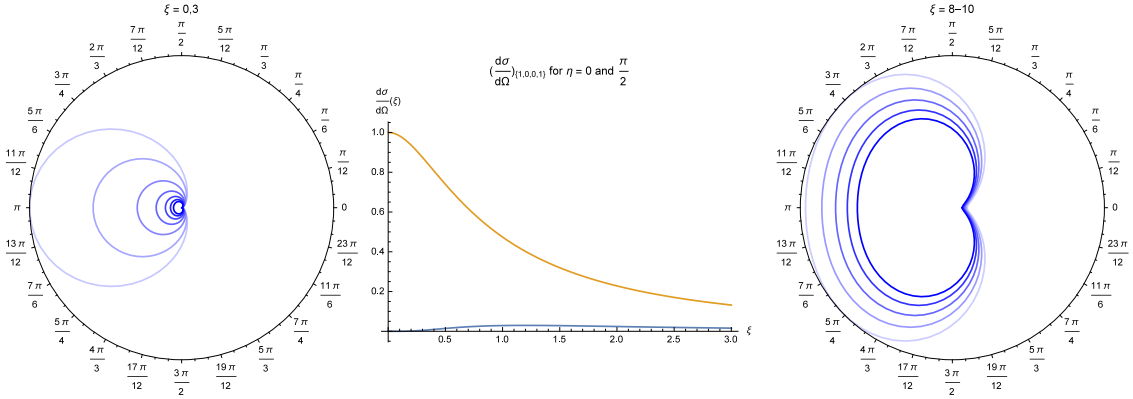

Figure A.47: Differential cross section for $\mathcal{M}_{iooi}$.

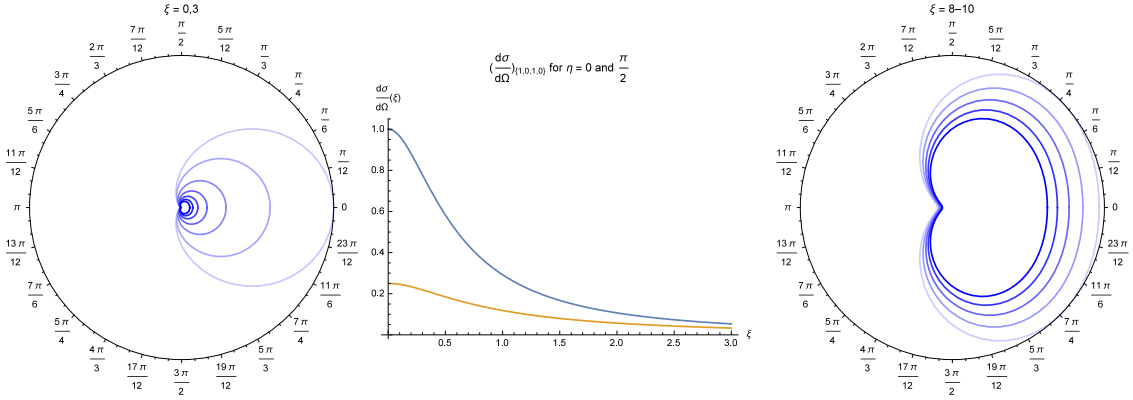

Figure A.48: Differential cross section for $\mathcal{M}_{ioio}$.

A.4.3 B in z direction

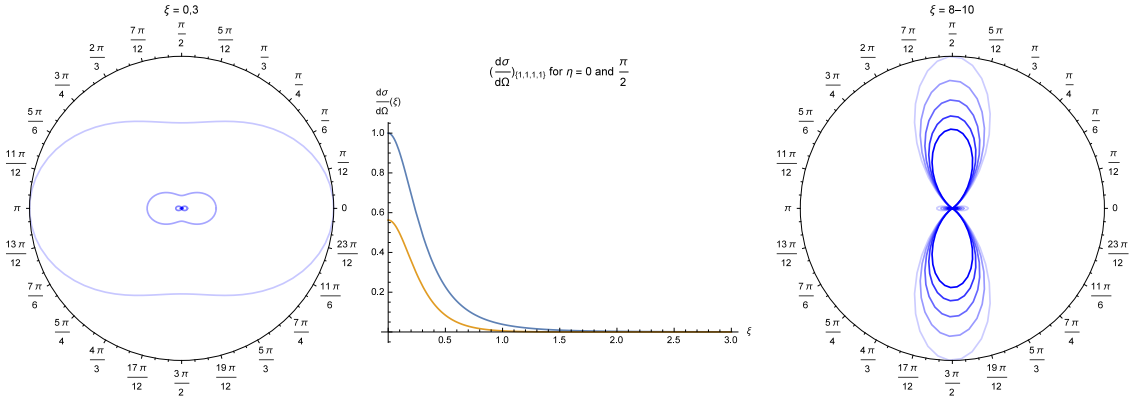

Figure A.49: Differential cross section for $\mathcal{M}_{iiii}$.

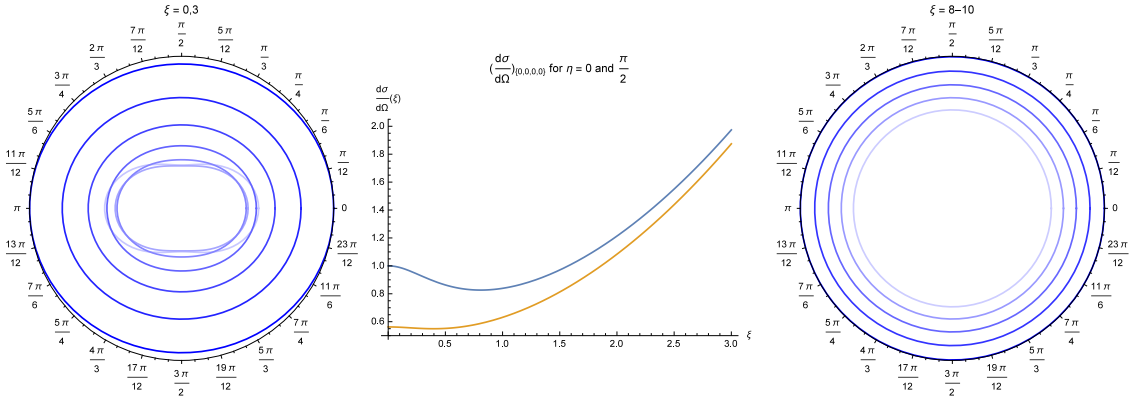

Figure A.50: Differential cross section for $\mathcal{M}_{oooo}$.

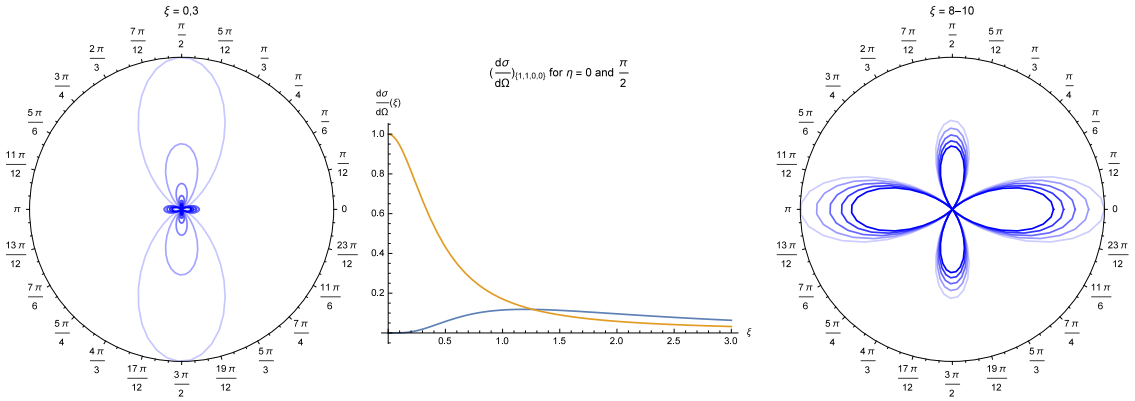

Figure A.51: Differential cross section for $\mathcal{M}_{iioo}$.

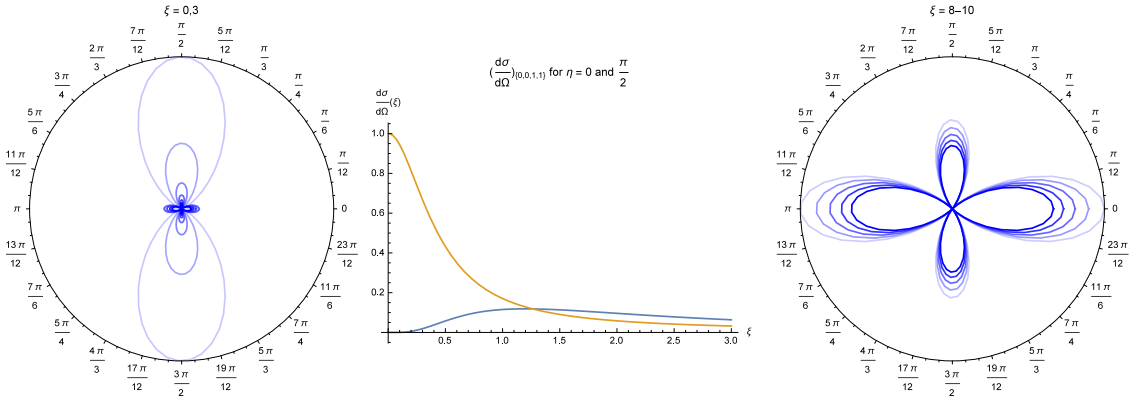

Figure A.52: Differential cross section for $\mathcal{M}_{ooii}$.

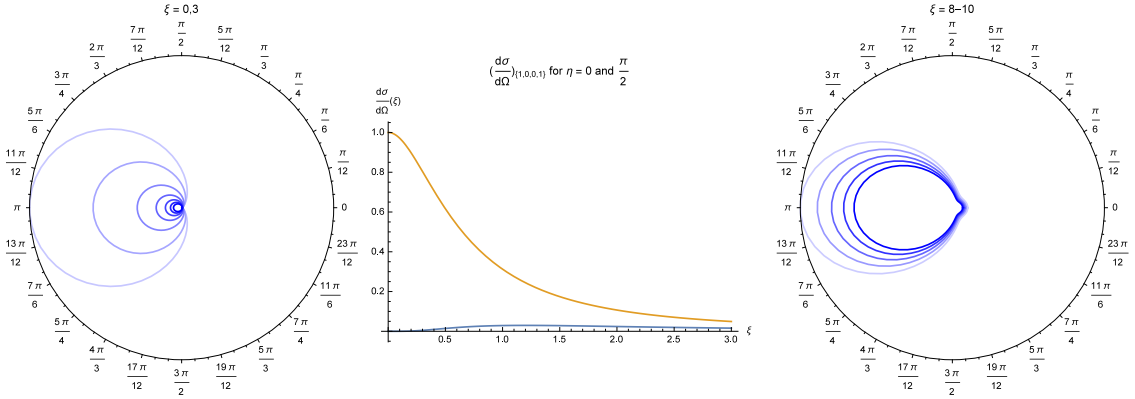

Figure A.53: Differential cross section for $\mathcal{M}_{iooi}$.

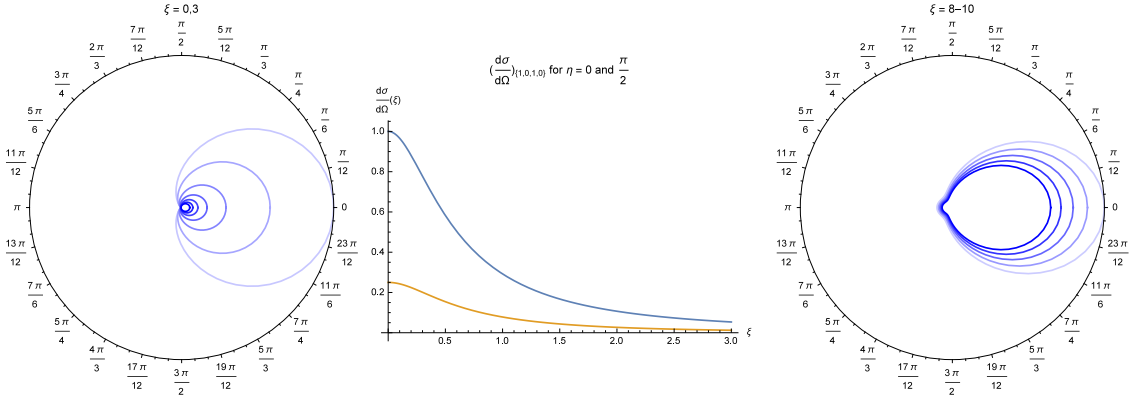

Figure A.54: Differential cross section for $\mathcal{M}_{ioio}$.

A.5 Vector QED

A.5.1 B in x direction

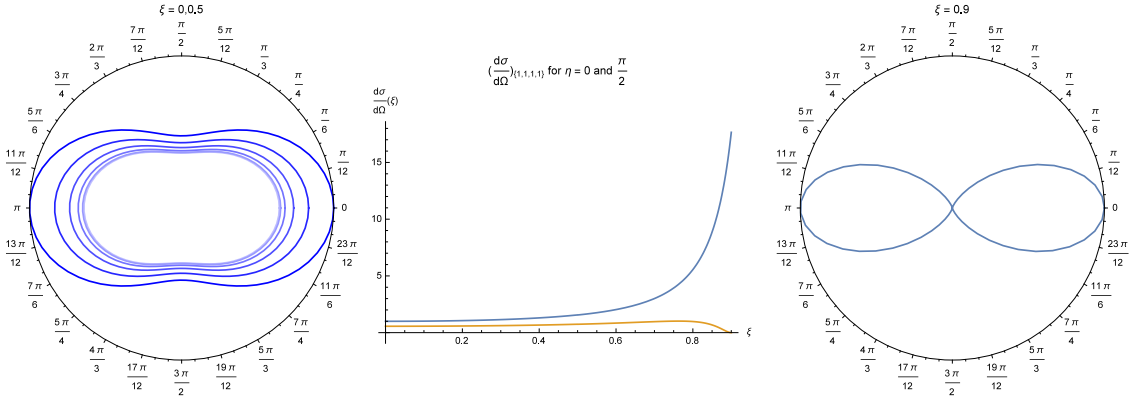

Figure A.55: Differential cross section for $\mathcal{M}_{iiii}$.

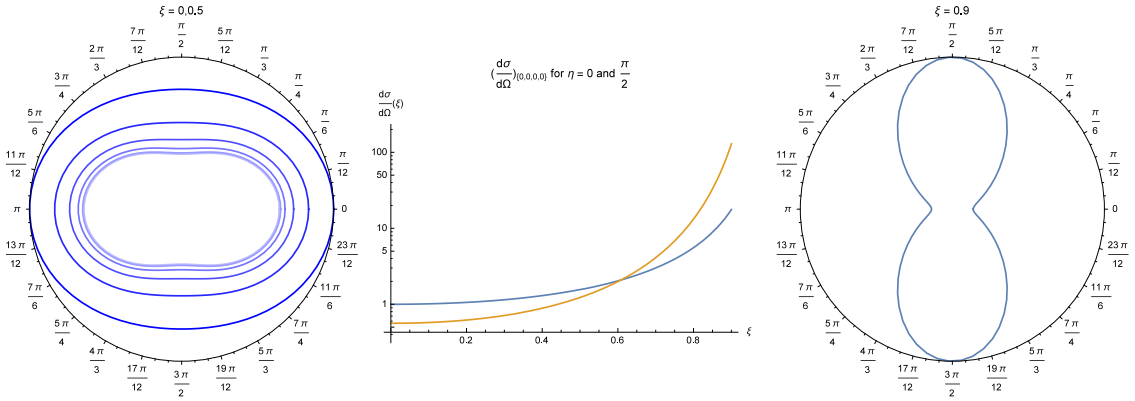

Figure A.56: Differential cross section for $\mathcal{M}_{oooo}$.

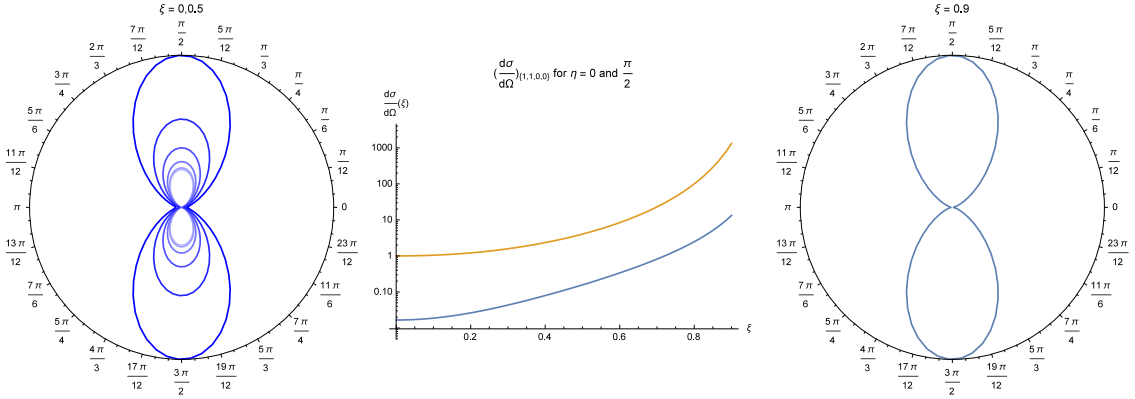

Figure A.57: Differential cross section for $\mathcal{M}_{iioo}$.

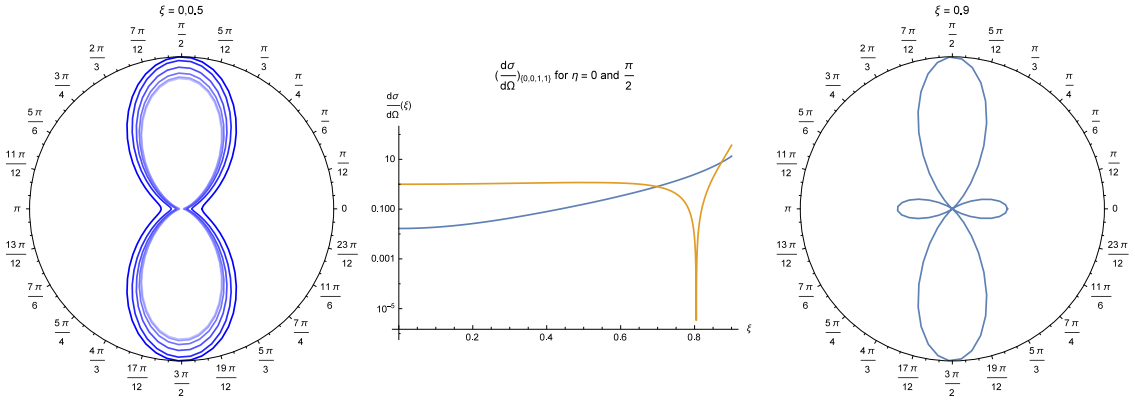

Figure A.58: Differential cross section for $\mathcal{M}_{ooii}$.

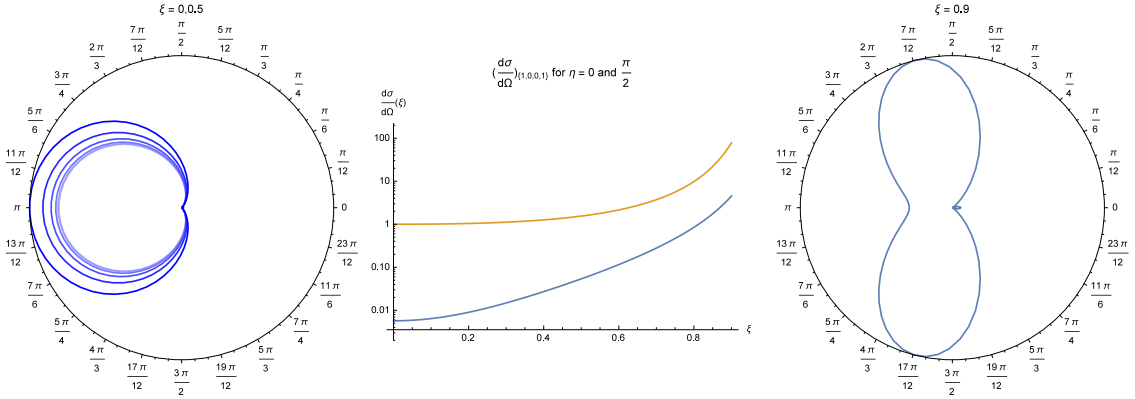

Figure A.59: Differential cross section for $\mathcal{M}_{iooi}$.

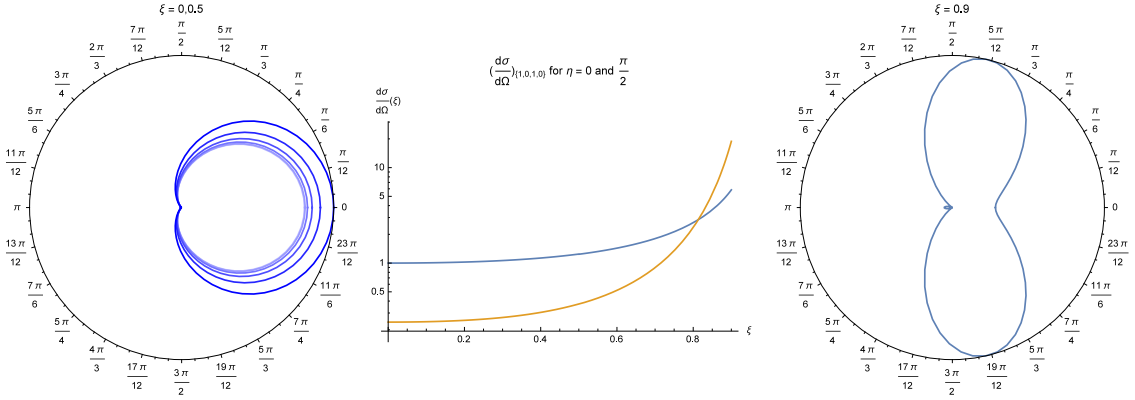

Figure A.60: Differential cross section for $\mathcal{M}_{ioio}$.

A.5.2 B in y direction

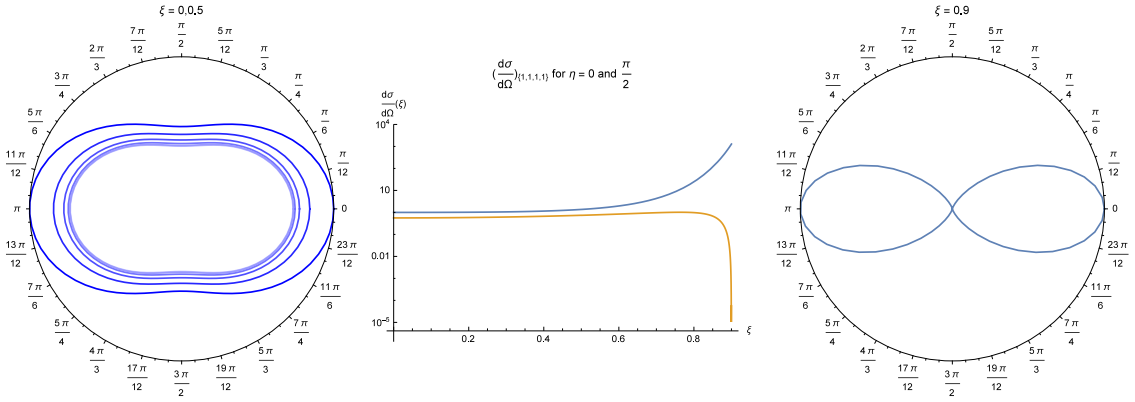

Figure A.61: Differential cross section for $\mathcal{M}_{iiii}$.

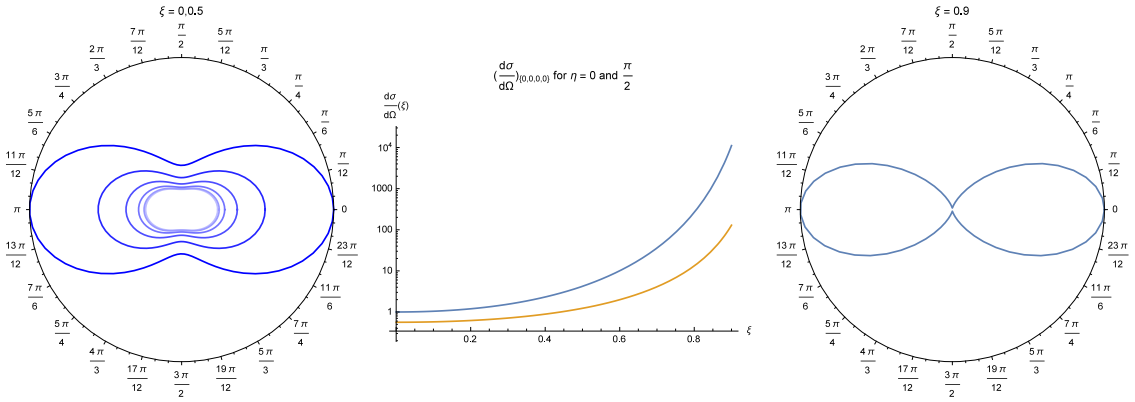

Figure A.62: Differential cross section for $\mathcal{M}_{oooo}$.

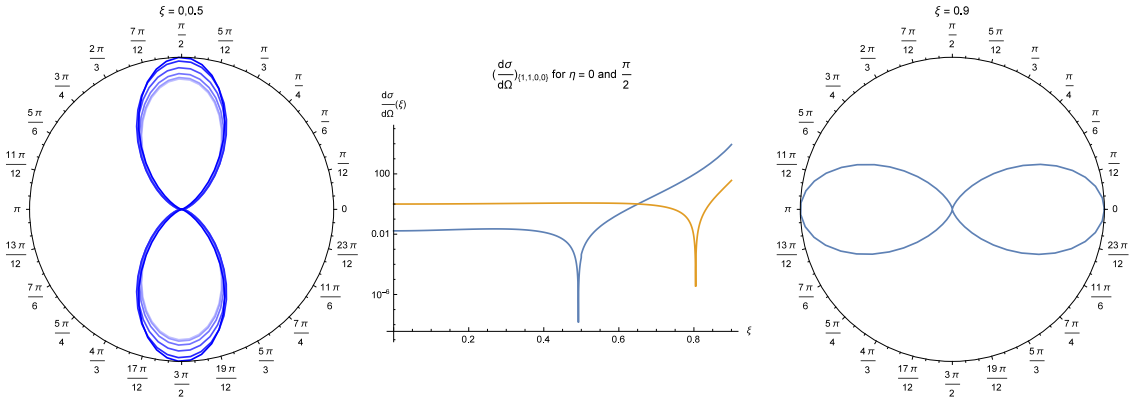

Figure A.63: Differential cross section for $\mathcal{M}_{iioo}$.

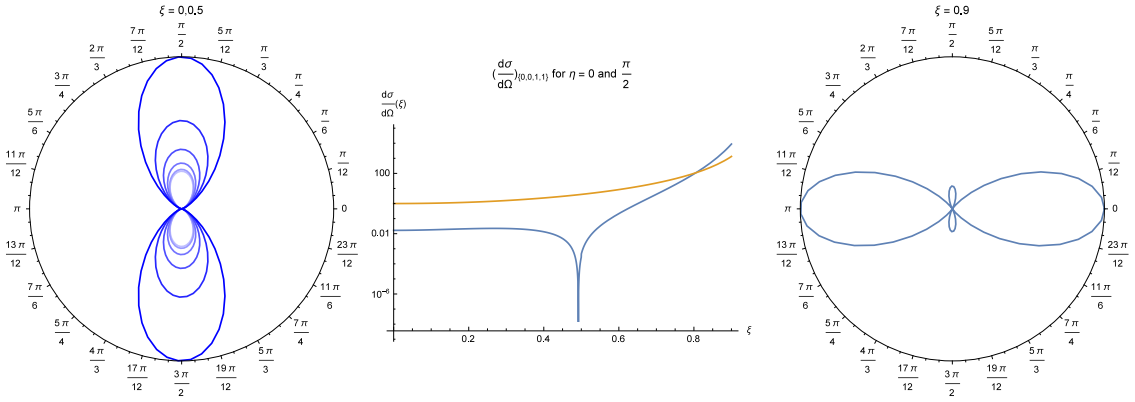

Figure A.64: Differential cross section for $\mathcal{M}_{ooii}$.

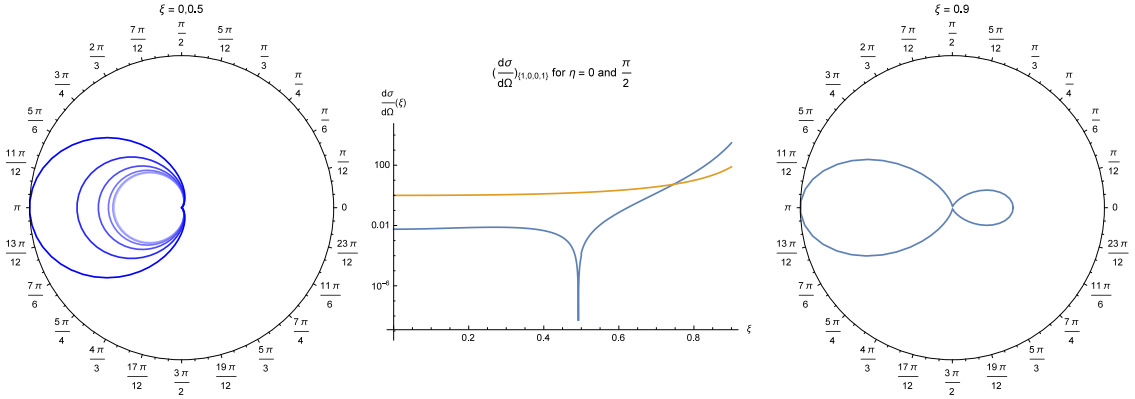

Figure A.65: Differential cross section for $\mathcal{M}_{iooi}$.

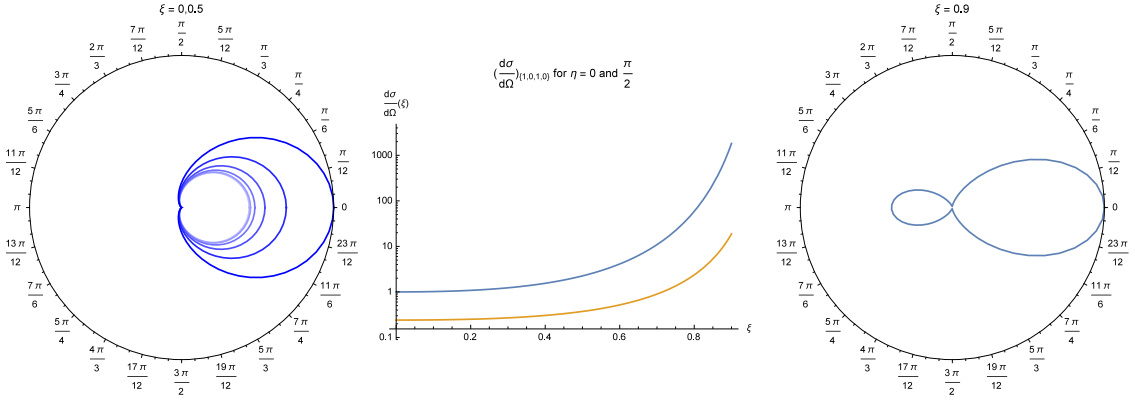

Figure A.66: Differential cross section for $\mathcal{M}_{ioio}$.

A.5.3 B in z direction

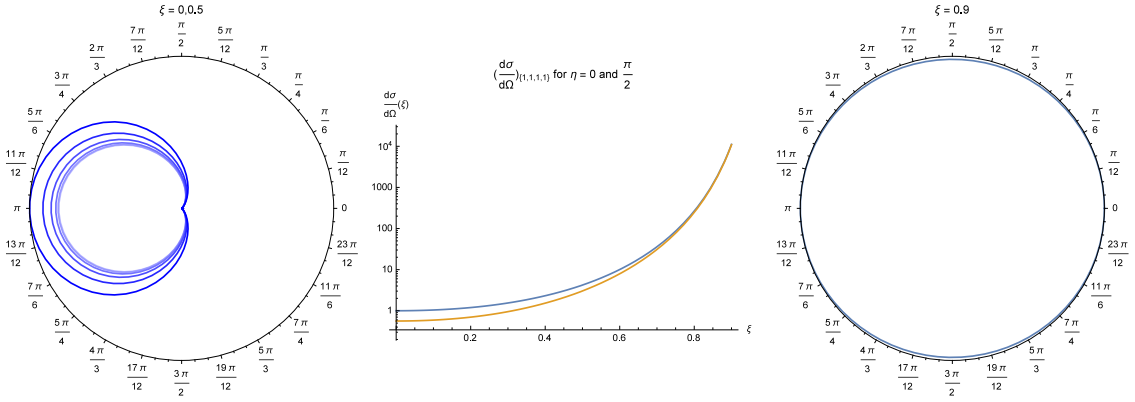

Figure A.67: Differential cross section for $\mathcal{M}_{iiii}$.

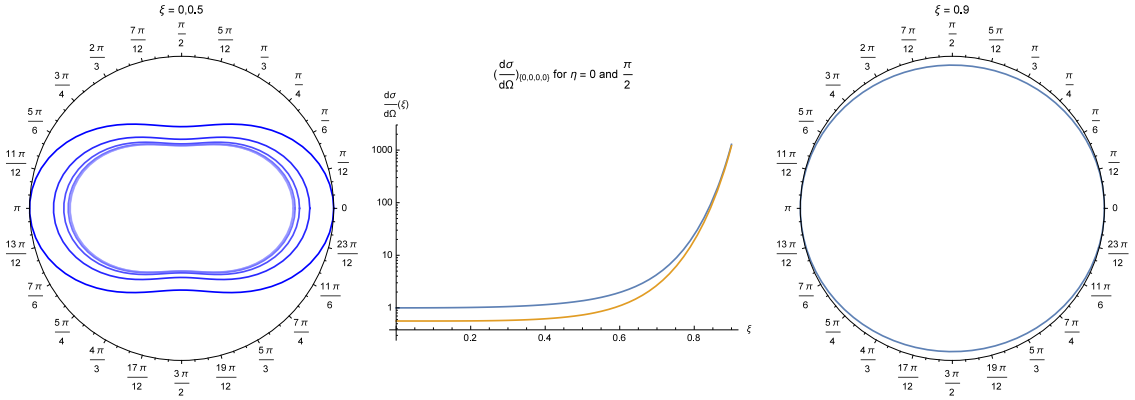

Figure A.68: Differential cross section for $\mathcal{M}_{oooo}$.

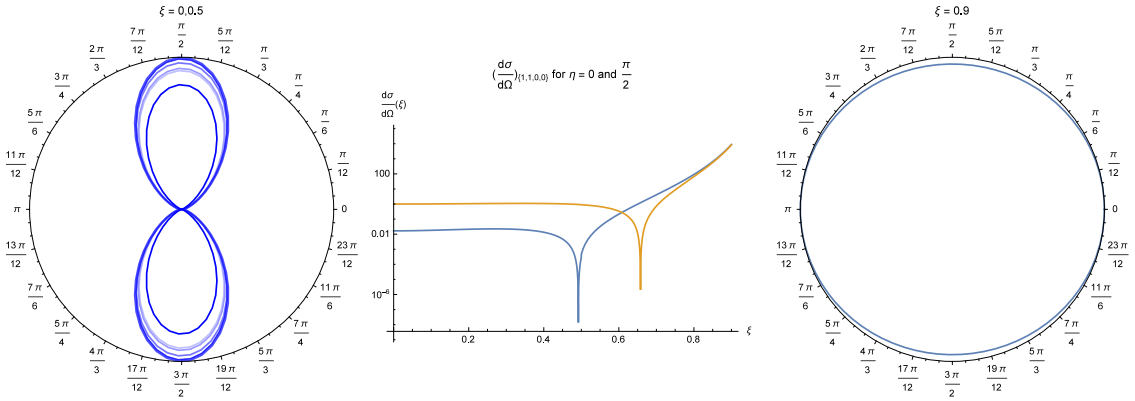

Figure A.69: Differential cross section for $\mathcal{M}_{iioo}$.

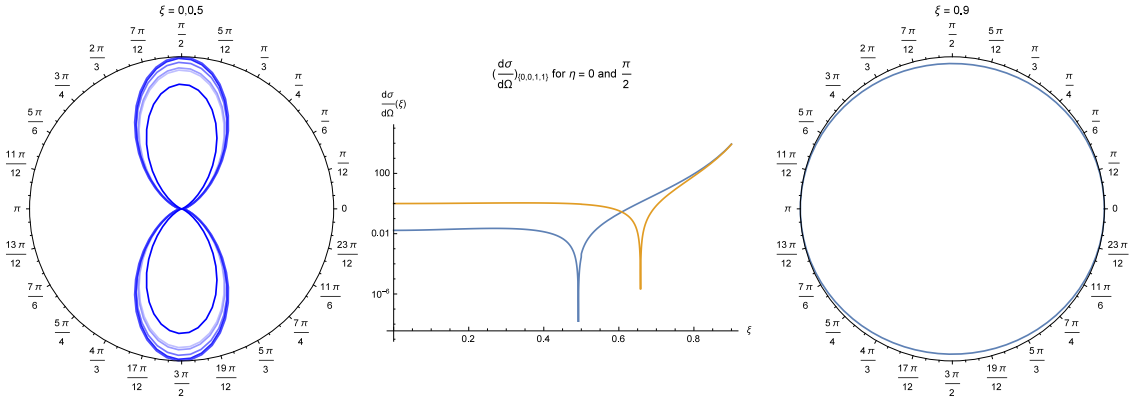

Figure A.70: Differential cross section for $\mathcal{M}_{ooii}$.

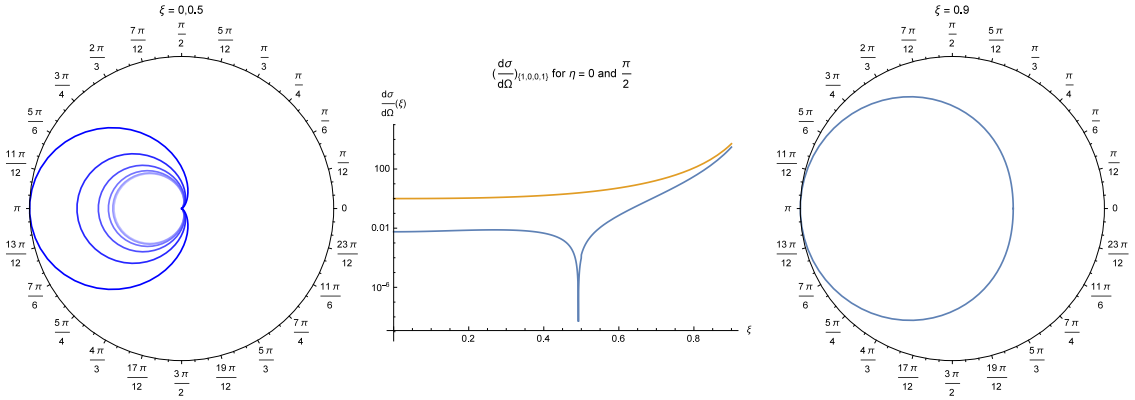

Figure A.71: Differential cross section for $\mathcal{M}_{iooi}$.

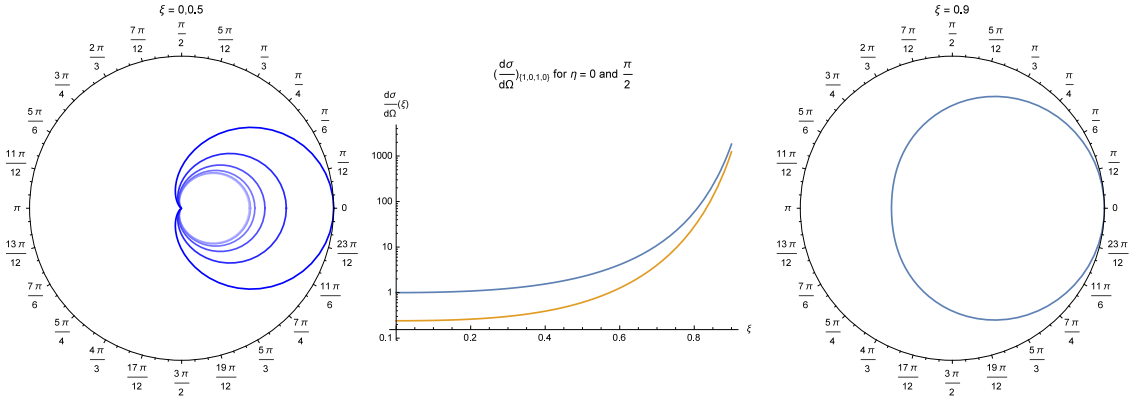

Figure A.72: Differential cross section for $\mathcal{M}_{ioio}$.